



Università degli Studi di Napoli "Federico II"
Dipartimento di Ingegneria Civile, Edile e Ambientale

XXXII Cycle
in Civil System Engineering

Field study on hydrodynamic drivers of magnitude and
spatial patterns of hyporheic exchange at river
confluences

Ivo Martone

Copyright © 2020 by Ivo Martone

Tutors:

Prof. Carlo Gualtieri

Prof. Theodore A. Endreny

PhD Program Coordinator (XXXII Cycle):

Prof. Andrea Papola

Reading Committee:

Daniele Tonina, University of Idaho, USA

Audrey Sawyer, University of Ohio, USA

Location:

Napoli, March 2020

*This manuscript is dedicated to
the loving memory of my grandmother*

Abstract

Confluences are connections in riverine networks characterized by complex three-dimensional changes in flow hydrodynamics and riverbed morphology, and are valued for important ecological functions and hence guide the management and restoration of the whole river environment. This physical complexity is often investigated within the water column or riverbed, while few studies have focused on hyporheic fluxes, which is the mixing of surface water and groundwater across the riverbed. This study aims to understand how hyporheic flux across the riverbed is organized by confluence physical drivers. Field investigations were carried out at two low gradient, headwater confluences in Marcellus, New York, USA over 8 months, beginning from September 2018 to May 2019. The study measured channel bathymetry, hydraulic permeability, and vertical temperature profiles, as indicators of the hyporheic exchange due to temperature gradients. Confluence geometry, hydrodynamics and morphodynamics were found to significantly affect hyporheic exchange rate and patterns. Local scale bed morphology, such as the confluence scour hole and minor topographic irregularities, influenced the distribution of bed pressure head and the related patterns of downwelling/upwelling. Furthermore, classical back-to-back bend planform and the related secondary circulation probably affected hyporheic exchange patterns around the confluence shear layer. Finally, even variations in the hydrological conditions played a role on hyporheic fluxes modifying confluence planform, and, in turn, flow circulation patterns.

Keywords: environmental hydraulics; river confluence; confluence hydrodynamics; hyporheic exchange; vertical hydraulic gradient; heat tracing; hydraulic conductivity

Abstract

Le confluenze rappresentano le connessioni delle reti fluviali, caratterizzate da complessi fenomeni tridimensionali idrodinamici e morfologici, rilevanti nelle funzioni ecologiche, che guidano la gestione ed il ripristino dell'intero ambiente fluviale. Questa complessità fisica viene spesso studiata all'interno della colonna d'acqua o dell'alveo, mentre pochi studi si sono concentrati sui flussi iporreici, che è l'incontro di acque superficiali e sotterranee. Questo studio ha lo scopo di approfondire come il flusso iporreico, attraverso l'alveo del fiume, è organizzato dalla morfologia della confluenza. Due campagne dati sono state condotte su due confluenze, presso la cittadina di Marcellus, New York, USA per 8 mesi, a partire da Settembre 2018 fino a Maggio 2019. Il presente studio ha ricavato la batimetria delle confluenze, la permeabilità idraulica ed i profili di temperatura verticale dei sedimenti del letto del fiume, come indicatori dello scambio iporreico dovuto ai gradienti di temperatura. È emerso che la geometria della confluenza, l'idrodinamica e la morfodinamica influenzano in modo significativo il tasso e lo schema dello scambio iporreico. La morfologia del letto su scala locale, come lo scour hole, presente in una confluenza, e le piccole irregolarità topografiche, hanno influenzato la distribuzione delle pressioni sull'interfaccia acqua/sedimenti ed i relativi pattern di downwelling / upwelling. Inoltre, la classica forma planare curva back-to-back e la relativa secondary flow hanno probabilmente influenzato i pattern dei flussi iporreici attorno allo shear layer della confluenza. Infine, anche le variazioni delle condizioni idrologiche hanno avuto un ruolo sui flussi iporreici modificando la forma planare della confluenza e, a loro volta, il campo di moto della confluenza.

Parole chiave: idraulica ambientale; confluenze fluviali; idrodinamica fluviale; scambio iporreico; gradiente idraulico verticale; traccanti; conducibilità idraulica

Acknowledgements

Firstly, I would like to express my gratitude to Prof. Carlo Gualtieri for the continuous support of my Ph.D study and related research, for his patience, motivation, and immense knowledge. His guidance helped me in all the time of research and writing of this thesis.

Secondly, I would like to manifest my sincerest thanks and appreciation to Prof. Ted Endreny, who trusted in my capacity to perform this research in such a challenging and interesting topic and accepted to guide my work. I am also grateful to his family which made my stay abroad more pleasant and enjoyable.

Besides my advisors, I would like to thank my PhD Coordinator Prof. Andrea Papola and the Scientific PhD Committee for evaluating and accepting the contents of this doctoral research over the past three years.

I sincerely thank the reading committee for the time spent reviewing this thesis and for their insightful comments and encouragement, but also for the hard question which incited me to widen my research from various perspectives.

My respect and consideration go to Guy Swenson for joining me in field surveys and data analysis. Without his precious support it would not have been possible to conduct this research.

I also show my gratitude to SUNY for hosting, support and instrumentation. Collaboration with staff of the Environmental Resources Engineering Department of the SUNY-ESF is gratefully acknowledged. In particular, I thank Teri Frese, Thomas Carter and the Office of International Education for their assistance and friendliness.

I thank my colleagues at DICEA: Andrea, Gerardo, Vittorio, Francesco, Maria Cristina, Diana, Guadalupe for the stimulating discussions, for the time spent together, and for all the fun we have had in the last three years. Also I thank my

international colleagues Farhad and Mohammed for sharing their culture, knowledge and time with me. A special thank goes to Giuseppe, who also helped me through my doctoral research.

I also thank all the people I met in Syracuse. In particular, I am grateful to Reza, for his precious help and warm welcome, Atef, for his kindness and support, Melvin, for getting me around in several trips, Rocco, for his friendship and time spent together, and all the fellows and friends around the campus. I would like to express my gratitude to Luke and Kate for their hospitality.

My affection goes to my best friends Francesco, Marco and Pasquale for their moral support and strong friendships over the last years.

Last but not the least, I would like to thank my parents and my brother for supporting me spiritually throughout writing this thesis and my life in general.

Contents

List of Figures	x
List of Tables	xviii
1 Introduction	1
1.1 Objectives and method of the thesis	1
1.2 Structure of the thesis	3
References	5
2 Rivers confluence	7
2.1 Introduction	7
2.2 Flow structure	9
2.3 Mixing at hydraulic confluence	13
2.4 Bed morphology	16
References	19
3 Hyporheic fluxes	26
3.1 Introduction	26
3.2 Structure, rates and scale of hyporheic exchange	27
3.3 The hyporheic zone outlining methods	29
3.4 Flux mechanism	30
3.5 Hyporheic exchange causing factors	32
3.6 Measurement of the hyporheic exchange	35

3.7	Hyporheic exchange numerical modelling	38
3.8	Existing studies on hyporheic exchange at river confluences	42
References		45
4	Field surveys	50
4.1	Study site	50
4.1.1	Soils	50
4.1.2	Climate	51
4.2	Baltimore Woods Nature Center (Marcellus, NY, USA)	55
4.2.1	Site description	55
4.3	Ninemile Creek (Marcellus, NY, USA)	57
4.3.1	Site description	58
4.4	Methodology and scheduled field campaigns	59
4.4.1	Total station theodolite	60
4.4.2	GPS System	61
4.4.3	Confluence bed sediment analysis	62
4.4.4	Hydraulic conductivity test pipe	64
4.4.5	Piezometers	65
4.4.6	Temperature rods	66
4.4.7	Flow meters	70
4.5	Post-processing data	73
4.5.1	Temperature data code analysis: VFLUX2	73
References		76
5	Data results	80
5.1	Plan form geometry	80
5.1.1	BWC site	80
5.1.2	NMC site	81
5.2	Hydrodynamics observation	81
5.2.1	BWC site	81
5.2.2	NMC site	85
5.3	Grain size analysis	86

5.3.1	BWC grain size analysis	86
5.3.2	NMC grain size analysis	87
5.4	Hydraulic conductivity tests	89
5.4.1	BWC test results	89
5.4.2	NMC test results	90
5.5	Piezometers results	91
5.5.1	BWC Vertical Hydraulic Gradients (VHG)	91
5.5.2	Transversal hydraulic gradients at BWC	92
5.5.3	BWC darcian fluxes	95
5.6	Temperature time series	96
5.6.1	BWC results	96
5.6.2	NMC results	102
References		105
6	Relations between river confluence and hyporheic exchange	107
6.1	Effect on variations in confluence geometry on the hyporheic fluxes	108
6.2	Effect of secondary flows on the hyporheic fluxes	111
6.3	Effect on variations in soil grain size and hydraulic conductivity . .	114
6.4	VHF estimating methods comparison	115
6.4.1	Temperature time series versus piezometers readings at BWC	115
References		118
7	Conclusions	122
References		127
A	Temperature time series charts	129
B	Downward fluxes charts	144
Abbreviations and List of symbols		158

List of Figures

1.1	Aerial View of Passau and the Confluence of the Inn (left), Danube (right) and the Ilz river (small river far right), Austria.	2
2.1	Confluence of the Mosel and Rhine Rivers in Koblenz, Germany. . .	8
2.2	In the picture, the six zones may be appreciated. Figure from Best and Reid 1984.	10
2.3	Figure from Gurram et al. (1997).	12
2.4	Figure from Ashmore (1982).	13
2.5	River junction between Rio Negro and Rio Solimões, Manaus, Brazil.	14
3.1	Horizontal and vertical variability of hyporheic exchange. Image from Stonedahl et al. (2010).	27
3.2	The three method comparison. Figure from Tonina and Buffington (2009).	30
3.3	Hyporheic exchange, e , per unit length for an infinitesimal volume of length, l , of the hyporheic zone, modified from Tonina and Buffington (2009).	31
3.4	Figure from Tonina and Buffington (2009).	32
3.5	Figure from Cardenas and Wilson (2007a). (a) Schematic of model domain and system formulation, (b) representative finite element mesh, (c) typical solution for flow directions and (d) close up view of the eddy showing streamlines.	40
3.6	Figure from Revelli et al. (2008). (a) Shows an example of a river planimetry, whereas (b) presents the detail of a single meander. . .	41

3.7	Hyporheic flux patterns at the Juehe River and the Haohe River confluence. Figures from Song et al. (2017) (down), Cheng et al. (2019) (up)	43
4.1	Study area overview	51
4.2	Soil characteristics of Marcellus town (source: USGS)	52
4.3	Monthly normal precipitation (1981-2010) at Syracuse Hancock INTL AP (source: NOAA Online Weather Data)	53
4.4	Max (Red line) and min (Blue line) temperature observations between October 1942 through to December 2012 at Syracuse Hancock International (source: NOAA Online Weather Data)	54
4.5	Marcellus study areas (red rectangles)	56
4.6	Baltimore Woods Nature Center study site.	57
4.7	Ninemile Creek confluence study site.	58
4.8	Topcon GTS-250	61
4.9	Black crosses represent K_v test point locations (05/06/19) while red crosses are soil sample collection points.	63
4.10	Pipe used for K_v tests.	64
4.11	Red crosses represent soil sample collection points and black crosses K_v test point locations at NMC.	65
4.12	Piezometers map at Baltimore Woods Nature Center confluence. . .	66
4.13	Surface-subsurface water temperature collection setup	68
4.15	iButtons location at NMC during FS-NCUC2.	70
4.16	MFP51 Stream Flow meter components (left) and deployment (right)	71
4.17	(a) Instrument set-up explained; (b) Sontek Flow Tracker Handheld adv probe	72
5.1	Topography of watershed and riverbeds about the BWC confluence zone, with black solid contour lines showing elevation above sea level (m). Black dotted lines delineate the active channel during low flow, and the red dotted ellipse delineates a scour hole.	82

5.2	Topography of watershed and riverbeds about the NMC confluence zone, with black solid contour lines showing elevation above sea level (<i>m</i>). Black dotted lines delineate the active channel during low flow.	83
5.3	BWC hydrodynamics observation. Typical flow structure at BWC (up) and a high-flow event in December 2018 with liquid precipitation and snowmelt (down).	84
5.4	NMC hydrodynamics observation. Picture taken on 10/16/18 facing north (left) and typical flow structure at NMC (right).	85
5.5	Results gathered after US SAH-97TM sieves at BWC.	87
5.6	Soil grain size distribution within BWC, showing a fining of sand from upstream (BB and CB sites) to downstream into the confluence zone (CHZ).	88
5.7	Soil grain size distribution within NMC, showing medium-fine sand at NM riverbed.	88
5.8	VHG patterns at BWC. Green and red dots are downwelling and upwelling fluxes, respectively. Black dash represents no-exchange (pressure head gradient $< 1\text{ cm}$)	93
5.9	Pressure heads at BWC. Values are meters above mean sea water level.	94
5.10	Darcian fluxes evaluated with hydraulic conductivity test results (Table 5.5).	96
5.11	VHF map at BWC in September 2018 (FS-BBCB1). Downwelling and upwelling fluxes are illustrated by red and blue contours, respectively.	98
5.12	Vertical hyporheic fluxes (<i>mm/d</i>) for October 23 to November 6 2018, derived from temperature profiles. Light blue contour represents an interpolated transitional zone.	99
5.13	VHF map at BWC in December 2018 (FS-BBCB1). Downwelling and upwelling fluxes are illustrated by red and blue contours, respectively.	100
5.14	VHF map at BWC in March-April 2019 (FS-BBCB2). Downwelling and upwelling fluxes are illustrated by red and blue contours, respectively.	101

5.15	Ninemile Creek runoff at gage 04240300 from April 17 to May 23, 2019 (Lakeland, NY).	103
5.16	VHF map of NMC. Downwelling and upwelling fluxes are illustrated by red and blue contours, respectively.	104
6.1	Longitudinal distribution of pressure coefficient in a backward facing step Driver and Seegmiller (1985).	108
6.2	VHF map extents from FS-BBCB1 and FS-BBCB2. Red polygon refers to September 2018 map dark green, dark blue and black recall December 2018, October 2018 and March 2019 maps, respectively. The scour hole is individuated by the red ellipse.	109
6.3	Test points and cross-section locations from FS-BBCB1 and FS-BBCB2. Red points refer to September 2018, light blue, dark blue and black recall to December 2018, October 2018 and March 2019, respectively. The red ellipse represents the scour hole.	110
6.4	Longitudinal sections at BWC (AA' and BB'). Red and blue light fill depict downwelling and upwelling zones, respectively.	111
6.5	Cross sections at BWC (CC' and DD'). Dotted line shows shear layer position and helicoidal rotating cells represent ideal water circulation. Red and blue light fill depict downwelling and upwelling zones, respectively.	112
6.6	K_v map at BWC. Values range from higher (Red contour) to lower (Yellow contour) conductivity	114
6.7	iButtons rods and piezometers point locations during September 2018 (FS-BBCB1).	116
A.1	Temperature time series at BWC during 0918 (FS-BBCB1). Temperature probe A.	130
A.2	Temperature time series at BWC during 0918 (FS-BBCB1). Temperature probe B.	130
A.3	Temperature time series at BWC during 0918 (FS-BBCB1). Temperature probe C.	131
A.4	Temperature time series at BWC during 0918 (FS-BBCB1). Temperature probe D.	131

A.5	Temperature time series at BWC during 0918 (FS-BBCB1). Temperature probe E.	132
A.6	Temperature time series at BWC during 1018 (FS-BBCB1). Temperature probe A.	132
A.7	Temperature time series at BWC during 1018 (FS-BBCB1). Temperature probe B.	133
A.8	Temperature time series at BWC during 1018 (FS-BBCB1). Temperature probe C.	133
A.9	Temperature time series at BWC during 1018 (FS-BBCB1). Temperature probe D.	134
A.10	Temperature time series at BWC during 1018 (FS-BBCB1). Temperature probe E.	134
A.11	Temperature time series at BWC during 1018 (FS-BBCB1). Temperature probe F.	135
A.12	Temperature time series at BWC during 1218 (FS-BBCB1). Temperature probe A.	135
A.13	Temperature time series at BWC during 1218 (FS-BBCB1). Temperature probe B.	136
A.14	Temperature time series at BWC during 1218 (FS-BBCB1). Temperature probe C.	136
A.15	Temperature time series at BWC during 1218 (FS-BBCB1). Temperature probe D.	137
A.16	Temperature time series at BWC during 1218 (FS-BBCB1). Temperature probe E.	137
A.17	Temperature time series at BWC during 1218 (FS-BBCB1). Temperature probe F.	138
A.18	Temperature time series at BWC during 0319 (FS-BBCB2). Temperature probe A.	138
A.19	Temperature time series at BWC during 0319 (FS-BBCB2). Temperature probe B.	139
A.20	Temperature time series at BWC during 0319 (FS-BBCB2). Temperature probe C.	139

A.21 Temperature time series at BWC during 0319 (FS-BBCB2). Temperature probe D.	140
A.22 Temperature time series at BWC during 0319 (FS-BBCB2). Temperature probe E.	140
A.23 Temperature time series at BWC during 0319 (FS-BBCB2). Temperature probe F.	141
A.24 Temperature time series at NMC during 0419 (FS-NMUC2). Temperature probe A.	141
A.25 Temperature time series at NMC during 0419 (FS-NMUC2). Temperature probe B.	142
A.26 Temperature time series at NMC during 0419 (FS-NMUC2). Temperature probe C.	142
A.27 Temperature time series at NMC during 0419 (FS-NMUC2). Temperature probe D.	143
B.1 Downward fluxes at BWC during 0918 (FS-BBCB1). Temperature probe A.	145
B.2 Downward fluxes at BWC during 0918 (FS-BBCB1). Temperature probe B.	145
B.3 Downward fluxes at BWC during 0918 (FS-BBCB1). Temperature probe C.	146
B.4 Downward fluxes at BWC during 0918 (FS-BBCB1). Temperature probe D.	146
B.5 Downward fluxes at BWC during 0918 (FS-BBCB1). Temperature probe E.	147
B.6 Downward fluxes at BWC during 1018 (FS-BBCB1). Temperature probe A.	147
B.7 Downward fluxes at BWC during 1018 (FS-BBCB1). Temperature probe B.	148
B.8 Downward fluxes at BWC during 1018 (FS-BBCB1). Temperature probe C.	148
B.9 Downward fluxes at BWC during 1018 (FS-BBCB1). Temperature probe D.	149

B.10	Downward fluxes at BWC during 1018 (FS-BBCB1). Temperature probe E.	149
B.11	Downward fluxes at BWC during 1018 (FS-BBCB1). Temperature probe F.	150
B.12	Downward fluxes at BWC during 1218 (FS-BBCB1). Temperature probe A.	150
B.13	Downward fluxes at BWC during 1218 (FS-BBCB1). Temperature probe B.	151
B.14	Downward fluxes at BWC during 1218 (FS-BBCB1). Temperature probe D.	151
B.15	Downward fluxes at BWC during 1218 (FS-BBCB1). Temperature probe E.	152
B.16	Downward fluxes at BWC during 1218 (FS-BBCB1). Temperature probe F.	152
B.17	Downward fluxes at BWC during 0319 (FS-BBCB2). Temperature probe A.	153
B.18	Downward fluxes at BWC during 0319 (FS-BBCB2). Temperature probe B.	153
B.19	Downward fluxes at BWC during 0319 (FS-BBCB2). Temperature probe C.	154
B.20	Downward fluxes at BWC during 0319 (FS-BBCB2). Temperature probe D.	154
B.21	Downward fluxes at BWC during 0319 (FS-BBCB2). Temperature probe E.	155
B.22	Downward fluxes at BWC during 0319 (FS-BBCB2). Temperature probe F.	155
B.23	Downward fluxes at NMC during 0419 (FS-NMUC2). Temperature probe A.	156
B.24	Downward fluxes at NMC during 0419 (FS-NMUC2). Temperature probe B.	156
B.25	Downward fluxes at NMC during 0419 (FS-NMUC2). Temperature probe C.	157

B.26 Downward fluxes at NMC during 0419 (FS-NMUC2). Temperature probe D.	157
-------------------------------------------------------------------------------------	-----

List of Tables

3.1	Table comparison among previous studies on hyporheic fluxes at river confluences and purpose of this study.	44
4.1	Resume of BWC and NMC field studies. LS stands for land survey, GSA for grain size analysis, K_v is the hydraulic conductivity, VHГ the vertical hydraulic gradient, TTS the temperature time series. . .	60
4.2	Input parameters of VFLUX2 code for computing hyporheic flux, where β is dispersivity, K_{Cal} the thermal conductivity, Cs_{Cal} volumetric heat capacity of the sediment, and Cw_{Cal} the volumetric heat capacity of the water.	74
5.1	Low flow active channel width (m), depth (m), average velocity (m/s), and discharge (m^3/s) in BB, CB, and the confluence CHZ. Data for BB and CB were collected 1.5 meters upstream of the junction, and data for CHZ were collected 3 meters downstream of the river junction.	85
5.2	Low flow active channel width (m), depth (m), average velocity (m/s), and discharge (m^3/s) in NC, UC, and the confluence CHZ. Data for BB and CB were collected 1.5 meters upstream of the junction, and data for CHZ were collected 3 meters downstream of the river junction.	86
5.3	Sediment size distributions at BWC. Samples are referred to December 2nd 2018 collection. $\sigma_G = (d_{84}/d_{16})^{1/2}$, $S = (d_{90}/d_{10})^{1/2}$, $Gr = 1/2 \cdot (d_{84}/d_{50}) + (d_{50}/d_{16})$	89

5.4	Sediment size distributions at NMC. Samples are referred to May 23rd 2019 collection. $\sigma_G = (d_{84}/d_{16})^{1/2}$, $S = (d_{90}/d_{10})^{1/2}$, $Gr = 1/2 \cdot (d_{84}/d_{50}) + (d_{50}/d_{16})$	90
5.5	Statistical analysis of K_v during 05/06/19 field campaign. Values are in m/d	90
5.6	Statistical analysis of K_v during 05/23/19 field campaign at NMC. Values are in m/d	91
5.7	Statistical analysis of VHG. Values are dimensionless. Downwelling and upwelling are negative and positive, respectively.	92
5.8	Statistical analysis of Darcian fluxes at BWC. Coefficient of variation (CV) and values are in mm/d	97
6.1	Vertical fluxes calculation comparison. Values are in mm/d and positive downward.	117

Chapter 1

Introduction

River confluences are, in fluvial systems, characterized by changes in flow hydrodynamics, bed morphology and important ecological functions, where the combining flows converge and realign further downstream a region known also as confluence hydrodynamic zone (CHZ). Velocity gradients in these non-uniform flows influence hydrodynamics in which water repetitively interact with pore water, thanks to riverbed and porous media interface, which enters the alluvium and then emerges farther into the water body: this mixing is known as hyporheic exchange and significantly affects water mixing, riverine ecology, physical habitat as well as biological activity and riparian zones thanks to a saturated sediment volume called hyporheic zone.

If hydrodynamics, morphodynamics and mixing at river confluences were widely investigated in last decades using field, laboratory and numerical methods, a couple of studies have focused on surface-subsurface water interaction generated by above-mentioned driving factors at a river confluence Cheng et al. (2019) and a natural confluent bend Song et al. (2017).

1.1 Objectives and method of the thesis

This thesis takes its inspiration and structure from the works made by Song et al. (2017); Cheng et al. (2019) which were first investigations on the Juehe River and the Haohe River, based on field surveys concerning hydrodynamics, confluence



FIGURE 1.1: *Aerial View of Passau and the Confluence of the Inn (left), Danube (right) and the Ilz river (small river far right), Austria.*

topography, hydraulic conductivity tests and sediment column temperature profile. The objective of this thesis is to expand the knowledge about this important issue and, in particular, aims to understand how pressure gradients driven by a CHZ lead to spatial, temporal and seasonal variations of hyporheic exchange, throughout several months of observations, and, moreover, sediment layers, caused by its hydraulics, evolve and influence hydraulic permeability and, hence, the whole process.

This study presents two field surveys carried out in the south-west area of Marcellus (NY, USA). The aim was to describe hyporheic fluxes variations over different seasonal conditions and how typical confluence hydrodynamic zones are determining those patterns and rates. For this reason, field surveys lasted from September to December 2018 and from March to May 2019 over two confluences with different spatial scales. In fact, a total-station was firstly deployed to get confluences bathimetries, river banks and flood-plain areas. Soil samples were collected to obtain grain size distributions and hydraulic conductivity tests were conducted to represent sediment layer permeability. The final step was dedicated to collect hydraulics features such as vertical hydraulic gradients (VHG) and temperature profile time series of subsurface sediment to acquire the hyporheic exchange.

1.2 Structure of the thesis

The manuscript is organized in three parts with a total of 5 chapters as listed below:

- Part I, an illustration on problematic background and field campaigns aims and plans are presented within three chapters:
 - Chapter 2 illustrates a wide background of river confluences. In particular the objective is to analyse the variety of factors which characterise this fluvial systems such as planform geometry, junction angle, bed discordance and momentum ratio and how those elements influence flow structure, mixing, bed morphology and sediment transport.
 - Chapter 3 points out the relevance of the hyporheic zone: rates, spatial and temporal sales, flux mechanisms, its causing factors, how to delineate its area of interaction and some mentions on previous numerical and experimental studies.
 - Chapter 4 is focused on field surveys conducted in Marcellus (NY) on the two river confluences. Further more, methodology is presented:

instruments used to get most important confluence morphological features (bed bathymetry, banks and bars), porous media characterization (soil sample analysis and hydraulic conductivity tests), visual hydrodynamics observations of confluences, vertical hyporheic fluxes estimation through direct and indirect methods (PVC piezometers readings and subsurface water temperature profiles).

- Part II shows results and discussion concerning field surveys operated in Marcellus:
 - In Chapter 5 all field campaigns outcomes are exposed in detail. Firstly, morphology and hydraulics of confluences are showed after field surveys and visual observations. Secondly, porous media characteristics are outlined through grain size analysis and hydraulic conductivity tests obtained in situ. Finally, vertical hydraulic fluxes results are showed from piezometers and temperature rods data in relation to seasonal variations.
 - Chapter 6 is dedicated to the relationship between river confluences and pattern of hyporheic flux. The influence of confluence morphology and porous media features are analysed discussing BWC and NMC results. A comparison between piezometers readings and VFLUX method is presented as well.
- Part III are dedicated to main conclusions with further developments for future research in Chapter 7.

References

Cheng, D., J. Song, W. Wang, and G. Zhang

2019. Influences of riverbed morphology on patterns and magnitudes of hyporheic water exchange within a natural river confluence. *Journal of Hydrology*, 574:75 – 84.

Song, J., G. Zhang, W. Wang, Q. Liu, W. Jiang, W. Guo, B. Tang, H. Bai, and X. Dou

2017. Variability in the vertical hyporheic water exchange affected by hydraulic conductivity and river morphology at a natural confluent meander bend. *Hydrological Processes*, 31(19):3407–3420. HYP-16-0947.R2.

Part I

Chapter 2

Rivers confluence

This chapter most predominant factors of open-channel confluences hydrodynamics, morphodynamics and sediment transport are presented. Typical features of this fluvial system are individuated in planform geometry, flow momentum ratio, bed discordance and the gradation of bed sediment mixture. These elements are explained individually in reference with previous studies done on this peculiar case.

2.1 Introduction

In nature several bodies of water merge together forming larger open-channel rivers in which complex hydraulic processes take place. This meeting between two or more rivers is known as river confluence. They are nodal fluvial systems, where the combining flows converge and realign further downstream identifying a region also known as confluence hydrodynamic zone (CHZ). Velocity gradients in these non-uniform flows influence hydrodynamics, mixing, bed morphology, sediment transport, physical habitat as well as biological activity (Kozarek et al. 2010). In fact, riverine biodiversity may take advantage of the unusual morphology and hydraulics of this system (Franks et al. 2002) and, consecutively, the hydraulic complexity within the confluence (Gualtieri et al. 2017)

This zone has been investigated for decades through observations, field data,



FIGURE 2.1: *Confluence of the Mosel and Rhine Rivers in Koblenz, Germany.*

laboratory experiments and simplified models due to its challenging understanding. First attempts were undertaken using 1-D hydraulic models based on momentum flux changes at confluences (Taylor 1944; Webber and Greated 1966; Ramamurthy et al. 1988; Hager 1989; Hsu et al. 1998; Shabayek et al. 2002). This approach did not consider crucial processes, such as mixing and three-dimensional flow, and were overcome by hydrodynamic modelling (Biron et al. 2004; Baranya and Józsa 2007; Sandbach et al. 2018; Fingert et al. 2019). In this way, laboratory and field measurements were accompanied by numerical simulations giving the opportunity to analyse several factors (such as junction angle, bed roughness, bed morphology, velocity ratio etc.)(Constantinescu et al. 2012; Constantinescu 2014; Guillén Ludeña et al. 2017) supported by large eddy simulation (LES) (Ramos et al. 2019) or detached eddy simulation (DES) (Constantinescu et al. 2011). Nevertheless, models may have two important issues: first, confluence hydrodynamics

is a storage of flow mechanism such as mixing, turbulence and sediment transport which may be laborious for numerical simulations. Secondly, numerical modelling represents a particular challenge as a result of limits to effective computation over such large spatial scales: this is notably the case for issues regarding large river junctions. In the following subsection a quick review concerning river confluences is presented after Biron and Lane 2008a,b manuscripts.

2.2 Flow structure

Merging rivers velocities are commonly dissimilar which means that, at river confluence, they will cause curving and contraction of streamlines, determining bed morphology variations, such as erosion holes and shallow areas, that may generate, in extreme cases, problems for navigation and put in danger the stability of structures. As aforementioned, acceleration and deceleration are due to vortices generated by the mixing of the two currents. Factors which have a decisive influence on CHZ are: angle between the confluent channels (junction angle, α), the degree of concordance between channel beds, the orientation of these channels relative to the receiving channel (confluence planform geometry) and the momentum flux ratio. The latter, (M_r), is a metric that conveys the relative hydraulic importance of each confluent stream:

$$M_r = \frac{\rho_2 Q_2 U_{m2}}{\rho_1 Q_1 U_{m1}} \quad (2.2.1)$$

where ρ is water density, C is discharge, and U_m is mean downstream velocity while the subscripts 1 and 2 denote the main and tributary channel, respectively. Therefore, a momentum ratio of 1 means that convergent flows have the same momentum, values less than one indicate the main stream is dominant, and values greater than one indicate the tributary is dominant. First attempt to create a general model for confluence hydrodynamics was done by Mosley 1976 followed by Best 1987, 1988.

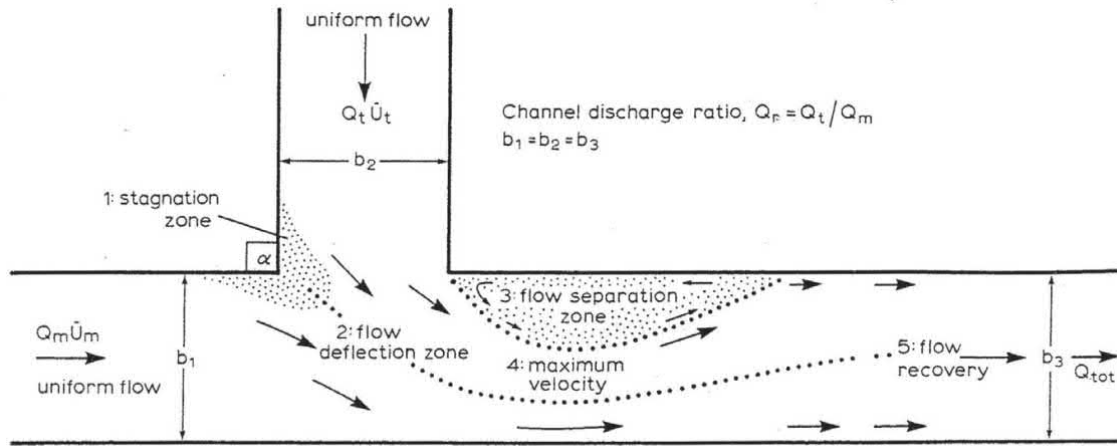


FIGURE 2.2: In the picture, the six zones may be appreciated. Figure from Best and Reid 1984.

Six different zones are usually located within this hydraulic system: a zone of stagnation at the junction apex, a zone of flow deflection, a zone of flow separation below the downstream junction, a zone of flow acceleration and maximum velocity, and a zone of gradual flow recovery (Figure 2.2). These regions define the CHZ where its extent depends on the distance over which the flow is influenced by pressure gradients caused by convergence and realignment flows. For instance, junction angle and planform symmetry on flow structure are variables well known and studied (Mosley 1976; Best and Reid 1984). In fact flow deflection is greater at high junction angles since tributary enters the main channel with higher lateral velocity (Figure 2.3). This generates shifted separation and acceleration zones. As junction angles approaches to zero, flow convergence and deflection decreases with the shear layer caused by parallel flow to become the dominant flow characteristic. Location of CHZ zones was demonstrated to be part of planform confluence geometry. There are two types: symmetrical confluences which have Y-shaped planforms, where flow deflection zone and zone of maximum velocity are located in the center of the downstream channel, and asymmetrical confluences, which have a receiving channel that is nearly collinear

with one of the upstream channels, with CHZ zones shifted towards the side of the CHZ associated with the main (receiving) tributary.

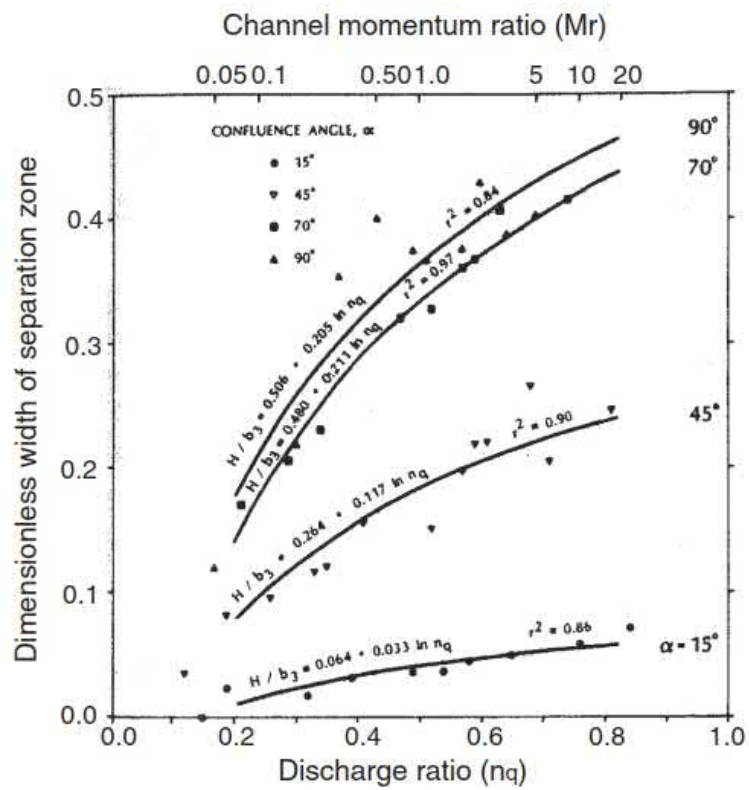
Further effect of planform geometry is related to secondary flow. As flows entering a confluence merge and mutually deflect one another, streamlines within each flow will curve, producing a centrifugal force oriented orthogonally to the path of curvature (Figure 2.4). centrifugal force causes flow streamlines to move toward the outer bank at the surface and toward the inner bank at the bed creating an helix effect.

Super-elevation of the water surface produced by flow curvature generates a pressure gradient force that balances the centrifugal acceleration, but only in a depth-averaged sense. Local imbalance between the two forces over depth results in spiral motion of the flow. This movement may be seen in two rotating cells which are converging at the surface in the centre of the channel, and diverging near the bed. At symmetrical confluences, both flows curve to a similar extent (assuming the momentum ratio equals one), and spiral flow is well-developed on both sides of the mixing interface (Rhoads 2006). An other aspect known as bed discordance may generate a situation where flow plunges into the CHZ, generally increasing turbulence, distorting the shear layer, and increasing pressure differences and causing streamlines to become disrupted.

Most of experimental and field studies have focused on headwater confluences where channel width are usually one order greater than depth . In large river systems, channel width reaches two or more orders of magnitude, where bank full channel width, channel depth and mean velocity increase non-linearly, as power functions of discharge. Those aspects were poorly understood in the past and new studies have been conducting in recent years on how confluence dynamics change with scale (Rhoads and Sukhodolov 2001; Rhoads et al. 2009; Szupiany et al. 2009; Konsoer and Rhoads 2014; Lewis and Rhoads 2015).

Gualtieri et al. 2018 showed first insights on hydrodynamics and processes at large-scale river confluences. In relatively high-flow condition, the separation region was longer, the maximum velocity zone seemed more downstream, and the extension of the CHZ was slightly larger and even its endpoint was more easily identified.

Lane et al. 2008 demonstrated that the distances required for mixing at large

FIGURE 2.3: Figure from Gurram *et al.* (1997).

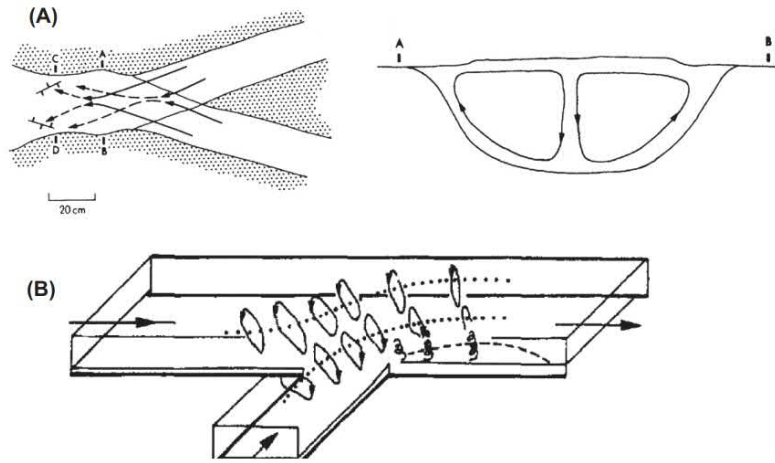


FIGURE 2.4: *Figure from Ashmore (1982).*

river junctions are often long, but can be very short, even within the same junction at different times (Río Paraná and Río Paraguay confluence, Argentina).

Ianniruberto et al. 2018 confirmed the results and models of previous studies, even though some unusual features were observed in a large rivers confluence that seemed to be related to past hydrological conditions (Negro and Solimões Rivers junction, Brazil).

2.3 Mixing at hydraulic confluence

Differences in velocities or momentum flux at a river confluence usually generates a shear layer that represents high levels of turbulence and large scale coherent structures. Therefore, the presence of two different water streams properties and suspended sediment concentration generates at confluences the existence of a visible interface between the tributaries, which can be quantified by using aerial photography and satellite images to analyze spectral properties of the water downstream of the confluence (Rhoads and Kenworthy 1995; Gaudet and Roy 1995; Rhoads and Kenworthy 1998; Kabeya et al. 2008). This process produces a



FIGURE 2.5: *River junction between Rio Negro and Rio Solimões, Manaus, Brazil.*

mixing and, in some cases, it may have a longer extension than the shear layer (Rhoads and Sukhodolov 2008). Mixing is traditionally separated into near, mid, and far field problems (Rutherford, 1994). Most transverse mixing problems are thought of as mid-field processes, occurring laterally and vertically which involve molecular diffusion (negligible in open-channel flow), turbulent diffusion, and advection.

At river confluence, due to the junction angle and planform geometry conformation, there are strong lateral and vertical components of flow developing within the CHZ increasing local momentum transfer both laterally and vertically. In recent years the process of lateral mixing in natural rivers has been of interest from many studies (Boxall and Guymmer 2003; Seo et al. 2006; Lane et al. 2008; Dow et al. 2009; Zhang and Zhu 2011). Transverse mixing in rivers, including confluences, is governed mainly by turbulent diffusion and advective transport (Rutherford 1994). The development of helical motion associated with flow curvature can produce large-scale transverse advection, greatly increasing rates of mixing at confluences. If bed discordance exists, distortion of the shear layer by lateral pressure gradients near the bed also can enhance advective mixing (Gaudet and Roy 1995; Biron et al. 2004).

The location of the mixing interface may be visualized by evaluating conservative property of the flow such as temperature, conductivity and pH. An other way is utilizing backscatter intensity (Gualtieri et al. 2019) to locate the interface. For instance, warm water tend to flow up while cold stream water, due to its higher density, falls to the bottom generating vertical mixing. The post-confluent flow can be considered mixed when cross-sectional temperature variance is sufficiently small. A complete vertical mixing is a rapid process with maximal dimensions of a few decades of the water depth. Complete lateral mixing, instead requires large distances. For typical river morphology ($W/h = 10$ to 100) the complete mixing will require from 100 to 1000 river widths' (where W is channel width and h is flow depth). In fact, further of this zone, mixing occurs only by molecular, random turbulence or secondary velocities.

In depth-limited environments, the dynamics of the mixing layer are strongly influenced by one dimension of the flow being much less than the other. In this case, the dynamics of mixing is strongly affected by friction, that constrain mixing layer growth, limiting the width of the mixing layer downstream of the point of initiation (Rhoads 2006). On large-scale confluences, in the absence of strong advective mixing within the confluence, shear-layer turbulence can dissipate before the two confluent flows are mixed (Rhoads and Sukhodolov 2004), instead.

Depending on the confluence geometry and morphology and the momentum flux ratio between the confluent flows, the mixing interface may be of Kelvin-Helmholtz or wake mode (Constantinescu et al. 2011, 2012). In the Kelvin-Helmholtz (KH) mode velocity and momentum ratio between the merging rivers is much higher than unity. The mixing interface contains predominantly co-rotating large-scale quasi-2D eddies whose growth is driven by the KH instability and vortex pairing which is the main growth mechanism of the mixing interface. In the wake mode, those ratios are close to unity and the stagnation region at the junction corner acts as the turbulent wake developing in the lee of an obstacle bounded by two shear layers. Downstream of the stagnation region, eddies from these layers are alternately shed into the mixing interface and merge into quasi 2D, counter-rotating vortices. Under these conditions, the mixing layer is in the wake mode, and the rate of growth of the mixing interface width is small compared to that of a mixing interface in the Kelvin-Helmholtz mode. The mixing layer width is given

by:

$$\delta = c_f \frac{\Delta V}{(\partial V_c / \partial y)_{max}} \quad (2.3.2)$$

where $V_c = (V1 + V2)/2$ is the depth-averaged velocity in the center of the mixing layer. It has been suggested that such cells are responsible for scour formation as a result of depression of the core of maximum velocity and/or intense shear towards the bed by downwelling flow. That phenomena is likely to be found in large river junctions where tributaries may gather a huge amount of sediments leading to distinct water densities between streams.

However, in more recent years a number of studies were conducted considering significant difference in density between the merging rivers. In this case, the denser river plunges and flows below the less dense river and the interface separating the confluent rivers tend to be inclined or nearly horizontal downstream of the plunge point: a conceptual model of horizontal shear layer was proposed by White and Helfrich (2013) and several field studies where conducted (Lane et al. 2008; Ramón et al. 2013; Gualtieri et al. 2019). Then, the location of the mixing interface was found to be closely related to discharge ratio between the tributaries: it may shift to one tributary to an other one as varying the discharge ratio.

2.4 Bed morphology

The bed morphology can be related to confluence flow structure and its different hydrodynamics zones (Section 2.2). Based on these factors, morphological features can be identified at channel confluences:

- a scour hole whose origin is linked to increased velocities and turbulence within the junction;
- a region of sediment accumulation close to the upstream confluence corner, perhaps related to flow separation zone;
- bars which can be tributary-mouth, mid-channel or bank-attached.

As scour holes are concerned, several studies have been carried out to explain depth and width growth and dimension, since they have an important engineering significance within structures design. In symmetric and asymmetric confluences, scour hole axis of symmetry may bisect junction angle. Ranging from small to large river confluences, scour holes may be found with various width while studies detailing scour depths at river channel confluences include those of Mosley (1975, 1976), Best (1988), Ashmore and Parker (1983), Rezaei et al. (1999), Bryan and Kuhn (2002), Ghobadian and Shafai Bajestan (2007).

Scour depth has been studied for decades and Best (1988) discovered that the location of the maximum depth is related to the discharge ratio between the streams. Mosley (1975, 1976), instead, found that the depth of scour became greater with an increasing junction angle. In an other study by Bryan and Kuhn (2002) was found that planform had a more influence on scour hole rather than junction angle. Moreover, scour holes tend to be, in a Y-shape confluence, symmetric in planform shape. Asymmetrical confluence, instead, usually have more complex scour holes which affect also bed morphology.

There is an aspect which relates bed morphology to flow structure: sediment transport. This phenomena is still under investigation within CHZ, particularly bedload transport. It has been provided that, under steady conditions and symmetrical confluence, most sediment move aside the scour hole rather than through it, and its cause can be addressed to the hydrodynamic produced by the scour hole, like helical flow cells (Mosley 1976). However, as sediment load increases with constant flow and junction, scour hole depth decreases as sediment transport passes it over. That mechanism, of course, has to deal with several parameters such as junction angle and confluence asymmetry. Experimental findings showed that sediment load of each stream are separated and it becomes higher as angle junction, mutual deflection of the incoming flows and scour depth increments (Nazari-Giglou et al. 2016; Guillén Ludeña et al. 2017). Discharge also adjust sediment flow and reshape the river morphology which is actively evolving, especially during high flow conditions. Therefore, spatial patterns of sediment transport need further studies to be characterized due to its complexity.

There are others effects as a result of complex confluence flow structure and angle junction: formation of sandy bars. Tributary-mouth bars, which are located

near the beginning of the junction, depend on discharges ratio, or momentum. In fact, its penetration into the junction is affected by floods as well. The presence of a dam upstream may restrict channels and improve tributary-mouth bars size. Sandy bars are clearly visible also in middle of the post-confluence channel. That happens especially when there are Y-shape confluences which cause convergence of sediment transport downstream of junction scour. Moreover, further the flow acceleration zone where flow recovers due to shear layer dissipation, the flow inevitably leaves sediments on the bottom.

There is still the possibility to have bars in region of flow separation/expansion formed downstream the junction. It has been observed, within the flow separation zone, that small velocities produce deposition of fine-grained bar in that region. Those sediments may come from bedload or entrainment into the separation zone. Eventually, the stagnation zone, formed at upstream rivers junction, may have bars even though they are not so evident and distinct but can reflect flow patterns of upstream flow.

References

- Ashmore, P. and G. Parker
1983. Confluence scour in coarse braided streams. *Water Resources Research*, 19(2):392–402.
- Ashmore, P. E.
1982. Laboratory modelling of gravel braided stream morphology. *Earth Surface Processes and Landforms*, 7:201–255.
- Baranya, S. and J. & Józsa
2007. Numerical and laboratory investigation of the hydrodynamic complexity of a river confluence. *Periodica Polytechnica Civil Engineering*, 51(1):3–8.
- Best, J. L.
1987. *Recent Developments in Fluvial Sedimentology*, chapter Flow dynamics at river channel confluences: Implications for sediment transport and bed morphology. Society of Economic Palaeontologists and Mineralogists Special Publication 39.
- Best, J. L.
1988. Sediment transport and bed morphology at river channel confluences. *Sedimentology*, 35(3):481–498.
- Best, J. L. and I. Reid
1984. Separation zone at open-channel junctions. *Journal of Hydraulic Engineering*, 110:1588–1594.
- Biron, P. M. and S. N. Lane
2008a. *River Confluences, Tributaries and the Fluvial Network*, chapter Modelling

- hydraulics and sediment transport at river confluences, Pp. 17–38. John Wiley & Sons, Ltd.
- Biron, P. M. and S. N. Lane
2008b. *River Confluences, Tributaries and the Fluvial Network*, chapter Sediment transport, bed morphology and the sedimentology of river channel confluences, Pp. 45–68. John Wiley & Sons, Ltd.
- Biron, P. M., C. Robson, M. F. Lapointe, and S. J. Gaskin
2004. Comparing different methods of bed shear stress estimates in simple and complex flow fields. *Earth Surface Processes and Landforms*, 29(11):1403–1415.
- Boxall, J. B. and I. Guymer
2003. Analysis and prediction of transverse mixing coefficients in natural channels. *Journal of Hydraulic Engineering*, 129(2).
- Bryan, R. B. and N. J. Kuhn
2002. Hydraulic conditions in experimental rill confluences and scour in erodible soils. *Water Resources Research*, 38(5):21–1–21–13.
- Constantinescu, G.
2014. Le of shallow mixing interfaces: A review. *Environmental Fluid Mechanics*, 14(5):971–996.
- Constantinescu, G., S. Miyawaki, B. Rhoads, and A. Sukhodolov
2012. Numerical analysis of the effect of momentum ratio on the dynamics and sediment-entrainment capacity of coherent flow structures at a stream confluence. *Journal of Geophysical Research: Earth Surface*, 117(F4).
- Constantinescu, G., S. Miyawaki, B. Rhoads, A. Sukhodolov, and G. Kirkil
2011. Structure of turbulent flow at a river confluence with momentum and velocity ratios close to 1: Insight provided by an eddy-resolving numerical simulation. *Water Resources Research*, 47(5).
- Dow, K. E., P. M. Steffler, and D. Z. Zhu
2009. Case study: Intermediate field mixing for a bank discharge in a natural river. *Journal of Hydraulic Engineering*, 135(1).

- Fingert, E., I. Krylenko, V. Belikov, P. Golovlyov, A. Zavadskii, and M. Samokhin
2019. Two-dimensional hydrodynamic modelling of channel processes and floods characteristics at the confluence of the amur and zeya rivers. *Proceedings of the International Association of Hydrological Sciences*, 381:73–77.
- Franks, C., S. Rice, and P. Wood
2002. *The Structure, Function and Management Implications of Fluvial Sedimentary Systems.*, volume 276, chapter Hydraulic habitat in confluences: an ecological perspective on confluence hydraulics., Pp. 61–67. Wallingford, UK: International Association Hydrological Sciences.
- Gaudet, J. M. and A. G. Roy
1995. Effect of bed morphology on flow mixing length at river confluences. *Nature*, 373:138–139.
- Ghobadian, R. and M. Shafai Bajestan
2007. Investigation of sediment patterns at river confluence. *Journal of Applied Sciences*, 7(10):1372–1380.
- Gualtieri, C., N. Filizola, M. de Oliveira, A. M. Santos, and M. Ianniruberto
2018. A field study of the confluence between negro and solimes rivers. part 1: Hydrodynamics and sediment transport. *Comptes Rendus Geoscience*, 350(1):31 – 42. Rivers of the Andes and the Amazon Basin: Deciphering global change from the hydroclimatic variability in the critical zone.
- Gualtieri, C., M. Ianniruberto, and N. Filizola
2019. On the mixing of rivers with a difference in density: The case of the negro/solimes confluence, brazil. *Journal of Hydrology*, 578:124029.
- Gualtieri, C., M. Ianniruberto, N. Filizola, R. Santos, and T. Endreny
2017. Hydraulic complexity at a large river confluence in the amazon basin. *Ecohydrology*, 10(7):e1863. e1863 ECO-16-0135.R3.
- Guillén Ludeña, S., Z. Cheng, C. G., and M. J. Franca
2017. Hydrodynamics of mountain-river confluences and its relationship to sediment transport. *Journal of Geophysical Research: Earth Surface*, 122(4):901–924.

- Gurram, S. K., K. Karki, and W. H. Hager
1997. Subcritical junction flow. *Journal of Hydraulic Engineering*, 123:447–455.
- Hager, W.
1989. Transitional flow in channel junctions. *Proc. ASCE, Journal of Hydraulic Engineering*, Vol. 115(HY No 2,):243–259. [92].
- Hsu, C. C., W. J. Lee, and C. H. Chang
1998. Subcritical open channel junction flow. *Journal of Hydraulic Engineering*, 124:847–855.
- Ianniruberto, M., M. Trevethan, A. Pinheiro, J. F. Andrade, E. Dantas, N. Filizola, A. Santos, and C. Gualtieri
2018. A field study of the confluence between negro and solimes rivers. part 2: Bed morphology and stratigraphy. *Comptes Rendus Geoscience*, 350(1):43 – 54.
Rivers of the Andes and the Amazon Basin: Deciphering global change from the hydroclimatic variability in the critical zone.
- Kabeya, N., T. Kubota, A. Shimizu, T. Nobuhiro, Y. Tsuboyama, S. Chann, and N. Tith
2008. Isotopic investigation of river water mixing around the confluence of the tonle sap and mekong rivers. *Hydrological Processes*, 22(9):1351–1358.
- Konsoer, K. M. and B. L. Rhoads
2014. Spatial-temporal structure of mixing interface turbulence at two large river confluences. *Environmental Fluid Mechanics*, 14(5).
- Kozarek, J., W. Hession, C. Dolloff, and P. Diplas
2010. Hydraulic complexity metrics for evaluating in-stream brook trout habitat. *Journal of Hydraulic Engineering*, 136(12):1067–1076.
- Lane, S. N., D. R. Parsons, J. L. Best, O. Orfeo, R. A. Kostaschuk, and R. J. Hardy
2008. Causes of rapid mixing at a junction of two large rivers: Rarand raraguay, argentina. *Journal of Geophysical Research: Earth Surface*, 113(F2).

- Lewis, Q. W. and B. L. Rhoads
2015. Rates and patterns of thermal mixing at a small stream confluence under variable incoming flow conditions. *Hydrological Processes*, 29(20):4442–4456.
- Mosley, M. P.
1975. *An experimental study of channel confluences*. PhD thesis, Colorado State University.
- Mosley, M. P.
1976. An experimental study of channel confluences. *Journal of Geology*, 84:535–562.
- Nazari-Giglou, A., A. Jabbari-Sahebari, A. Shakibaeinia, and S. M. Borghei
2016. An experimental study of sediment transport in channel confluences. *International Journal of Sediment Research*, 31(1):87 – 96.
- Ramamurthy, A. S., L. B. Carballada, and D. M. Tran
1988. Combining open channel flow at right-angled junctions. *Journal of Hydraulic Engineering*, 114(1449-1460).
- Ramón, C. L., A. B. Hoyer, J. Armengol, J. Dolz, and F. J. Rueda
2013. Mixing and circulation at the confluence of two rivers entering a meandering reservoir. *Water Resources Research*, 49(3):1429–1445.
- Ramos, P. X., L. Schindfessel, J. P. P, and T. D. Mulder
2019. Influence of bed elevation discordance on flow patterns and head losses in an open-channel confluence. *Water Science and Engineering*, 12(3):235 – 243.
- Rezaur, R., A. W. Jayawardena, and M. M. Hossain
1999. *River Sedimentation: Theory and Applications*, chapter Factors affecting confluence scour, Pp. 187–192. Balkema: Rotterdam.
- Rhoads, B. L.
2006. Scaling of confluence dynamics in river systems: Some general considerations. In *River, Coastal and Estuarine Morphodynamics*, River, Coastal and Estuarine Morphodynamics: RCEM 2005 - Proceedings of the 4th IAHR Symposium on River, Coastal and Estuarine Morphodynamics, Pp. 379–387.

- Rhoads, B. L. and S. T. Kenworthy
1995. Flow structure at an asymmetrical stream confluence. *Geomorphology*, 11(4):273 – 293.
- Rhoads, B. L. and S. T. Kenworthy
1998. Time-averaged flow structure in the central region of a stream confluence. *Earth Surface Processes and Landforms*, 23(2):171–191.
- Rhoads, B. L., J. D. Riley, and D. R. Mayer
2009. Response of bed morphology and bed material texture to hydrological conditions at an asymmetrical stream confluence. *Geomorphology*, 109(3):161 – 173.
- Rhoads, B. L. and A. N. Sukhodolov
2001. Field investigation of three-dimensional flow structure at stream confluences: 1. thermal mixing and time-averaged velocities. *Water Resources Research*, 37(9):2393–2410.
- Rhoads, B. L. and A. N. Sukhodolov
2004. Spatial and temporal structure of shear layer turbulence at a stream confluence. *Water Resources Research*, 40(6).
- Rhoads, B. L. and A. N. Sukhodolov
2008. Lateral momentum flux and the spatial evolution of flow within a confluence mixing interface. *Water Resources Research*, 44(8).
- Rutherford, J. C.
1994. *River mixing*, volume 23. Chichester, UK: John Wiley & Sons. ISBN 0-471-94282-0.
- Sandbach, S., A. Nicholas, P. Ashworth, J. Best, C. Keevil, D. Parsons, E. Prokocki, and C. Simpson
2018. Hydrodynamic modelling of tidal-fluvial flows in a large river estuary. *Estuarine, Coastal and Shelf Science*, 212:176–188.

- Seo, I., K. O. Baek, and T. M. Jeon
2006. Analysis of transverse mixing in natural streams under slug tests. *Journal of Hydraulic Research*, 44(3):350–362.
- Shabayek, S., P. Steffler, and F. Hicks
2002. Dynamic model for subcritical combining flows in channel junctions. *Journal of Hydraulic Engineering*, 128:821–828.
- Szupiany, R. N., M. L. Amsler, D. R. Parsons, and J. L. Best
2009. Morphology, flow structure, and suspended bed sediment transport at two large braid-bar confluences. *Water Resources Research*, 45(5).
- Taylor, E. H.
1944. Flow characteristics at rectangular open-channel junctions. *Transactions of the American Society of Civil Engineers*, 109(1):893–902.
- Webber, N. B. and C. A. Greated
1966. An investigation of flow behaviour at the junction of rectangular channels. *Proceedings of the Institution of Civil Engineers*, 34(3):321–334.
- White, B. L. and K. R. Helfrich
2013. Rapid gravitational adjustment of horizontal shear flows. *Journal of Fluid Mechanics*, Pp. 86–117.
- Zhang, W. and D. Z. Zhu
2011. Transverse mixing in an unregulated northern river. *Journal of Hydraulic Engineering*, 137(11).

Chapter 3

Hyporheic fluxes

In this chapter a brief literature review of hyporheic exchange is given. Some knowledge concerning surface-subsurface water exchange is presented concerning its structure, rate, spatial and temporal scale. How the hyporheic zone is defined and set of equations used to describe the intricate relation between water column and sediment layer. Secondly, most used field techniques and methods to obtain hyporheic fluxes are given and a few numerical studies are showed. In the end a couple of precedent field studies are exposed to analyse the existing gap between literature and this study is concerned.

3.1 Introduction

Bodies water repetitively interact with pore water thanks to stream bed and porous media interface. That mixing is usually called hyporheic fluxes which affect all the surrounding and underneath zones of stream water (transversal, longitudinal and vertical) (Elliott and Brooks 1997; ?; Triska et al. 1989; Packman and Bencala 2000; Marion et al. 2002; Tonina and Buffington 2007; Tonina 2008). Hyporheic fluxes area investigation was exhaustively discussed in Tonina and Buffington 2009 from which the present section is inspired and follows its outline. This exchange is characterized by river waters entering the streambed sediment in downwelling areas, (i.e., downwelling fluxes) and then emerging into the stream in upwelling areas, (i.e., upwelling fluxes). This water exchange varies due to spatial and temporal variations of channel features (hydraulic conductivity, stream morphology,

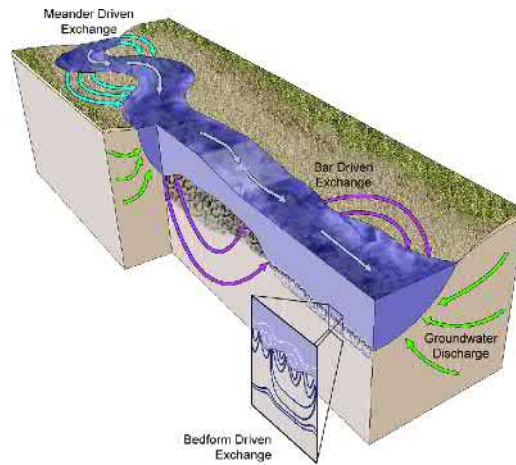


FIGURE 3.1: *Horizontal and vertical variability of hyporheic exchange. Image from Stonedahl et al. (2010).*

streambed pressure distribution, groundwater level, sediment transport, etc) and it can be longitudinal or transversal to the stream direction. The hyporheic exchange affects significantly surface and subsurface water quality, riverine habitat for aquatic and terrestrial organisms and plays an important role in preserving and conserving riverine systems. Concepts, environmental aspects and methods for measuring and assessing hyporheic fluxes and zone are summary described in this section.

3.2 Structure, rates and scale of hyporheic exchange

The hyporheic exchange develops over multiple embedder scales, resulting in different spatial extents. This feature determines various exchange rates and residence time (temporal length that river water spends traversing the subsurface sediment before re-emerging into the stream). The latter is a critical characteristic of hyporheic zone since biological and chemical processes depend on the amount of time that river water is in contact with the groundwater environment. It may be defined

- micro scale (1)
- channel unit scale (2)
- channel reach scale (3)
- valley segment scale (4)

The case of (1), the exchange happens essentially by variation of head around wood debris, salmon redds, or protruding streambed particles; scale of exchange is up to a channel width (W) in length. (2) head variations around individual bedforms (pools, bars, steps); up to several W . (3) channel reach (e.g. changes in reach slope, meso-scale changes in alluvial volume, flow through the floodplain between meander bends, or cross-valley head differences between the main channel and secondary channels; tens of W and (4) is mainly caused by changes in valley confinement, alluvial volume, or underlying bedrock topography; hundreds to thousands of W .

While (3) and (4) have temporal and spatial scales are influenced by broad-scale changes in channel properties, hyporheic exchange varies frequently at channel reach-scale, in terms of differences in bed topography and corresponding influences on head variations. In general, the range of mechanisms causing hyporheic exchange increases as one moves from steep, confined channels to lower-gradient, unconfined ones. Different channel topographies, will have different pressure-head profiles and different potentials for hyporheic exchange. For instance, in cascade channels, due to its bed topography, short and fast hyporheic circulation cells under each boulder obstruction will be found. On the other hand, featureless topography of plane-bed channels will have limited hyporheic exchange pressure variations due to local occasional circulation around sporadic obstructions. There are other cases where head variations matter more than topography: dune-ripple and pool-riffle channels have strong downstream pressure head variations generating well-formed hyporheic paths.

Channel slope and depth of alluvium also influence vertical extent and residence time of the exchange. In fact, shallow depths results in short, fast, flow

paths, while steep valley slopes should cause greater hyporheic underflow. confinement across these morphologies also create differences in lateral complexity of the river valley that affect head gradients and hyporheic exchange.

Cascade and step-pool channels are expected to have high magnitudes of exchange due to large head gradients and porous sediment (high hydraulic conductivity), but steep valley slopes and small alluvial volumes will limit the scale of exchange for these channels. In contrast, braided, pool-riffle and dune-ripple channels are expected to have moderate magnitudes of hyporheic exchange due to more gentle head gradients and finer bed material. Plane-bed channels are underlain by thicker alluvial packages, but lack of bed topography will limit the magnitude and scale of hyporheic exchange that can be developed. Finally, bedrock channels should have the smallest magnitudes and scales of hyporheic exchange due to the limited occurrence of alluvial patches.

3.3 The hyporheic zone outlining methods

In literature, three macro approaches are used for studying hyporheic fluxes dynamics. The first is the biological method which observes the presence of organisms, carrying oxygen extremely important for salmonid embryos incubating in their egg-nests, below to streambed surface. These habitats have water properties more similar to those of the surface water than subsurface waters. For this reason this method defines the zone by the presence-absence of hyporheic fauna, called hyporheos.

The second, the geochemical, defines the hyporheic zone as the volume of sediment containing an arbitrary amount traditionally set at least 10% of surface water (Triska et al. 1989). Consequently, the hyporheic zone is a transitional zone where surface and subsurface waters mix. The last method, the hydraulic one, is based on the concept of hyporheic flow paths, which are the trajectories of stream water moving through the streambed sediment between its downwelling and upwelling points (Cardenas et al. 2004; Tonina and Buffington 2007). This method defines the hyporheic zone as the volume of streambed sediment enveloped by all the flow paths of hyporheic exchange that begins at stream bed and ends on its banks.

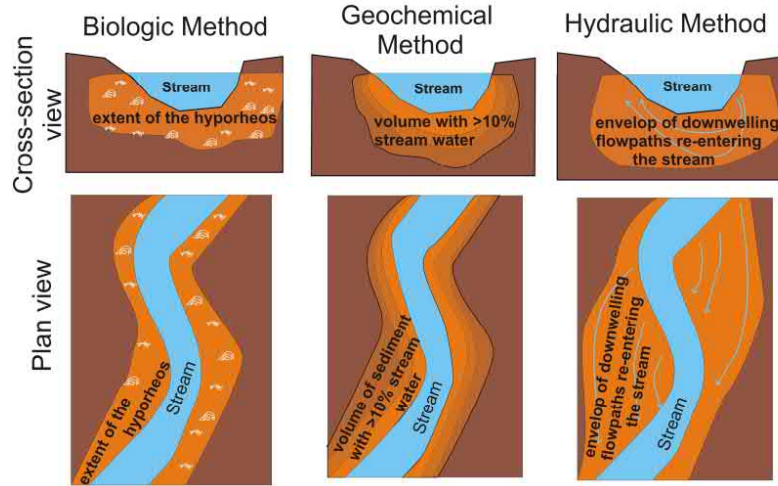


FIGURE 3.2: *The three method comparison. Figure from Tonina and Buffington (2009).*

The three methods may lead to different delineating zones. Where biological and geochemical zones do not set any condition to stream water returning to stream, the hydraulic approach do not take into account hyporheic fluxes which are lost into the ground. As may be seen, an unique hyporheic zone can not be found properly. Anyway, as this study is concerned, the third approach will be using for the following applications.

3.4 Flux mechanism

By assuming a fixed in space infinitesimal volume, the mass balance of water equation can be used for describing the hyporheic exchange. The volume is saturated with lateral sides parallel to the hyporheic flow (no-lateral exchange), bottom side at an impervious layer (no flow) and upper surface at the water-sediment interface. As a consequence, the temporal change of the volume of water, V_w , within the volume depends on the subsurface inflow Q and outflow $Q + dQ/dx \cdot$

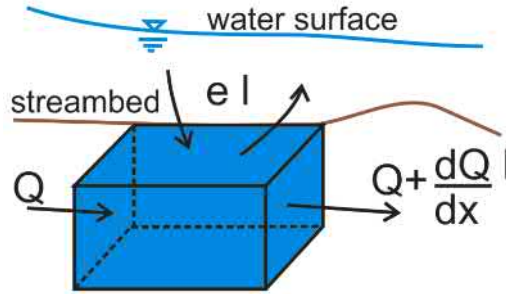


FIGURE 3.3: Hyporheic exchange, e , per unit length for an infinitesimal volume of length, l , of the hyporheic zone, modified from Tonina and Buffington (2009).

dl , where dl is the infinitesimal length of the volume, and the hyporheic exchange e per unit length, such that:

$$\frac{dV_W}{dt} = Q - \left(Q + \frac{dQ}{dx} dl \right) + e \cdot dl = \left(e - \frac{dQ}{dx} \right) dl \quad (3.4.1)$$

For steady-state conditions, V_w does not change with time $dV_W/dt = 0$, and $e = dQ/dx$. Taking into account the Darcy (1856) equation, the equation becomes:

$$Q = qA = -K_C \frac{dh}{dx} A \quad (3.4.2)$$

where q is the subsurface flux ($q = n u$, where n is the sediment porosity and u the interstitial flow velocity), K_C is the hydraulic conductivity of the sediment, and dh/dx is the spatial gradient of the energy head, the hyporheic exchange is:

$$e = \frac{d \left(-K_C \frac{dh}{dx} A \right)}{dx} = -K_C A \frac{d^2 h}{dx^2} - K_C A \frac{dA}{dx} \frac{dh}{dx} - A \frac{dK_C}{dx} \frac{dh}{dx} \quad (3.4.3)$$

This equation shows that e is driven by (3.4.1) spatial changes in the energy head, $(d^2 h/dx^2)$, (3.4.2) spatial changes in the cross-sectional area of alluvium

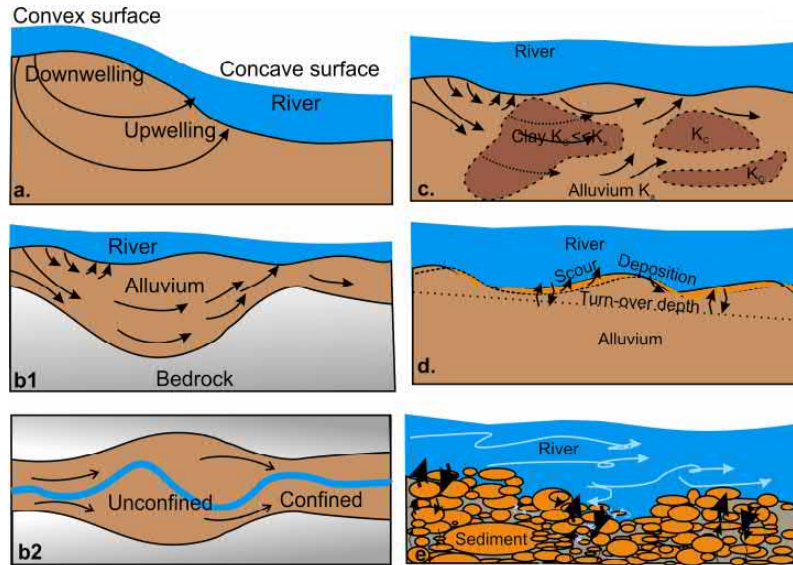


FIGURE 3.4: Figure from Tonina and Buffington (2009).

(dA/dx) , and (3.4.1) spatial changes in hydraulic conductivity (dK_C/dx). (Tonina (2008)).

Furthermore, as the energy head varies its curvature, upwelling or downwelling flow may be found (concave and convex respectively). In addition to this, hyporheic depth extension and distribution is affected by amplitude and wavelength of the head surface. These areas can be also be visualized when water surface approximates the energy grade line: this situation requires particular streambed and flow conditions which may be difficult to find in natural channels. However, observing water surface might be a initial hyporheic path approximation.

3.5 Hyporheic exchange causing factors

Most influencing causing factor of hyporheic exchange is variation in pressure distribution. Bed morphology, in streams and rivers, is discontinuous creating

zone of high and low pressures: for instance, bedforms induce surface-subsurface water exchange. Flow obstruction, such as river steps, also drives hyporheic circulation in prescribed paths (Endreny et al. 2011). The problem may be studied through the total streambed pressure:

$$H = z + h + C_d \frac{V^2}{2g} \quad (3.5.4)$$

where z is the bed elevation, the static pressure head and $C_d \frac{V^2}{2g}$ the dynamic pressure head (where V is mean velocity, g is gravitational acceleration and C_d is a generic loss coefficient representing changes in momentum due to form drag or channel contraction/expansion).

Each of these pressure components alters due to several factors such as bed topography, channel flow and hydraulics. It might be seen how bedforms can modifies bed elevation inducing surface-subsurface water exchange (Janssen et al. 2012; Constantz et al. 2013): these formations influence water surface elevation affecting hyporheic patterns. Increase in flow depth reduces static pressure head gradients giving a more uniform surface water profile while decrease or rise in velocity and dynamic pressure head gradients may develop different water exchanges depending on flow separation or bedform shape. As turbulence effects on hyporheic exchange are concerned, that depends on topography that minimize or enhance flow separation: a steep lee side bedforms angle induces a stagnation zone where a stronger hyporheic flux can be observed.

As mentioned before, many logs and other woody debris that fall into channels create flow interferences which affect hydraulics and river forms. Obstructions may also be generated by aquatic organisms which modify bed topography, nutrient fluxes and local pressure distribution.

More causes of pressure variations may involve channel sinuosity (Demaria et al. 2008), sudden changes in river width and depth, turbulent mixing at river confluences as well.

The term (dA/dl) of equation (3.4.3) is the spatial changes of alluvial area. A decrease in its volume generates an expulsion of pore water into the stream (upwelling flux) while an increase of the subsurface volume implicates discharge

into substrate sediments (downwelling flux). These variations occur due to downstream changes in alluvial depth or channel width. Sometimes an irregular bedrock is covered by alluvium and create strange spatial variation in substrate depth driving hyporheic exchange into confined spaces.

These volumes increase usually in downstream mountain basins where slope are steeper: sediment supply enhances. Spatial variations in river profile are also given by tributary bedload transport which partially modifies downstream river bed morphology.

Its composition is crucial as well: an heterogeneous alluvium can obstruct and modifies hyporheic fluxes. The permeability of near-surface sediment determines the exchange: This brings attention to quantify the stratigraphy of subsurface sediments composition for accurate modelling of hyporheic exchange.

Therefore, this consideration can be explained by the term (dK/dl) within the equation (3.4.3) known as hydraulic conductivity. The latter is a crucial parameter which is often measured in situ for modelling hyporheic fluxes. As it is known that depends on sediment porosity and connectivity of pores, it varies horizontally and vertically within alluvial volume. In fact, alluvial valleys are a mesh of different sediment patches and hydraulic conductivity. From the experience gained, a permeable substrate allows an higher subsurface flow (higher K) with downwelling fluxes mainly, whereas a lower hydraulic conductivity indicates a low penetrable sediment volume provoking upwelling fluxes, because of excess of water to be expelled into the stream. Therefore, a sediment heterogeneity causes a spatial variability and magnitude of hyporheic exchange in sand-bed streams mostly.

There are other influencer factors for the surface-subsurface water fluxes: bedload transport and turbulence fluctuations. The first causes a mechanical mixing of the stream bed material. Taking into account a riverbed characterized of bedforms, erosion effects tend to reshape dunes and ripples: in particular stoss side dune sediments move towards the lee side bedform depositing themselves. This process potentially alters the volume of hyporheic exchange by bedforms movement.

The second occurs thank to permeable riverbed sediments. Near-bed turbulence is generated by various factors such as large-scale flow structures, turbulent

scale wakes behind flow obstacles and local obstructions on the bed (Ridolfi et al. 2010). However, turbulent fluctuation to be effective needs to penetrate into the sediment: they usually reach a depth of 2-10 times the mean diameter of the bed material. Turbulent diffusion causes nonlinear behaviour due to the occurrence of inertial forces. The consequence is a modification of the head distribution with a consequent hyporheic exchange patterns compared to that of an impermeable bed.

3.6 Measurement of the hyporheic exchange

Many methods exist to measure the extent and the magnitude of hyporheic exchange. There are numerical approaches (CFD simulations e.g.) or laboratory/direct observations. The easiest procedure, and common field technique, needs to insert a mini-well into the subsurface sediment in order to obtain the vertical head gradient (VHG).

$$VHG = \frac{\Delta h}{z} \quad (3.6.5)$$

where VHG is the difference in water elevation between the piezometer and the stream level Δh divided by the sediment column below the streambed z . That indicates direction and strength of water exchange between the surface and subsurface water: positive/negative values indicate upwelling/downwelling, respectively, while zero indicates no exchange.

In field campaigns, a fine mesh of piezometers can, without difficulty, individuate hyporheic fluxes pattern: accuracy depends on instrument extent which has to be taken into account. Passive tracers (salt, rhodamine and other) may be utilized to estimate surface-subsurface water flux rate and scale. The exchange, by using this approach, is obtained from the breakthrough curve. Natural tracers, instead, have been widely using in recent years. The easiest natural tracer is water temperature: recent studies have brought to light the temperature pipe technique (Anibas et al. 2009, 2011). A PVC pipe is equipped with thermistors at different depths. Each of these is thermically isolated and records water temperature

data. Once the time series is given by the pipe, a one dimensional conduction-advection-dispersion equation:

$$\frac{\delta T}{\delta t} = \kappa_e \frac{\delta^2 T}{\delta z^2} - q \frac{C_w}{C} \frac{\delta T}{\delta z} \quad (3.6.6)$$

where T is temperature, z is vertical coordinate, κ_e is effective thermal diffusivity, q is fluid flux, C_w is the volumetric heat capacity of the saturated streambed, and C is the volumetric heat capacity of the saturated sediment calculated as the mean of C_w and C_s , the volumetric heat capacity of the sediment grains, weighted by total porosity Stallman (1960); Hatch et al. (2006); Keery et al. (2007). The effective thermal diffusivity is defined as:

$$\kappa_e = \frac{\lambda_0}{\rho c} + \beta |v_f| \quad (3.6.7)$$

where λ_0 is the baseline thermal conductivity (in the absence of fluid flow), excluding the effects of dispersion, β is thermal dispersivity, and c and ρ are specific heat and density of the sediment-water system respectively and v_f is the linear particle velocity. The second term in Equation 3.6.7 represents the increase in effective thermal diffusivity caused by hydrodynamic dispersion and it is often assumed to have little influence in models with modest fluid flow rates Hatch et al. (2006). The solution of equation (3.6.6) with periodic sinusoidal temperature variations as boundary conditions at the streambed and a thermal gradient equal to zero at an infinite streambed depth is:

$$T(z, t) = A_S \exp \left(\frac{\nu z}{2\kappa_e} - \frac{z}{2\kappa_e} \sqrt{\frac{\alpha + \nu^2}{2}} \right) \cos \left(\frac{2\pi t}{P} - \frac{z}{2\kappa_e} \sqrt{\frac{\alpha + \nu^2}{2}} \right) \quad (3.6.8)$$

where A_S is the amplitude of the surface temperature signal, $\alpha = \sqrt{\nu^4 + (8\pi \cdot \kappa_e / P)^2}$, P is the period of temperature variations (one day) and $\nu = v_f / \gamma$ ($\gamma = C_w / C_s$). The Hatch et al. (2006) method splits equation (3.6.8) into components solving for seepage fluxes based on the observed amplitude ratio (A_r):

$$AR = \frac{A_L}{A_S} = \exp \left[\frac{Z_L - Z_S}{2\kappa_e} \left(v - \sqrt{\frac{\alpha + v^2}{2}} \right) \right] \quad (3.6.9)$$

and phase shift (time lag $\Delta\phi$)

$$\Delta\phi = \phi_L - \phi_S = \exp \left[\frac{Z_L - Z_S}{2\kappa_e} \sqrt{\frac{\alpha - v^2}{2}} \right] \quad (3.6.10)$$

where A_L , A_S , ϕ_L , ϕ_S , Z_L and Z_S represent the amplitude, phase and vertical coordinate (subscript S and L indicate shallowest and lowest sensor, respectively). Equations (3.6.9) and (3.6.10) are reordered to obtain velocity of a thermal front as function of amplitude and phase:

$$q = \frac{C_w}{C} \left(\frac{2\kappa_e}{\Delta_z} \ln A_r + \sqrt{\frac{\alpha + v^2}{2}} \right) \quad (3.6.11)$$

$$|q| = \frac{C_w}{C} \sqrt{\alpha - 2 \left(\frac{\Delta\phi 4\pi\kappa_e}{P\Delta_z} \right)} \quad (3.6.12)$$

Both (3.6.11) and (3.6.12) require to be solved iteratively (or by optimization) and depend on thermal sensitivity which is estimated on empirical ranges. The advantage of using this method is its extreme user-friendly feature.

During winter season, as shown in literature (Hyun et al. 2011; Gariglio et al. 2013; Song et al. 2017), a steady-state condition may be applied by solving the following implicit equation (Bredehoeft and Papadopoulos 1965):

$$\beta = \frac{\gamma q \Delta L}{\kappa_e} \quad (3.6.13)$$

$$\frac{T(z) - T_S}{T_L - T_S} = \frac{e^{\frac{\beta z}{\Delta L}} - 1}{e^\beta - 1} \quad (3.6.14)$$

where T_S and T_L indicate the temperatures at the surface and at the lowest recorded sensor, respectively with ΔL the distance between the two sensors, and $T(z)$ is the temperature at a generic location z between S and L .

Laboratory experiments have shown promising results towards the understanding of the phenomena. A teaching flume is usually installed with a rocky-gravel shaped bed where a coloured dye is injected at crucial points of the model (Endreny et al. 2011). Pressure gradients make hyporheic exchange visible thanks to trajectories left by upwelling or downwelling fluxes. Many laboratory experiments and field campaign have been carried out regarding river confluences (Rhoads and Kenworthy 1995, 1998) as well as hyporheic exchange (Endreny et al. 2011; Hyun et al. 2011; Jiang et al. 2015) but a few had their focus on the combination of these two subjects. Song et al. (2017) has investigated the vertical variability of hyporheic exchange in a confluent meander bend.

3.7 Hyporheic exchange numerical modelling

The fluid physics along and across the surface-subsurface water interface, at micro scale, has been of growing interest in the recent years (Cardenas and Wilson 2007a,b and of ease estimation with simplified assumptions. Field and laboratory data gave valuable insight into the sediment–water interface (SWI) role that was deeply examined by using numerical modelling Cardenas (2009a,b); Gomez-Velez and Harvey (2014) that can seek fundamental advancements when these empirical data are demonstrated or recreated through this method based on the conservation laws of mass, momentum, and energy. In this case a coupling physics system is needed: water surface physic can be simulated through Navier-Stokes and continuity equations for incompressible, viscous flow for the water column:

$$\rho \frac{\partial u}{\partial t} - \mu \nabla^2 u + \rho(u \cdot \nabla)u + \nabla p = 0 \quad (3.7.15)$$

$$\nabla \cdot u = 0 \quad (3.7.16)$$

where ρ is the fluid density, u the velocity vector, μ the dynamic viscosity, and p is the dynamic pressure. The porous bed domain is governed by the combination of Darcy's Law and the continuity equation for incompressible flow in a non-deformable media:

$$\nabla \cdot q = 0 \quad (3.7.17)$$

$$q = -\frac{k}{\mu} \nabla p \quad (3.7.18)$$

here q is the specific discharge (i.e. Darcy 'velocity') and k is intrinsic permeability. Simulations require boundary conditions between the two domains: the top of the water column is treated as a no-flow symmetry boundary and not as a free surface, while its bottom boundary, the SWI, assumes the no-slip/no-flow condition:

$$q = 0 \quad (3.7.19)$$

Because the top boundary of the porous domain is a prescribed pressure boundary, derived from solving the NS equations in the water column, the pressure is continuous across the two domains. Periodic boundaries are used on the left and right of both domains, adopting a periodic pressure and velocity boundary. This method allows to estimate residence time and fluxes path that, especially, in field setting are barely impossible to observe. For instance, two-dimensional models have been used to predicting hyporheic exchange across sand-bed channels with dune-like bedforms. Numerical simulations have indicated that the separation region and the related bottom pressures are a key parameter that control the flow field in the upper part of the porous medium and the size of the hyporheic zone Cardenas and Wilson (2007a,b).

These studies focused their aim on the investigation of the underlying and fundamental dynamics of advective exchange between rippled sediments and a water column driven by gravity waves. Several simulations were run varying

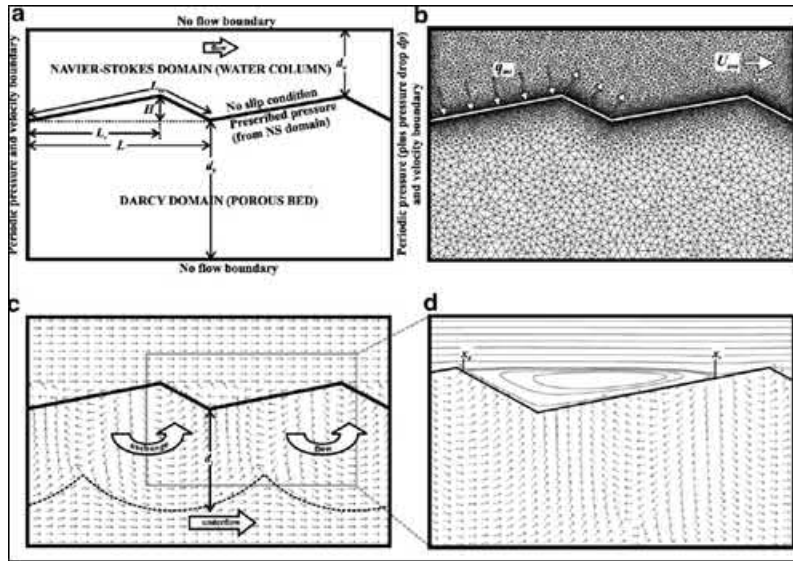


FIGURE 3.5: Figure from Cardenas and Wilson (2007a). (a) Schematic of model domain and system formulation, (b) representative finite element mesh, (c) typical solution for flow directions and (d) close up view of the eddy showing streamlines.

morphological parameters such as bedform length, bed crossover length, bedform height and the depth of impermeable boundary located at the bottom of the sediments. Results showed that the pressure gradient and the flow through the exchange volume were related to the Reynolds Number of the turbulent flow via a power function. However, a measure or prediction of pressure distribution along the streambed is needed to work properly as long as hydraulic conductivity of the sediment column, that in ideal case is hypothesised as homogeneous.

Revelli et al. (2008) examined an other aspect of hyporheic flow related to the longitudinal riverbed slope and the inclination of the stream free surface at the bends, instead, which induce pressure gradients along the riverbanks that drive the fluxes. In meandering rivers, where considerable pressure gradients develop along relatively short pathways between opposite banks of the same meander. In addition to that, morphodynamics evolution of meander rivers affects dynamics

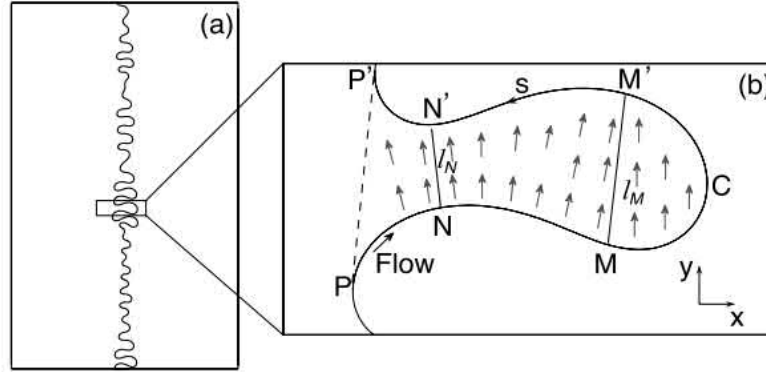


FIGURE 3.6: Figure from Revelli *et al.* (2008). (a) Shows an example of a river planimetry, whereas (b) presents the detail of a single meander.

of water exchange till through the meander cutoff. The equation describing the two-dimensional horizontal behavior of the piezometric head, $h(x, y)$, is given by the well-known Laplace equation, in this case:

$$\nabla^2 h^2 = 0 \quad (3.7.20)$$

while the velocity vector, V , in every point of the hyporheic zone, D , is obtained with the Darcy equation:

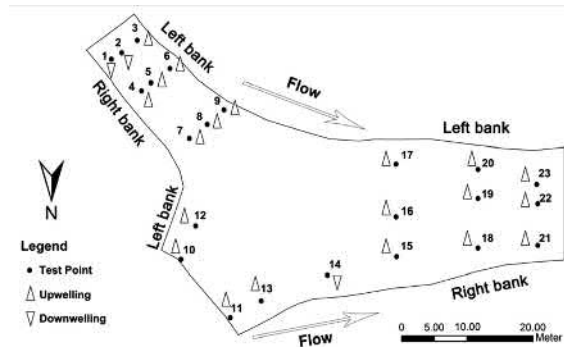
$$V = -\frac{K}{n} \cdot \nabla h \quad (3.7.21)$$

where K is the hydraulic conductivity and n is the porosity.

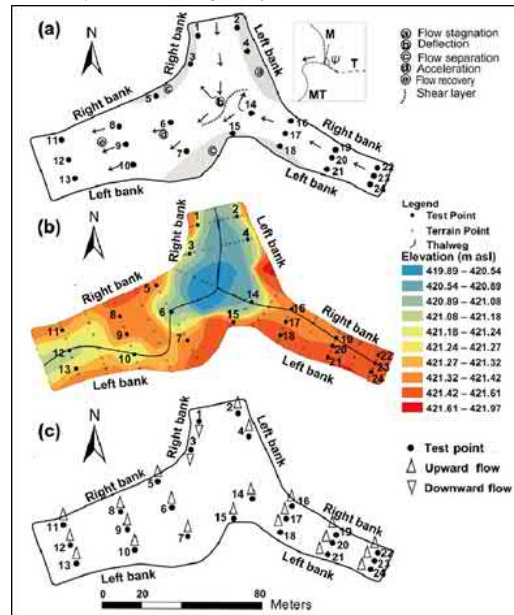
The outcomes of this research was that values of the residence times typical of the fastest and slowest hyporheic fluxes, were located in the meander neck and core, respectively. Moreover, meander hyporheic fluxes were depended on the knowledge of the river planimetry, the head differences and the mean hydraulic conductivity and porosity of the sediments.

3.8 Existing studies on hyporheic exchange at river confluences

Song et al. (2017) studied the general hydraulic and morphological characteristics of the confluent meander bend between the Juehe River and the Haohe River in the southern region of Xi'an City, Shaanxi Province, China. The estimation of the hyporheic flux was obtained after Stallman (1965) approach which uses a one-dimensional heat steady-state model to predict surface-subsurface water exchange. Under the complex conditions of the CMB morphology, significantly intricate spatial variability of sediment grain size distributions was found in different channel segments. In particular, hyporheic fluxes pattern were mostly affected by the erosional and depositional zones generated by planform geometry and flow momentum ratio. Grain size analysis were strongly related to hydraulic conductivity and, thus, helpful to understand the existence of fluxes pattern. Cheng et al. (2019) surveyed a river confluence in the same are as the previous study between the Juehe River and the Haohe River located in arid and semi-arid areas. The river confluence morphology effects on hyporheic water exchange were investigated in this study. The latter was controlled by the planform geometry with low river confluence flux momentum. Erosional zones generally occurred in the vicinity of the thalweg and the magnitude of hyporheic water exchange was significantly affected by the sediment particle distributions resulting from erosional and depositional processes. Temperature sensor were used to get vertical hydraulic fluxes (VHF) and spatial distribution. Plausible limitations of this study and previous one may cause by the short time testing since temperature profile were 30-minute long.



(A) Patterns of the hyporheic water exchange at each test point during July 11th and 12th, 2016



(B) Map of test points, indicating the patterns of vertical hyporheic water exchange at each test point during January 14 and 15, 2016

FIGURE 3.7: Hyporheic flux patterns at the Juehe River and the Haohe River confluence. Figures from Song et al. (2017) (down), Cheng et al. (2019) (up)

The objective of this work is based on the evidence of lack of long-term testing which may improve understanding of hyporheic water exchange processes and dynamics on river confluences along with comparison of different spatial and temporal scales. In fact, a one-dimensional model for temperature time series was adopted to figure out whether hyporheic exchange variation is dependent by CHZ and/or seasonal river stage and groundwater flow. In addition to that, a different method was also tested within one confluence to compare two distinct approaches (PVC piezometer readings).

TABLE 3.1: *Table comparison among previous studies on hyporheic fluxes at river confluences and purpose of this study.*

	Song et al. 2017	Cheng et al. 2019	Thesis
Land survey	x	x	x
Grain size analysis	x	x	x
Hydraulic Conductivity tests	x	/	x
Piezometer readings VHF	/	/	x
Temperature VHF	x	x	x
Temperature time series VHF	/	/	x

References

- Anibas, C., K. Buis, R. Verhoeven, P. Meire, and O. Batelaan
2011. A simple thermal mapping method for seasonal spatial patterns of groundwater-surface water interaction. *Journal of Hydrology*, 397(1):93 – 104.
- Anibas, C., J. H. Fleckenstein, N. Volze, K. Buis, R. Verhoeven, P. Meire, and O. Batelaan
2009. Transient or steady-state? using vertical temperature profiles to quantify groundwater-surface water exchange. *Hydrological Processes*, 23(15):2165–2177.
- Bredehoeft, J. D. and I. S. Papadopoulos
1965. Rates of vertical groundwater movement estimated from the earth's thermal profile. *Water Resources Research*, 1(2):325–328.
- Cardenas, B. M.
2009a. A model for lateral hyporheic flow based on valley slope and channel sinuosity. *Water Resources Research*, 45(1):n/a–n/a. W01501.
- Cardenas, B. M.
2009b. Stream-aquifer interactions and hyporheic exchange in gaining and losing sinuous streams. *Water Resources Research*, 45(6):n/a–n/a. W06429.
- Cardenas, B. M., J. L. Wilson, and V. A. Zlotnik
2004. Impact of heterogeneity, bed forms, and stream curvature on subchannel hyporheic exchange. *Water Resources Research*, 40(8).
- Cardenas, M. B. and J. Wilson
2007a. Hydrodynamics of coupled flow above and below a sediment-water interface with triangular bedforms. *Advances in Water Resources*, 30(3):301 – 313.

- Cardenas, M. B. and J. L. Wilson
2007b. Dunes, turbulent eddies, and interfacial exchange with permeable sediments. *Water Resources Research*, 43(8):n/a–n/a. W08412.
- Cheng, D., J. Song, W. Wang, and G. Zhang
2019. Influences of riverbed morphology on patterns and magnitudes of hyporheic water exchange within a natural river confluence. *Journal of Hydrology*, 574:75 – 84.
- Constantz, J., C. A. Eddy-Miller, J. D. Wheeler, and H. I. Essaid
2013. Streambed exchanges along tributary streams in humid watersheds. *Water Resources Research*, 49(4):2197–2204.
- Demaria, A., F. Boano, C. Camporeale, R. Revelli, and L. Ridolfi
2008. Flussi iporreici indotti dalla sinuosità dei fiumi meandriformi (in italian). In *31st National symposium on hydraulics and hydraulic structures, Perugia, Italy*.
- Elliott, A. H. and N. H. Brooks
1997. Transfer of nonsorbing solutes to a streambed with bed forms: Theory. *Water Resources Research*, 33(1):123–136.
- Endreny, T., L. Lautz, and D. I. Siegel
2011. Hyporheic flow path response to hydraulic jumps at river steps: Flume and hydrodynamic models. *Water Resources Research*, 47(2):n/a–n/a. W02517.
- Gariglio, F. P., D. Tonina, and C. H. Luce
2013. Spatiotemporal variability of hyporheic exchange through a pool-riffle-pool sequence. *Water Resources Research*, 49(11):7185–7204.
- Gomez-Velez, J. D. and J. W. Harvey
2014. A hydrogeomorphic river network model predicts where and why hyporheic exchange is important in large basins. *Geophysical Research Letters*, 41(18):6403–6412.
- Hatch, C. E., A. T. Fisher, J. S. Revenaugh, J. Constantz, and C. Ruehl
2006. Quantifying surface water-groundwater interactions using time series

- analysis of streambed thermal records: Method development. *Water Resources Research*, 42(10).
- Hyun, Y., H. Kim, S.-S. Lee, and K.-K. Lee
2011. Characterizing streambed water fluxes using temperature and head data on multiple spatial scales in munsan stream, south korea. *Journal of Hydrology*, 402(3):377 – 387.
- Janssen, F., M. B. Cardenas, A. H. Sawyer, T. Dammrich, J. Krietsch, and D. de Beer
2012. A comparative experimental and multiphysics computational fluid dynamics study of coupled surface-subsurface flow in bed forms. *Water Resources Research*, 48(8):n/a–n/a.
- Jiang, W., J. Song, J. Zhang, Y. Wang, N. Zhang, X. Zhang, Y. Long, J. Li, and X. Yang
2015. Spatial variability of streambed vertical hydraulic conductivity and its relation to distinctive stream morphologies in the beiluo river, shaanxi province, china. *Hydrogeology Journal*, 23(7):1617–1626.
- Keery, J., A. Binley, N. Crook, and J. W. N. Smith
2007. Temporal and spatial variability of groundwater-surface water fluxes: Development and application of an analytical method using temperature time series. *Journal of Hydrology*, 336:1–16.
- Marion, A., M. Bellinello, I. Guymer, and A. Packman
2002. Effect of bed form geometry on the penetration of nonreactive solutes into a streambed. *Water Resources Research*, 38(10):27–1–27–12.
- Packman, A. I. and K. E. Bencala
2000. *Streams and Ground Waters*, chapter Modeling Surface-Subsurface Hydrological Interactions. Academic Press.
- Revelli, R., F. Boano, C. Camporeale, and L. Ridolfi
2008. Intra-meander hyporheic flow in alluvial rivers. *Water Resources Research*, 44(12).

- Rhoads, B. L. and S. T. Kenworthy
1995. Flow structure at an asymmetrical stream confluence. *Geomorphology*, 11(4):273 – 293.
- Rhoads, B. L. and S. T. Kenworthy
1998. Time-averaged flow structure in the central region of a stream confluence. *Earth Surface Processes and Landforms*, 23(2):171–191.
- Ridolfi, L., F. Boano, and R. Revelli
2010. Flussi iporreici indotti da fluttuazioni turbolente di pressione (in italian). In *32nd National symposium on hydraulics and hyrdaulic structures, Palermo, Italy*.
- Song, J., G. Zhang, W. Wang, Q. Liu, W. Jiang, W. Guo, B. Tang, H. Bai, and X. Dou
2017. Variability in the vertical hyporheic water exchange affected by hydraulic conductivity and river morphology at a natural confluent meander bend. *Hydrological Processes*, 31(19):3407–3420. HYP-16-0947.R2.
- Stallman, R. W.
1960. Notes on the use of temperature data for computing groundwater velocity. In *Proceedings of 6th Assembly on Hydraulics. Société de hydrotechnique de France. Nancy, France*.
- Stallman, R. W.
1965. Steady one-dimensional fluid flow in a semi-infinite porous medium with sinusoidal surface temperature. *Journal of Geophysical Research*, 70(12):2821–2827.
- Stonedahl, S. H., J. W. Harvey, A. Wörman, M. Salehin, and A. I. Packman
2010. A multiscale model for integrating hyporheic exchange from ripples to meanders. *Water Resources Research*, 46(12).
- Tonina, D.
2008. *Fluid Mechanics of the Environmental Interfaces*, chapter Surface water and streambed sediment interaction: the hyporheic exchange, Pp. 1–44. Taylor & Francis.

Tonina, D. and J. M. Buffington

2007. Hyporheic exchange in gravel bed rivers with pool-riffle morphology: Laboratory experiments and three-dimensional modeling. *Water Resources Research*, 43(1).

Tonina, D. and J. M. Buffington

2009. Hyporheic exchange in mountain rivers i: Mechanics and environmental effects. *Geography Compass*, 3(3):1063–1086.

Triska, F. J., V. C. Kennedy, R. J. Avanzino, G. W. Zellweger, and K. E. Bencala

1989. Retention and transport of nutrients in a third-order stream in northwestern california: Hyporheic processes. *Ecology*, 70(6):1893–1905.

Chapter 4

Field surveys

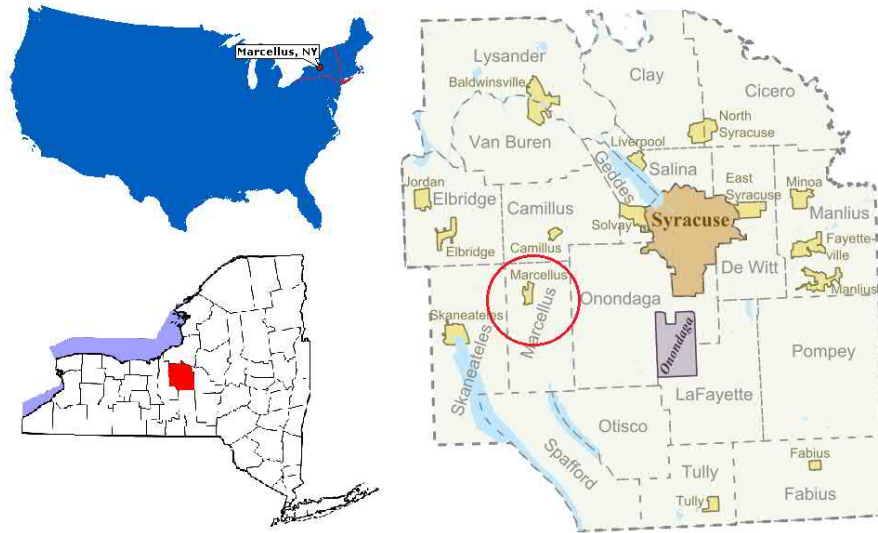
In this chapter, field studies are thoroughly presented showing monitored areas and confluences. Afterwards, a short background is given concerning field techniques mostly used and adopted within the study. Field experiments were carried out in Marcellus from September 2018 to December 2018 (FS-BBCB1 and FS-NCUC1) and from March to May 2019 (FS-BBCB2 and FS-NCUC2). Measurements were interrupted since this region has long and harsh winters from December 2018 up to March 2019. Set-up is finally showed illustrating spatial and temporal experiments scale in Methodology section.

4.1 Study site

First confluence was individuated between the Baltimore Brook and the Cold Brook (BB and CB, respectively), located in the Baltimore Woods Nature Center. The second case was a confluence formed by the Ninemile Creek and its tributary (NC and UC from now on, respectively) placed in southern Marcellus area. Due to their particular locations, discharge and precipitation were not available at the confluences.

4.1.1 Soils

The Onondaga County soil survey indicates that most soils in the study area are derived from till (83%); the rest are derived from glaciofluvial sediments such

FIGURE 4.1: *Study area overview*

as outwash, kames, and terraces (8.9%), postglacial lake sediments (2.6%), recent alluvial sediments (4.3%), and recent organic deposits (1.1%). Soil permeability ranges from less than 2 to more than 51 mm/h (Hutton and Rice, 1977).

Permeability of soils derived from till typically range from 5 to 15 mm/h but may be less where fragipans are present. Permeability of soils derived from well-sorted glacial outwash typically is greater than 51 mm/h , and that of soils derived from fine-grained lacustrine deposits or organic-rich soils is typically less than 2 mm/h . The Baltimore Woods soil area of study may be classified as outwash sand and gravel while in Ninemile Creek confluence's one mainly by alluvium. This soil characterization yields to moderate-well permeability which is shown in figure 4.2.

4.1.2 Climate

Climate in this area is characterized as humid continental and is moderated somewhat by the Great Lakes, especially Lake Ontario. The latter, with its moisture

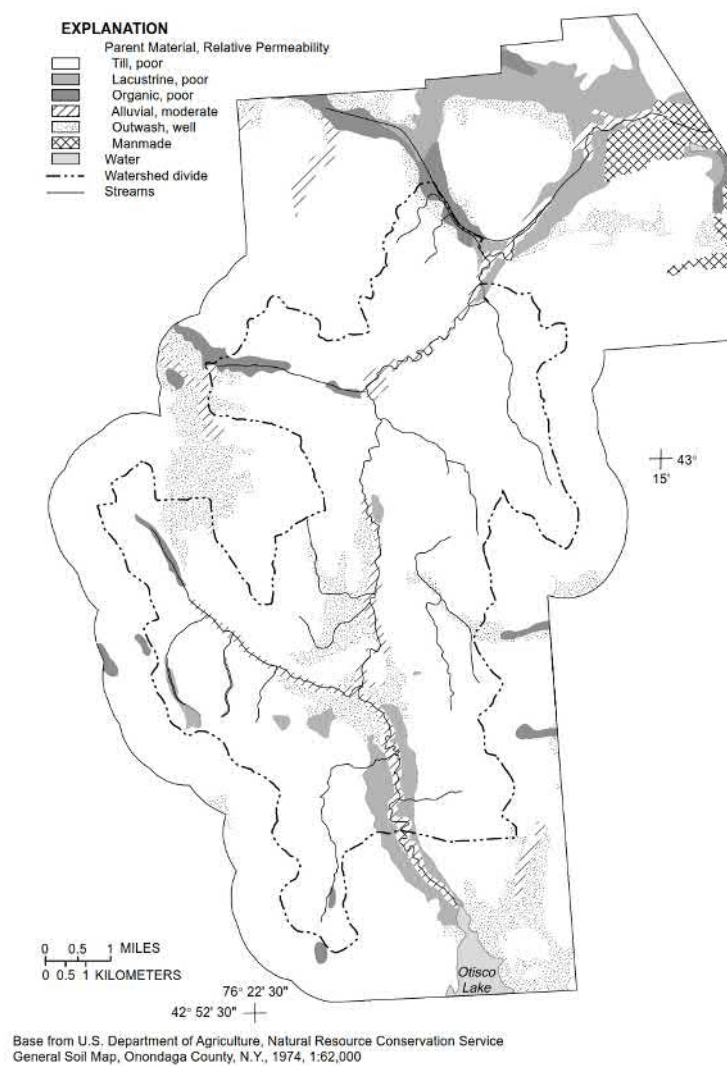


FIGURE 4.2: Soil characteristics of Marcellus town (source: USGS)

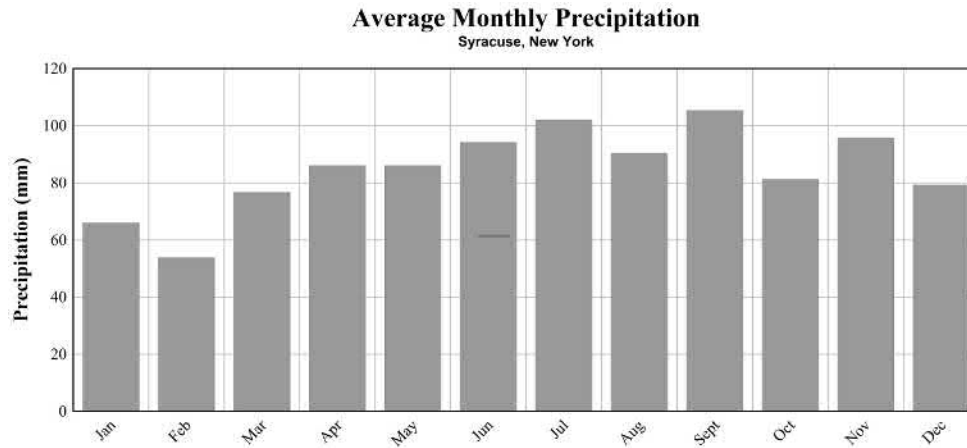


FIGURE 4.3: *Monthly normal precipitation (1981-2010) at Syracuse Hancock INTL AP (source: NOAA Online Weather Data)*

creates frequent cloudiness and “lake-effect” precipitation when relatively cool air passes over relatively warm lake waters. Precipitation from late October through late March can be in the form of local snow squalls that produce an average snowfall of 2768 *mm/yr*.

There was no metrological station in Marcellus and rainfall data were collected from the Syracuse Hancock National Airport weather station (National Oceanic and Atmospheric Administration), since its metro area confines with the Marcellus village. The 1055 *mm/yr* average precipitation reported is relatively evenly distributed throughout the year, although precipitation is slightly less in the winter, when moisture-holding capacity of the air is diminished. Surface evaporation is about 711 *mm/yr* and evapotranspiration, reported as the difference between annual runoff and precipitation, is about 508 *mm/yr*. Average annual runoff in this area is about 483 *mm*.

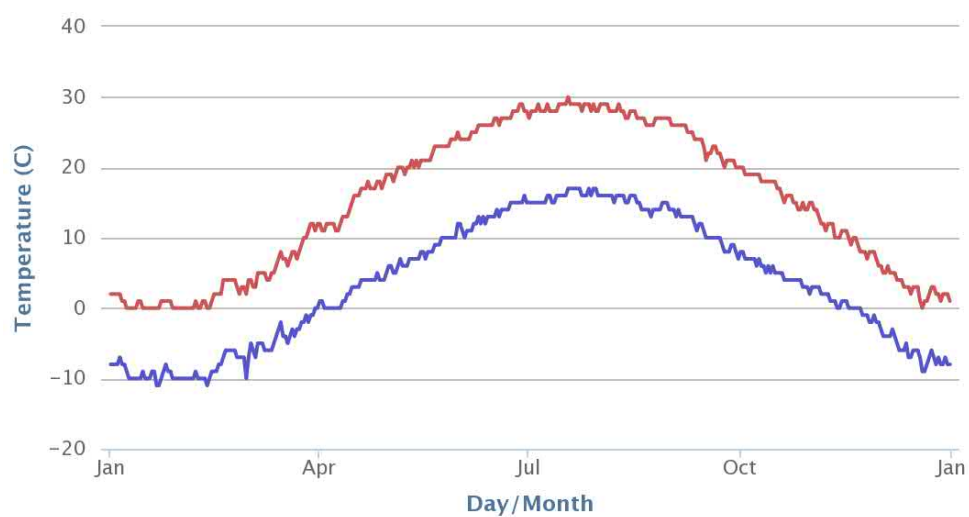


FIGURE 4.4: Max (Red line) and min (Blue line) temperature observations between October 1942 through to December 2012 at Syracuse Hancock International (source: NOAA Online Weather Data)

4.2 Baltimore Woods Nature Center (Marcellus, NY, USA)

Baltimore Woods Nature Center is located on 182 acres of land in Marcellus (NY, USA). This area includes fields, successional and mature forest, and many brooks and springs. The confluence was based on two brooks called Baltimore and Cold Brook flowing across the park ($42.966704^{\circ}\text{N}$, $-76.346998^{\circ}\text{W}$). The first is a tributary of Ninemile Creek long approximately 2.85 km with an bankfull streamflow of $0.53\text{ m}^3/\text{s}$. The other confluent, Cold Brook, has a length of about 1.5 km instead, confined within Baltimore Woods Nature Center park limits: its bankfull streamflow is $0.36\text{ m}^3/\text{s}$ (data from USGS StreamStats).

4.2.1 Site description

The drainage area of this first study case was about 1.73 km^2 with a mean annual assessed runoff for the considered basin is 462.28 mm . This confluence collects water from two small streams which flow from west to east forming a 45° confluence angle. The area was suitable for field measurements since it was easy to wade across (maximum depth during field experiments was about 50 cm , except for a relative high flow condition in December 2018). The Baltimore Brook, which is the main channel, flows with many sharp bends along the park. In fact, Baltimore Brook streambed has been eroded by streamflow causing a very steep bank on left-hand side of the confluence (looking from downstream to upstream) which represents the erosional bank whereas the Cold Brook bank has a more gently slope (depositional bank).

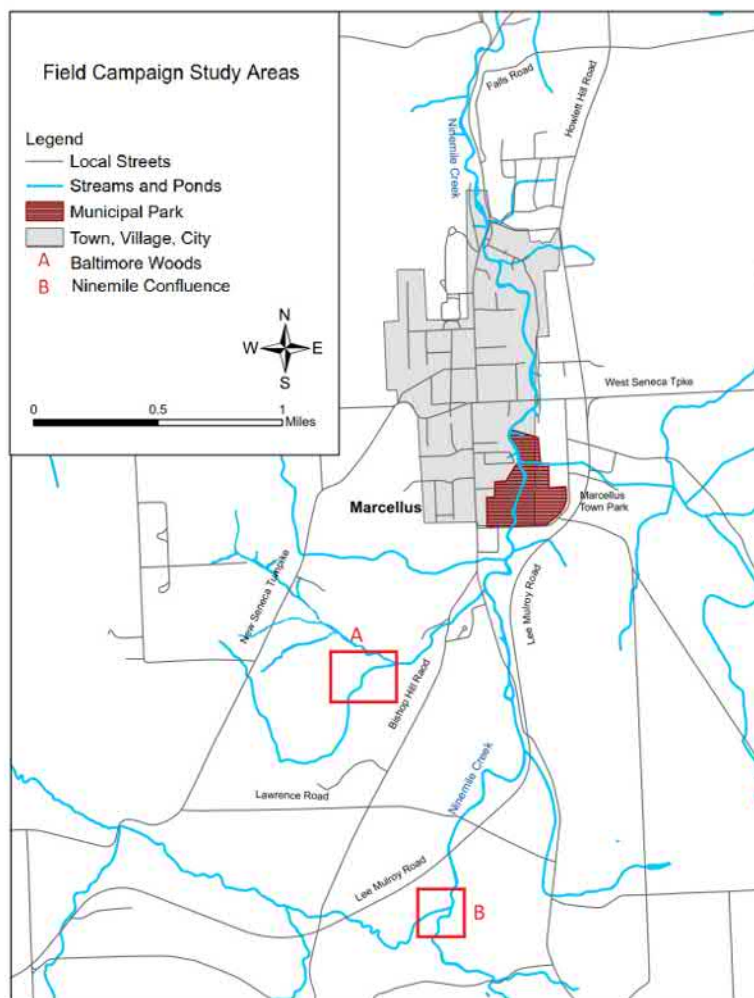


FIGURE 4.5: Marcellus study areas (red rectangles)



FIGURE 4.6: *Baltimore Woods Nature Center study site.*

The emerged area in between is composed of fine sand mostly and was surveyed with a couple of piezometer rows. Cold Brook was characterized by having more turbulent flow, especially in low flow condition, controlling mixing zone location which resulted shifted away from the streams junction. As a result of that, piezometers and temperature pipes were mostly inserted where the confluence zone was located. However, streambed topography influences pathways since the presence of a bed discordance between these streams and because of a pool individuated on Baltimore Brook, before approaching the junction, even blocked by some logs, which drastically reduces flux velocity, during mean flow condition.

4.3 Ninemile Creek (Marcellus, NY, USA)

Ninemile Creek is located in Onondaga County near the towns of Camillus and Marcellus, in Central New York. Its source is at Otisco Lake in the town of Marcellus, from where the creek runs northward for 35.00 *km* through the villages of Marcellus and Camillus to Onondaga Lake in the town of Geddes. Nine Mile Creek is a scenic stream noted for trout fishing. The study area ($42.953078^{\circ}\text{N}$, $-76.341514^{\circ}\text{W}$) was the junction of Ninemile and an untitled stream in southern

Marcellus area (southern Lee-Mulroy Road). This channel has a mean annual discharge of $5 \text{ m}^3/\text{s}$ (measured at Lakeland, NY just right before the Onondaga Lake) while there are no time series or historical observations concerning the untitled stream which converges into the confluence study case.

4.3.1 Site description

The drainage area was about 158.50 km^2 and the mean annual estimated runoff for the considered basin is 492.76 mm . There is a visible bed discordance between Ninemile Creek and its tributary which influences and generates a complex hydrodynamics. The main river has a predominance of sand over the bottom while an erosional area is well developed at Ninemile Creek's mouth: depending on bankful stage, pebbles and rocks are emerged or submerged during dry and wet seasons. This condition affects water circulation causing flow acceleration and shear layers formation. On the opposite site of the confluence, Ninemile Creek's tributary is characterized by permanent low-flow condition which causes deposition with a sandy-loamy river bottom. A stagnation zone is evident at confluence junction which is partially covered by dead vegetation.



(A) Field observations on 10/16/18



(B) Field observations on 12/02/18, in high-flow condition

FIGURE 4.7: Ninemile Creek confluence study site.

The riparian zone is mainly composed by woody vegetation with stretches of shrubs and herb mainly. The confluence was relatively safe to wade and to work on it, water depth was shallow at low stage (about 0.90-1.00 *m*) with ease of access thanks to a concrete bridge situated post-confluence. The latter constraints water flowing narrower, generating flow separation to its supports.

Discharge measurements were possible for instrument probe to record because of sufficient water depth. However, VHG measurements were limited to a narrow area close to the stagnation zone. In fact, streamflow shook piezometers over their usage, making piezometric head values not accurate and uncertain, causing continuous pressure variations inside each pipe. In addition to this, main channel mouth was characterized by impervious streambed where piezometers installation was barely achieved.

4.4 Methodology and scheduled field campaigns

Table 4.1 summarize methodology and period of data collection at Baltimore Woods Nature Center confluence (BWC) and Ninemile Creek confluence (NMC) confluences. Instrumentation utilized over FS-BBCB1, FS-BBCB2, FS-NCUC1 and FS-NCUC2 are listed below:

- Topcon GS-250
- Trimble GeoExplorer 2008
- Gravelometer (US SAH-97TM by Rickly Hydrological Co.)
- Rotap shaker
- Permeability test tube
- PVC piezometers
- Temperature rods equipped with temperature sensors (iButtons)

First stage was to obtain contour maps of confluences bedform which were achieved with a total station and a GPS receiver. Secondly, porous media and hydraulic characteristics were obtained. BWC field survey yielded soil samples, permeability in-situ tests, pressure head readings and temperature time series (Table 4.1). Data collection at NMC was slightly different: hydraulic conductivity tests and soil samples were undertaken in relatively shallow water because of field equipment configuration. In fact, pressure readings were unable to be taken due to its high median water depth. On the other hand, rivers discharge and depth-averaged were recorded in this analysis.

TABLE 4.1: *Resume of BWC and NMC field studies. LS stands for land survey, GSA for grain size analysis, K_v is the hydraulic conductivity, VHG the vertical hydraulic gradient, TTS the temperature time series.*

Field trip	LS	GSA	K_v	VHG	TTS
FS-BBCB1	Sept 18	Dec 18		Sept-Nov 18	Sept-Dec 18
FS-BBCB2			May 19		March-Apr 19
FS-NCUC1	Nov 18				
FS-NCUC2		May 19	May 19		Apr-May 19

4.4.1 Total station theodolite

A total station is an electronic/optical instrument used in surveying and building construction that uses electronic transit theodolite in conjunction with electronic distance meter (EDM). The instrument is used to measure sloping distance of object to the instrument, horizontal angles and vertical angles with the height of the instrument set to a common benchmark. This microprocessor unit enables for computation of data collected to further calculate the horizontal distance, coordinates of a point and reduced level of point. Data collected from total station can be downloaded into computer/laptops for further processing of information. A Topcon GTS-250 was deployed over field campaigns and Surfer 15 was performed for spatial analysis by using a natural neighbour as gridding method. Kennedy

et al. (2007) suggested a minimum points density of about $0.05 \text{ points}/m^2$ to reduce the occurrence of error value of 10 %. Therefore, bathymetrys were realized by quickly moving around a rod-stick equipped with a prism on the top (Fabian et al. 2011; Swanson and Cardenas 2012; Gariglio et al. 2013; Song et al. 2016). Furthermore, azimuth angles, piezometric head elevations and pipe temperature locations were obtained and referred from a known local datum (two benchmarks 4.4.2.1).

4.4.2 GPS System



FIGURE 4.8: *Topcon GTS-250*

that time. Even though GPS system uses a simple theory to work, collected data might be suffering uncertainty of meters (horizontally and vertically) caused by various factors such as:

- Tree canopy
- Hilly terrain
- Satellite constellation at collected data time
- Satellite geometry at the collected data time

The basic concept behind GPS is using satellites as reference points for triangulating a position somewhere on earth: every satellite yields a position on an imaginary sphere that is centred on itself and that has a radius equivalent to it. At least four satellites ranges to unambiguously locate any point. The basic idea of measuring a distance to a satellite is just velocity times travel-time: GPS system works by timing how long it takes a radio signal to reach a receiver from a satellite and then calculating the distance from

- Atmospheric condition (to a lesser extent)

Therefore, unknown points under or near a tall leaf on tree canopy (or thick tall conifers) may have difficulty in being achieved with optimal precision. Likewise in a valley area, where the signal from the satellite actually reflects off hills near the antenna or even large diameter tree trunks for that matter (multi-pathing), the distance the signal travels would be longer and cause inaccuracies in the data.

The number and geometry of the satellite constellation during acquisition also plays a large part in data precision. Optimal constellation configurations for the surveyed area may not occur at times when a survey would normally be done. The goal is to do a work at a time when the most satellites are available and they are in the best position.

4.4.2.1 Trimble GeoExplorer 2008

This handheld device, Trimble GPS receiver with a field computer powered by Microsoft Windows Mobile operating system, was deployed over field campaigns to get accurate benchmarks of surveyed confluences. Attached to it there was an external antenna for improved yield under canopy and for a better accuracy, a Satellite Based Augmentation Systems (SBAS) correction messages was used to improve precision and integrity of GPS data.

The receiver tracked or locked onto the most powerful satellite signal. The GPS receiver could track two SBAS satellites at the same time and used corrections from only one SBAS satellite at a time, but tracking two satellites could improve the availability of SBAS real-time corrections. Since points elevation was pretty much sensitive to signal accuracy, precision increased up to less than 30 *cm*.

4.4.3 Confluence bed sediment analysis

Porous media features were obtained through two different methods: pebble count and grain size analysis. At Baltimore Woods Nature Canter, shallow water depth allowed to collect streambed pebbles using the Wolman Pebble Count procedure. It was done in each tributary (Baltimore Brook and Cold Brook) and in the confluence zone. Bed material was sized using a gravelometer (US SAH-97TM by Rickly

Hydrological Co.) which has 14 square holes of common sieve sizes (1/2-phi unit classes) ranging from 2 to 180 mm. There is also a scale along one side that can be used to measure up to 310 mm. The scale is in 10-mm increments.

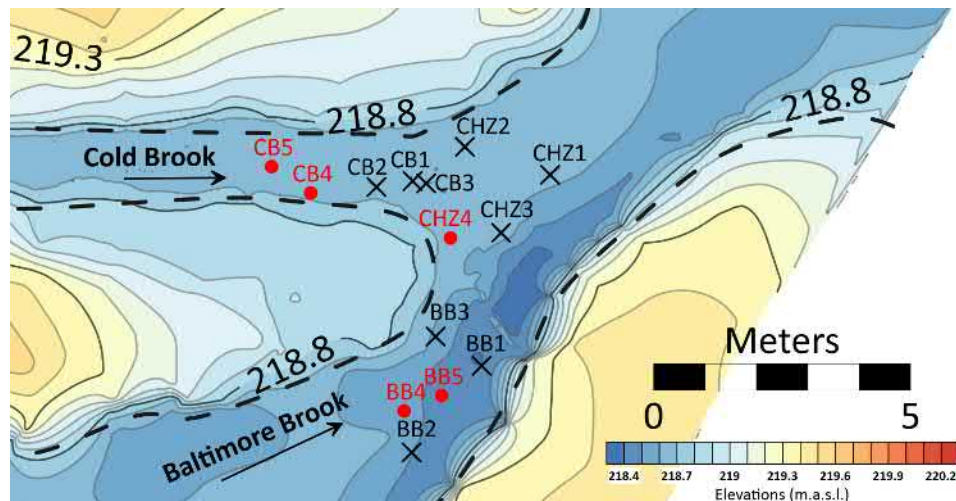


FIGURE 4.9: Black crosses represent K_v test point locations (05/06/19) while red crosses are soil sample collection points.

Analysis consisted in determining which hole the pebble fits through in the instrument and record to a field book. In general, a reach is selected for sediment particle size distribution and sample of 100 measurements at least is required. This procedure was discarded for Ninemile Creek confluence due to its topography and water depth.

The second approach was done at Department of Forest and Natural Resources Management at SUNY-ESF by collecting soil samples of Baltimore Woods Nature Center and Ninemile Creek confluences which were analysed by a sieving method to get grain size curves. Each sediment sample was dried and poured into a rotap sieve shaker for shaking and then categorized. Sieves used for this analysis were: #10, #18, #35, #60, #140 and #270.

4.4.4 Hydraulic conductivity test pipe

The hydraulic conductivity of a streambed is an important parameter affecting surface and subsurface water exchange between streams and surrounding groundwater.

It also plays a significant role to better estimate other hydro-geochemical problems (Song et al. 2010; Jiang et al. 2015; Song et al. 2016, 2017). In field methodology was carried out following a very practical approach described by Chen (2000) which is a simplified version of the permeameter method Hvorslev (1951).

The method measures K_v of the sediment column, which can be calculated as follows:

$$K_v = \frac{L_v}{(t_2 - t_1)} \cdot \ln \frac{h_1}{h_2} \quad (4.4.1)$$

where K_v vertical hydraulic conductivity of the streambed, L_v thickness of the measured streambed in the pipe, h_1 the hydraulic head in the pipe measured at time t_1 , and h_2 the hydraulic head in the pipe measured at time t_2 . Water level is assumed to be constant during test. Calculation was done using, as pair of head readings, the head measured at t_1 , h_1 , and successively decreasing readings $h_2(t_2)$, $h_3(t_3)$, $h_4(t_4)$, to estimate K_v (Table 5.5). That area was subjected to fine sand deposition that might be carried downward altering K_v results. Tests were conducted in winter with lower water kinematic viscosity which may affect permeameters.

Therefore, the test pipe was made by a transparent plastic tube signed each centimetre. It was after lowered into significant spots of the study areas with the same approach as before mentioned (4.4.5). Readings were collected pouring water inside the pipe and taking note of successive negative piezometric heads.



FIGURE 4.10: Pipe used for K_v tests.

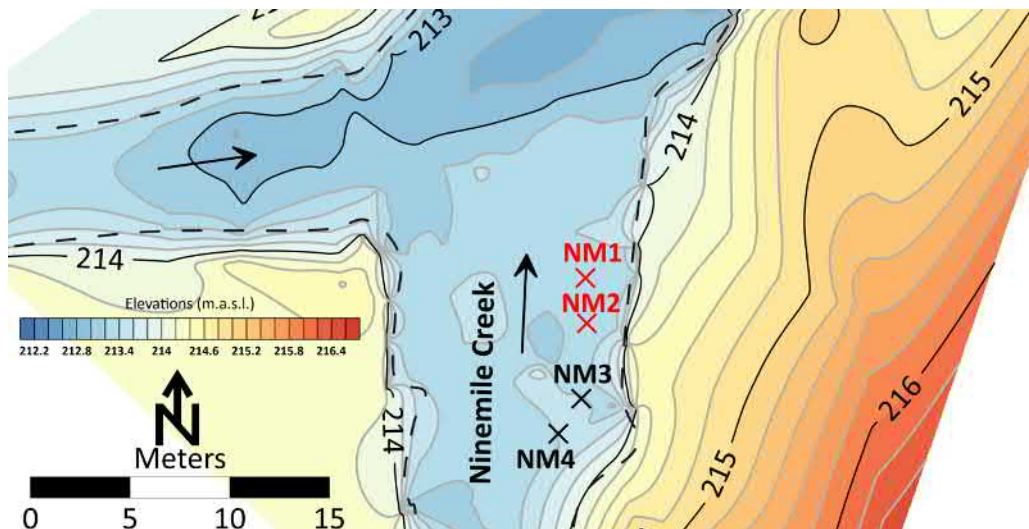


FIGURE 4.11: Red crosses represent soil sample collection points and black crosses Kv test point locations at NMC.

4.4.5 Piezometers

A piezometer is a well designed to get liquid pressure by reading its water column from a specific point where a screening or an opening is located. It measures, for instance, the piezometric head of groundwater or static pressure of a river water. Observations must be obtained manually as long as a transducer is installed inside itself. Deploying procedure consisted firstly in inserting a metal driver inside each mini-well before hammering into soil. Secondly, with the help of a sledge hammer, every piezometer was pushed to a depth ranging between 25-35 *cm* (Kennedy et al. 2007; Fabian et al. 2011; Song et al. 2016) and finally removed the inserter device. In this study 24 mini-wells (15 *mm* inner diameter) were used to calculate VHG (3.6) and piezometric head of streams and confluence area. They ranged from 1 to 1.2 *m* in height and from 10 to 15 *cm* in screening. Piezometric head measurements were conducted following a previous work approach (Fabian et al. 2011; Kennedy et al. 2007) which consisted in determining water level blowing air into a plastic tube lowered inside piezometers: sound of bubbles identified tube

position in contact with water level. Therefore, direct measurements were taken from each in-stream piezometer and used to compute VHGs and Darcy's fluxes over the all in-situ study (Song et al. 2016, 2017).

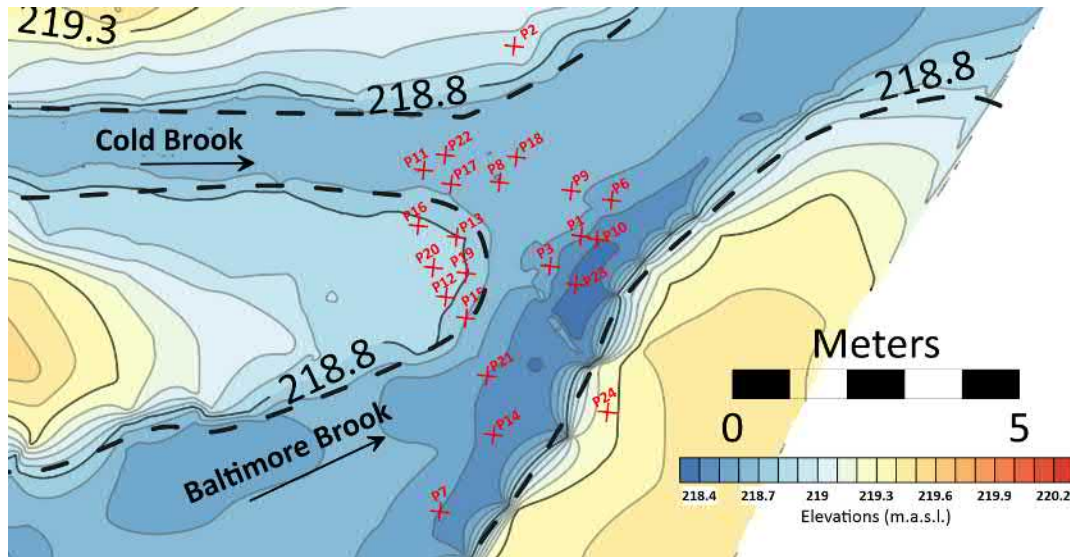


FIGURE 4.12: Piezometers map at Baltimore Woods Nature Center confluence.

Baltimore Woods Nature Center study site was surveyed with mini-wells (including 2 on confluence banks and 5 within the emerged area between Baltimore Brook and Cold Brook) and instantaneous measurements were collected in August, September and November 2018.

4.4.6 Temperature rods

Water temperature profile data collection was made it possible thanks to multiple PVC pipes (interior diameter 20 mm and 100 cm approximately long). They were drilled with distances from the tip at 5, 10, 15, 25 and 45 cm. Inside these PVC rods, wooden stakes were inserted and slotted at the same gaps as the pipes, for temperature sensors to fit inside (iButtons 4.4.6.1). To secure them, they were

sealed with a silicone glue, which has successfully been used in previous work Lautz et al. (2010), and let it dry for 24 hours. Every pipe was driven into the soil in order to have sensors at surface-subsurface interface, 20 *cm* and 40 *cm* from streambed and at surface-subsurface interface, 5 *cm* and 10 *cm* from streambed, during 2018 and 2019 field campaign respectively. To help installation on field, a metal inserter dug the way in before hammering the instruments.

4.4.6.1 iButton Devices

The iButton device is a computer chip enclosed in a 16 *mm* thick stainless steel can. The device uses its stainless steel 'can' as an electronic communications interface. Each can has a data contact, called the 'lid', and a ground contact, called the 'base'. Each of these contacts is connected to the silicon chip inside. The specific type used within this research was the DS1922L: each sensor has an accuracy of $\pm 0.5\text{ }^{\circ}\text{C}$ (from $-10\text{ }^{\circ}\text{C}$ to $+65\text{ }^{\circ}\text{C}$) and programmable resolution of $0.5\text{ }^{\circ}\text{C}$ for 8 bit and $0.0625\text{ }^{\circ}\text{C}$ for 11 bit. The 8 bit can read up to 8192 values at a logging rate of 1 second to 273 hours, and the 11 bit can read up to 4096 values at the same logging rate. If it is compared with others temperature sensors available in commerce (Rau et al. 2010; Swanson and Cardenas 2012; Anibas et al. 2011; Hyun et al. 2011), one of the strongest point is definitely its small dimension and independent function. In addition to this, iButton software allows to set sampling rate, sensor accuracy, starting delay and temperature alarms. Data were eventually post-processed and downloaded into a computer analysing temperature time series: sampling rate varied from 1 *min* to 10 *min*. Subsurface-surface confluence interface was monitored over 2018 and 2019 field campaigns. Time series, at BWC, were obtained in September (7 days), October-November (14 days) and December 2018 (2.5 days) and in March-April 2019 (13 days) (Figure 4.14a 4.14b). At NMC, data were collected in April-May 2019 (34 days) (Figure 4.15). Data analysis were conducted by using a MATLAB code which is described in the following subsection.

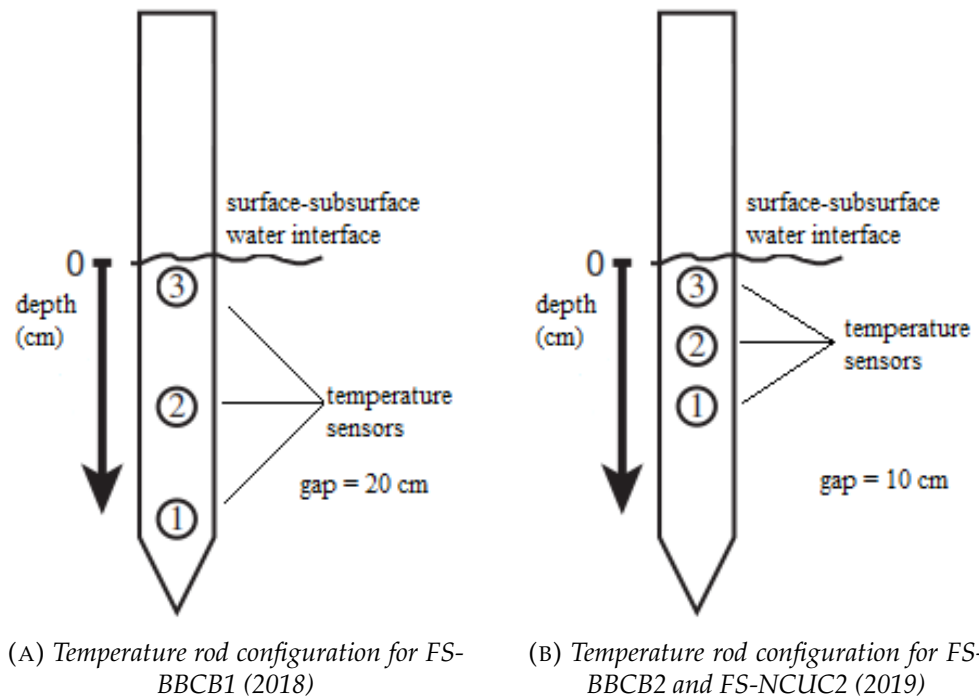
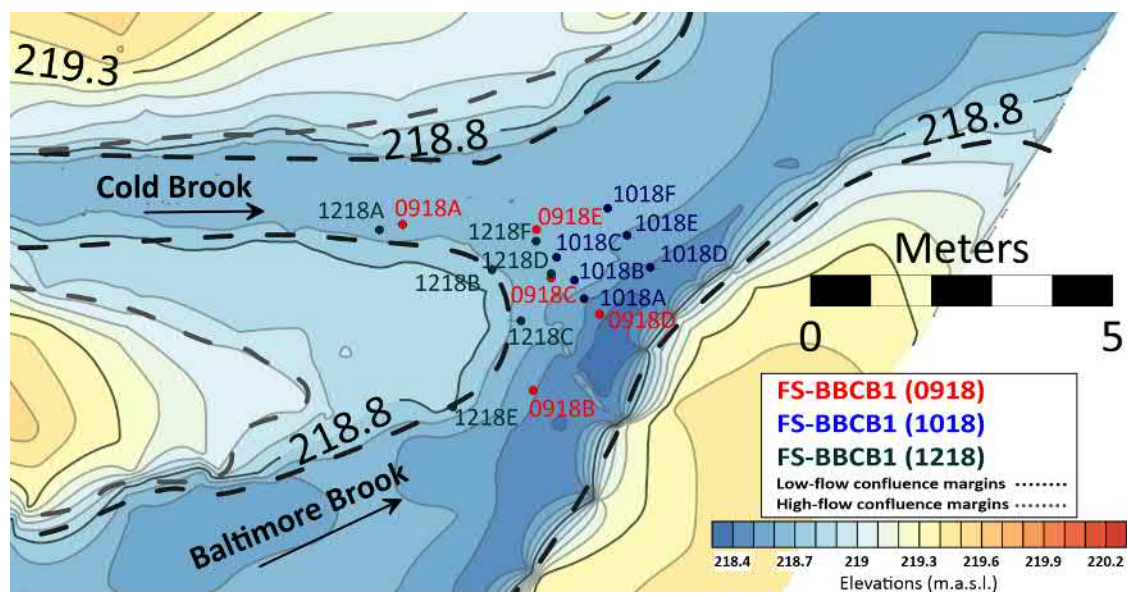
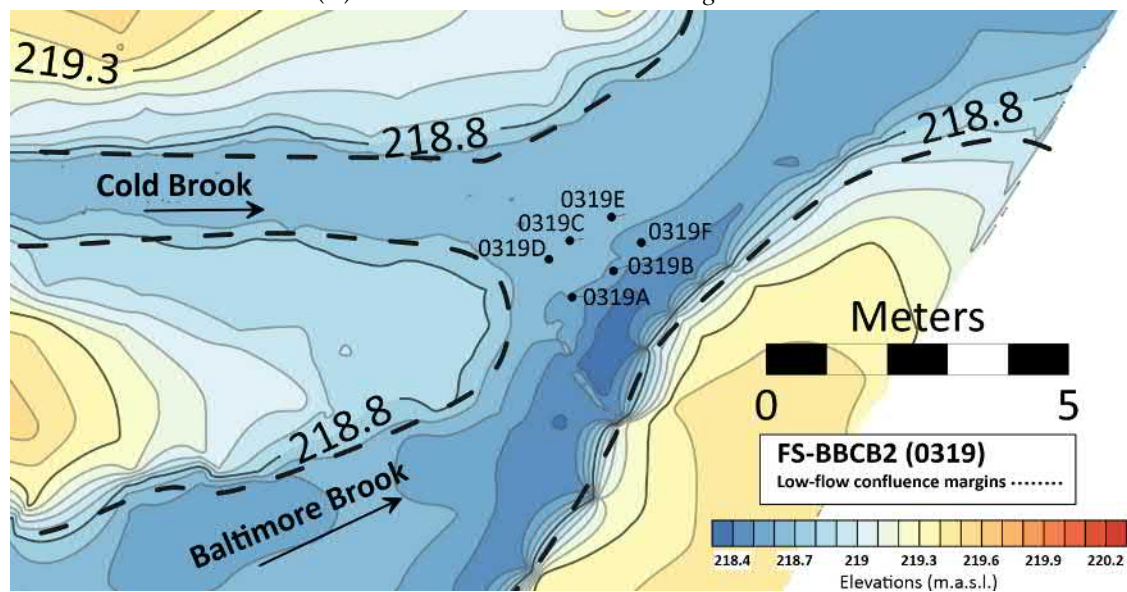


FIGURE 4.13: Surface-subsurface water temperature collection setup



(A) iButtons location at BWC during FS-BBCB1.



(B) iButtons location at BWC during FS-BBCB2.

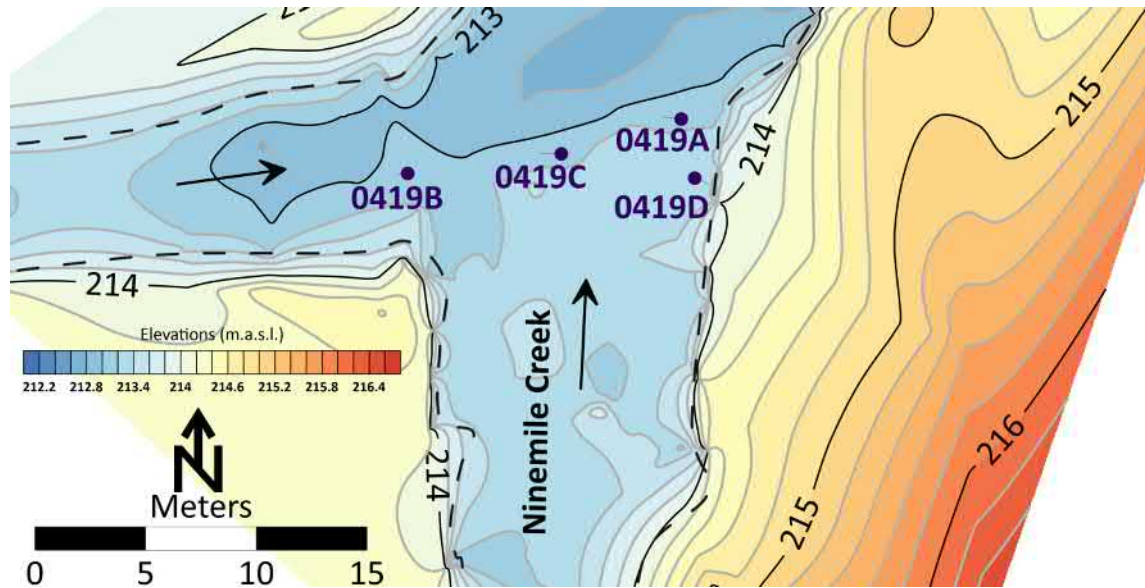


FIGURE 4.15: *iButtons* location at NMC during FS-NCUC2.

4.4.7 Flow meters

Collecting flow data is essential for characterizing and simulating every study area. The principle is measuring volumetric or mass flow rates, such as litres per second or kilograms per second, respectively. They may be mechanical, pressure-based, thermal mass, Sonar or open-channel flow meters. The latter was used within this application and it is basically a matter of localize a channel cross-section, calculating its cross-sectional area (determined by the shape of the channel and depending on water depth), dividing it in equal spaced columns.

According to the geometry of the channel, each column consists of a triangle and/or a rectangle and the area of each column was calculated by using simply water depth and column width. Finally a grid is obtained where in each "cell" midpoint the average velocity is required to get river discharge.



FIGURE 4.16: MFP51 Stream Flow meter components (left) and deployment (right)

4.4.7.1 MFP51 Stream Flow meter

This instrument consists of an impeller and a coupled sensor which counts numbers of revolutions by opening and closing a switch. It is equipped with multiple riser rods which together make a 1 m stick (every section is 25 cm long). The total number of counts per minute is converted into a velocity value by an experimental formula obtained from a calibration chart and its formula:

$$V(m/s) = (0.000845C_{fm}) + 0.05 \quad (4.4.2)$$

where C_{fm} is the number per minute. The latter may be read on a LCD counter connected to a jack plug from the impeller. To obtain flow discharge, the method requires a perpendicular cross-section divided into equal spaces.

4.4.7.2 Sontek/YSI Flow Tracker Handheld ADV

The ADV technology has been used widely to provide velocity measurements at a single point to compute river discharge or shear flow. It determines velocities by a change in acoustic frequency emitted by a transmitter and converted to an instantaneous velocity value from two or three receivers. This variation is due to reflections, suspended sediment or moving particles which are assumed to be moving at the same velocity as the water.

In particular, the FlowTracker is provided with a computer which is protected by a water resistant case linked to the probe by a rubberized data cable. Its functions are carried out thanks to a keypad and a LCD screen. The probe contains 3 ceramic receiving transducer and a central transmitting transducer which generates a sample volume (less than 0.5 cm^3) and located 10-12 *cm* away from the face of it.

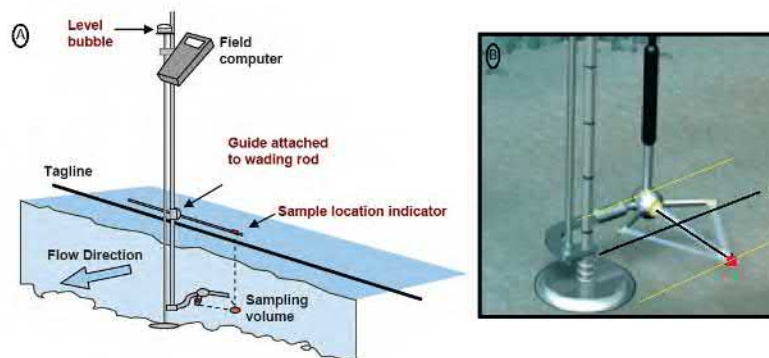


FIGURE 4.17: (a) *Instrument set-up explained*; (b) *Sontek Flow Tracker Handheld adv probe*

The receivers sample this reflected sound at the exact time corresponding to the return from the sample volume (based on speed of sound in water) and measure the change in frequency (Doppler shift) between the transmitted and received signals.

The FlowTracker is usually deployed with a conventional hydrometric field equipment such as the wading rod: SonTek wading rod attachment bracket (supplied by the manufacturer). This bracket offsets the sensor face to the left of the rod. The resulting sampling volume is 5-9 *cm* to the right of the wading rod centerline.

4.5 Post-processing data

Thermal records were collected over several days across BWC and NMC sites. Thousands of temperature data needed to be reduced and daily-averaged to ensure that signal noise did not affect vertical fluxes estimation. In this section a brief resume is showed concerning sensors data post-processing method.

4.5.1 Temperature data code analysis: VFLUX2

Thermal records went through the VFLUX 2 program to calculate vertical flux rates. VFLUX2 is distributed as an open source MATLAB toolbox, a set of functions written in the MATLAB computing language that are designed to run in the MATLAB environment. The program is exhaustively described in Gordon et al. (2011) as VFLUX, first version of the program, and Irvine et al. (2015), further functions implemented, where version 2.0 is illustrated. VFLUX2 operates following six major steps:

- format all sensors time series to a one-dimensional vector with same time step;
- applies a low-pass filter and extract a 12 samples per fundamental cycle (day);
- isolate the fundamental signal (typically diurnal) using DHR;
- obtains amplitude and phase shifts for the fundamental signal using DHR;
- individuates pairs of sensors where fluxes have to be computed;

- calculate vertical water flux rates between the identified sensor pairs.

First of all, every set of data were resampled to the "lowest common denominator". That means that trims the input series to the shortest time range that is common to all the input series, and interpolates/resamples the input series to have the lowest sampling rate of all the input series Gordon et al. (2011).

Secondly, time series were reduced to 12 samples per fundamental cycle is an operation that reduces noise and improves Dynamic Harmonic Regression (DHR) model Young et al. (2010) efficiency in the filtering process Gordon et al. (2011). The latter produces a time-varying apparent amplitude and phase coefficients for a time series, extracting harmonic signals from dynamic environmental systems. Since streambed temperature fluctuates over time due to weather and seasonality, fluxes have varying temporal scales: a non-stationary approach for diurnal signal is mandatory. Therefore, the harmonic components of the original temperature data are desired. Thus, VFLUX2 attempts to identify a trend, the fundamental signal (ω_1), and the first and second harmonics (ω_2 and ω_3) using an auto-regression (AR) frequency spectrum created with the Captain Toolbox.

TABLE 4.2: *Input parameters of VFLUX2 code for computing hyporheic flux, where β is dispersivity, K_{Cal} the thermal conductivity, Cs_{Cal} volumetric heat capacity of the sediment, and Cw_{Cal} the volumetric heat capacity of the water.*

Parameter	Value	Unit
β	0.001	m
K_{Cal}	0.0045	$cal / (s \cdot cm \cdot C)$
Cs_{Cal}	0.5	$cal / (cm^3 \cdot C)$
Cw_{Cal}	1.0	$cal / (cm^3 \cdot C)$

Results are then plotted showing the time series in the frequency domain. If the time series contains the fundamental signal at sufficient power, there should appear peaks near the fundamental period (12 samples/cycle in this case) and one or more of its harmonics. If the DHR model fits the AR spectrum, a modelled

red line might be visible, on a plotted graph, over the fundamental peak and any other selected harmonics.

Next stage provides that flux estimations are computed between pairs of sensors selected. By setting the desired sensor-spacing "window", in units of sensor-spacings, sensor pairs for flux calculations are identified. In this way, VFLUX2 will calculate flux between all the sensor pairs that are separated by the "window"-number of sensor-spacings. In our case the "window" was set as 1: fluxes were estimated between sensor 1 and 2, 2 and 3.

Methods for calculating vertical fluxes are: Hatch amplitude and phase method, Keery amplitude and phase method, McCallum and Luce. All those approaches are analytical solutions to 1-D heat transport equation 3.6.6.

References

- Anibas, C., K. Buis, R. Verhoeven, P. Meire, and O. Batelaan
2011. A simple thermal mapping method for seasonal spatial patterns of groundwater-surface water interaction. *Journal of Hydrology*, 397(1):93 – 104.
- Chen, X.
2000. Measurement of streambed hydraulic conductivity and its anisotropy. *Environmental Geology*, 39(12).
- Fabian, M. W., T. A. Endreny, A. Bottacin-Busolin, and L. K. Lautz
2011. Seasonal variation in cascade-driven hyporheic exchange, northern Honduras. *Hydrological Processes*, 25(10):1630–1646.
- Gariglio, F. P., D. Tonina, and C. H. Luce
2013. Spatiotemporal variability of hyporheic exchange through a pool-riffle-pool sequence. *Water Resources Research*, 49(11):7185–7204.
- Gordon, R. P., L. K. Lautz, M. A. Briggs, and J. M. McKenzie
2011. Automated calculation of vertical pore-water flux from field temperature time series using the vflux method and computer program. *Journal of Hydrology*, 141-142:142–158.
- Hvorslev, M. J.
1951. Time lag and soil permeability in ground-water observations. Technical report, US Army Bull 36, Waterways Experiment Station, US Army Corps of Engineers, Vicksburg, Mississippi.
- Hyun, Y., H. Kim, S.-S. Lee, and K.-K. Lee
2011. Characterizing streambed water fluxes using temperature and head data

- on multiple spatial scales in munsan stream, south korea. *Journal of Hydrology*, 402(3):377 – 387.
- Irvine, D. J., L. K. Lautz, M. A. Briggs, R. P. Gordon, and J. M. McKenzie
2015. Experimental evaluation of the applicability of phase, amplitude, and combined methods to determine water flux and thermal diffusivity from temperature time series using vflux 2. *Journal of Hydrology*, 531:728–737.
- Jiang, W., J. Song, J. Zhang, Y. Wang, N. Zhang, X. Zhang, Y. Long, J. Li, and X. Yang
2015. Spatial variability of streambed vertical hydraulic conductivity and its relation to distinctive stream morphologies in the beiluo river, shaanxi province, china. *Hydrogeology Journal*, 23(7):1617–1626.
- Kennedy, C. D., D. P. Genereux, D. R. Corbett, and H. Mitsova
2007. Design of a light-oil piezomanometer for measurement of hydraulic head differences and collection of groundwater samples. *Water Resources Research*, 43.
- Lautz, L. K., N. T. Kranes, and D. I. Siegel
2010. Heat tracing of heterogeneous hyporheic exchange adjacent to in-stream geomorphic features. *Hydrological Processes*, 24:3074–3086.
- Rau, G. C., M. S. Andersen, A. M. McCallum, and R. I. Acworth
2010. Analytical methods that use natural heat as a tracer to quantify surface water–groundwater exchange, evaluated using field temperature records. *Hydrogeology Journal*, 18(5):1093–1110.
- Song, J., X. Chen, C. Cheng, D. Wang, and W. Wang
2010. Variability of streambed vertical hydraulic conductivity with depth along the elkhorn river, nebraska, usa. *Chinese Science Bulletin*, 55(10):992–999.
- Song, J., W. Jiang, S. Xu, G. Zhang, L. Wang, M. Wen, B. Zhang, Y. Wang, and Y. Long
2016. Heterogeneity of hydraulic conductivity and darcian flux in the submerged streambed and adjacent exposed stream bank of the beiluo river, north-west china. *Hydrogeology Journal*, 24(8):2049–2062.

- Song, J., G. Zhang, W. Wang, Q. Liu, W. Jiang, W. Guo, B. Tang, H. Bai, and X. Dou
2017. Variability in the vertical hyporheic water exchange affected by hydraulic conductivity and river morphology at a natural confluent meander bend. *Hydrological Processes*, 31(19):3407–3420. HYP-16-0947.R2.
- Swanson, T. E. and B. M. Cardenas
2012. Diel heat transport within the hyporheic zone of a pool-riffle-pool sequence of a losing stream and evaluation of models for fluid flux estimation using heat. *limnology and oceanography*, 55(4):1741–1754.
- Young, P., C. Taylor, W. Tych, D. Pegregal, and P. McKenna
2010. The captain toolbox.

Part II

Chapter 5

Data results

In the following section field experiment results are illustrated. Total station data were processed into bathymetry maps and georeferenced through GPS benchmark data. Pressure head readings collected from piezometers at BWC yielded VHGs (those placed into the water), groundwater levels (located on river banks) and transversal head gradients from some installed on a strip of land between BB and CB. Soil samples went through a grain size analysis and three samples of pebbles were used to discriminate BB and CB river beds. Readings from the hydraulic conductivity test pipe provided values of K_v applying the Chen (2000) method and temperature time series processed through Gordon et al. (2011) MatLab code.

5.1 Plan form geometry

A total station Topcon GTS-250 was deployed for this study (subsection 4.4.1) and Surfer 15 was performed for spatial interpolation by using a natural neighbor as gridding method. In this study, points density of streambed was $0.90/m^2$ and $0.135/m^2$ for Baltimore Nature Woods Center and Ninemile Creek confluence, respectively.

5.1.1 BWC site

BB and CB were two first-order streams where water level was predominantly shallow over this field study, constituted by low-gradient velocities and pressure

variations. The planform geometry was Y-shaped with a junction angle of approximately 45° . The confluence was characterized by low-gradient water surface slopes, with slightly higher slopes in the CB tributary in the 5 meters above the junction. The strip of land connecting BB and CB at the junction was rich in outwash sediments and partially submerged during high-flow discharge events (i.e. in December after a sudden snow melt, which complicated the drawing and localization of the BB and CB riverbanks (see down in Figure 5.1).

5.1.2 NMC site

This confluence zone is characterized by a 90° junction angle: three-dimensional flow dynamics and water depth have tremendously influenced confluence bed which is strongly discordant. In fact, various boulders and pebbles might be seen just right before a deep sediment face formed on Ninemile Creek side while its tributary streambed is predominantly sandy, instead. This morphological configuration suggests an intensive erosional activity and momentum flow ratio dependence, with an evident mid-channel scour hole of approximately 20 m length (Figure 5.2).

5.2 Hydrodynamics observation

5.2.1 BWC site

The confluence flow was dominated by low-flow and base-flow conditions, and field observations were taken during one high-flow event in December 2018 (FS-BBCB1), during liquid precipitation and snowmelt, and in March 2019 (FS-BBCB2). The hydraulic characteristics of BWC, such as water levels and discharge, were not daily monitored due to a lack of water-stage recorders within the watershed. Visual observations yielded larger velocity from CB because of its bed morphology and steep riffle slope into the confluence. The location of the shear layer moved towards the right bank or BB side of the confluence due to the dominant CB flow velocity (see the dotted blur line in Figure 5.3). Downward fluxes from prior channel forming flows eroded the BB riverbed forming a large scour hole

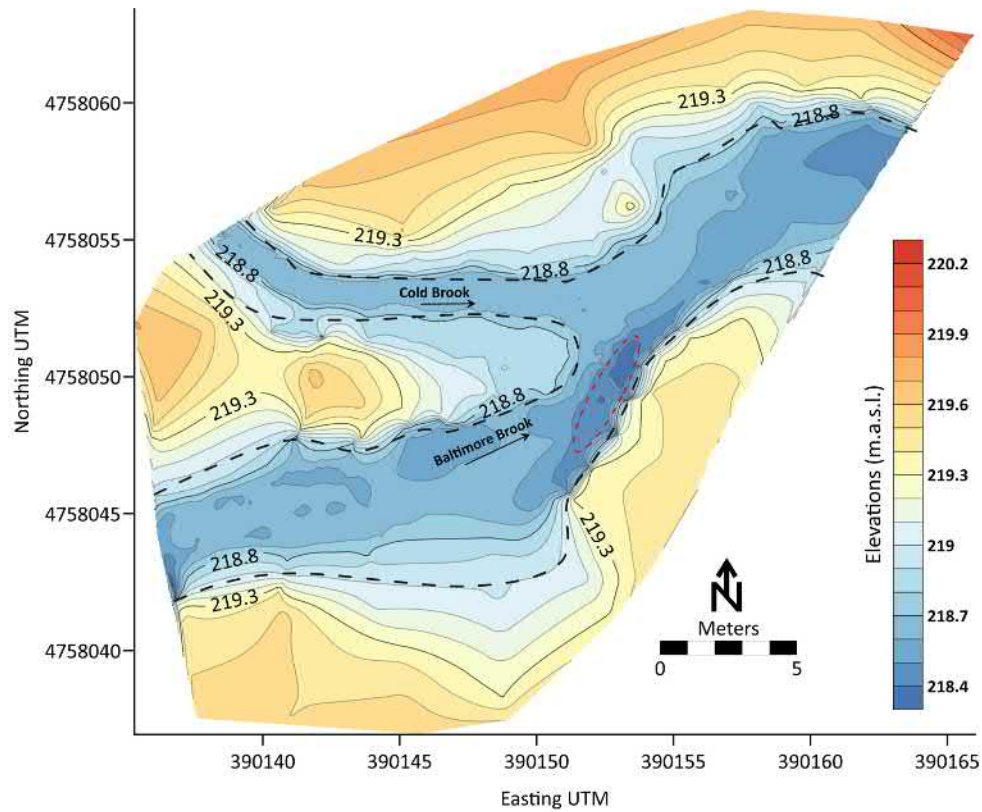


FIGURE 5.1: Topography of watershed and riverbeds about the BWC confluence zone, with black solid contour lines showing elevation above sea level (m). Black dotted lines delineate the active channel during low flow, and the red dotted ellipse delineates a scour hole.

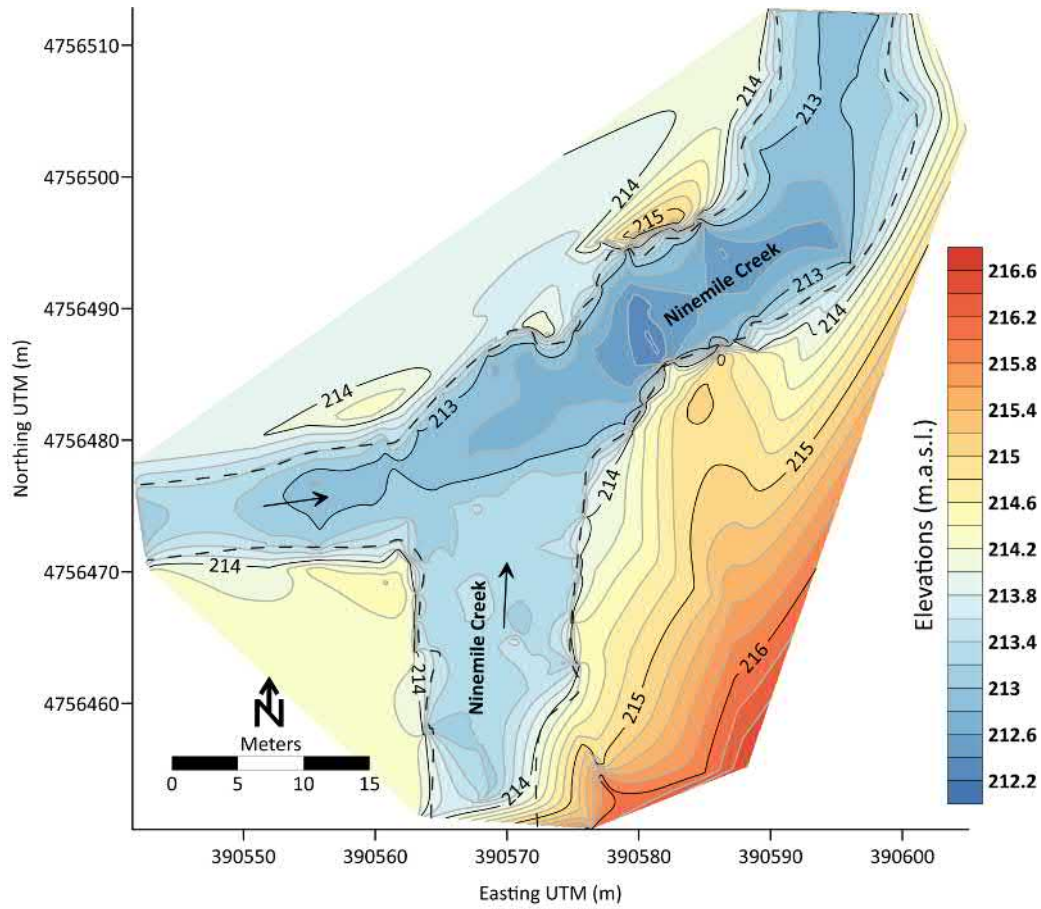


FIGURE 5.2: Topography of watershed and riverbeds about the NMC confluence zone, with black solid contour lines showing elevation above sea level (m). Black dotted lines delineate the active channel during low flow.

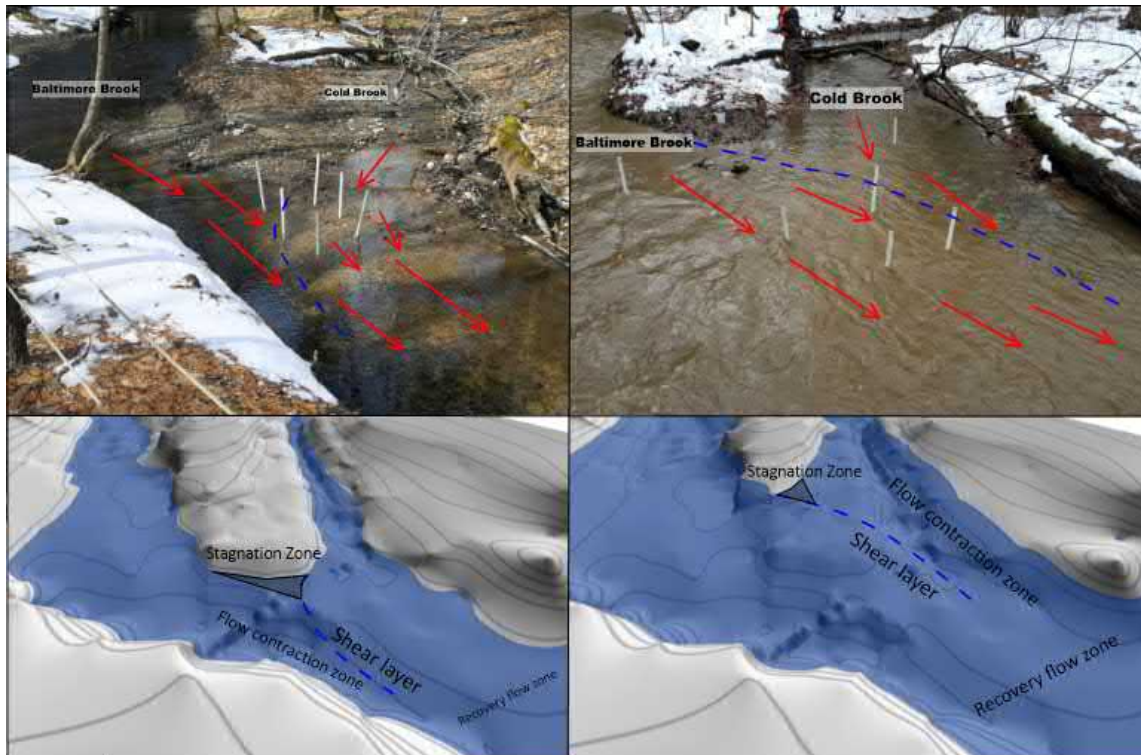


FIGURE 5.3: *BWC hydrodynamics observation. Typical flow structure at BWC (up) and a high-flow event in December 2018 with liquid precipitation and snowmelt (down).*

within the CHZ (see Figure 5.1). Flow paths induced by bed topography in CB defined length and width of a sand bar located downstream the CHZ (Cardenas et al. 2004; Song et al. 2017) and caused fine sand infiltration into the bed resulting in lower K_v .

However, visual observations yielded larger velocity from CB because of its bed morphology. The location of the shear layer (the dotted blue line in Figure 5.3) was moved towards the BB side, the mainstream, due to the dominant CB flow velocity. Downward fluxes have eroded BB riverbed forming a large scour hole within the CHZ. Flow paths induced by bed topography in CB defines length

and width of a sand bar located downstream the CHZ Rhoads and Sukhodolov (2001) and causes fine sand infiltration Rhoads and Kenworthy (1995) resulting in lower K_v .

TABLE 5.1: Low flow active channel width (m), depth (m), average velocity (m/s), and discharge (m^3/s) in BB, CB, and the confluence CHZ. Data for BB and CB were collected 1.5 meters upstream of the junction, and data for CHZ were collected 3 meters downstream of the river junction.

Parameters	BB	CB	CHZ
Width (m)	2.20	1.00	3.09
Depth (m)	0.31	0.08	0.24
Fr (—)	0.155	0.735	0.248
Re (—)	81720	48387	88411
U_{avg} (m/s)	0.268	0.635	0.376
Q_{avg} (m^3/s)	0.179	0.048	0.273

5.2.2 NMC site

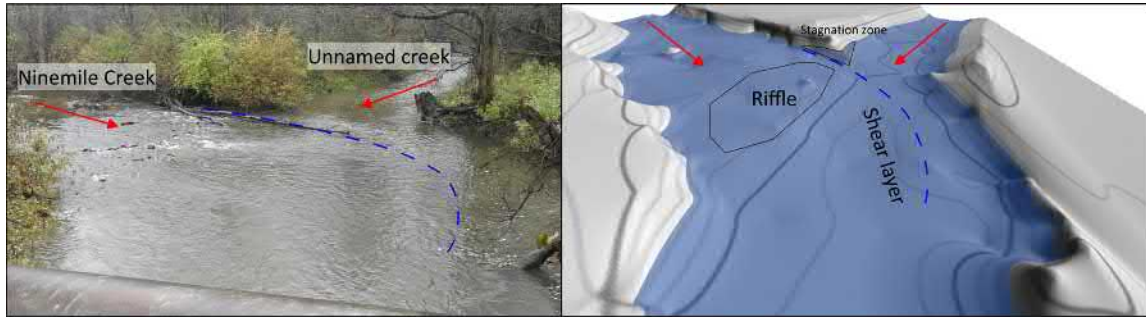


FIGURE 5.4: NMC hydrodynamics observation. Picture taken on 10/16/18 facing north (left) and typical flow structure at NMC (right).

NMC hydrodynamics was particularly complex and developed: several shear layers were visible caused by the presence of a couple of erosional zones in the

middle of Ninemile Creek mouth. In fact, a flow separation zone may be seen close to the erosional bank: bankful stage is 2 *m* approximately and riparian zone is mainly composed by woody vegetation with stretches of shrubs and herb mainly. Water depth was shallow at low stage (about 0.90-1.00 *m*) with ease of access thanks to a concrete bridge situated post-confluence. The latter constraints water flowing narrower, generating flow separation to its supports.

TABLE 5.2: *Low flow active channel width (m), depth (m), average velocity (m/s), and discharge (m³/s) in NC, UC, and the confluence CHZ. Data for BB and CB were collected 1.5 meters upstream of the junction, and data for CHZ were collected 3 meters downstream of the river junction.*

Parameters	NC	UC	CHZ
Width (<i>m</i>)	13.80	7.30	12.30
Depth (<i>m</i>)	0.380	0.480	0.420
Fr (—)	0.38	0.26	0.015
Re (—)	1023420	2688	209100
U_{avg} (<i>m/s</i>)	0.740	0.050	0.170
Q_{avg} (<i>m³/s</i>)	0.179	0.200	0.273

5.3 Grain size analysis

Five samples were extracted from BWC (BB4, BB5, CB4, CB5, CHZ4) and two samples from NMC (NM1 and NM2). The average of cumulative percentages of silt-clay ($PZ < 0.053 \text{ mm}$) and sand ($0.053 \text{ mm} < PZ < 2 \text{ mm}$) by weight are displayed in Table 5.3 and 5.4.

5.3.1 BWC grain size analysis

Grain size analysis result suggested that BWC confluence bed was mostly composed of coarse sand-gravel. In particular, the confluence zone was the highest

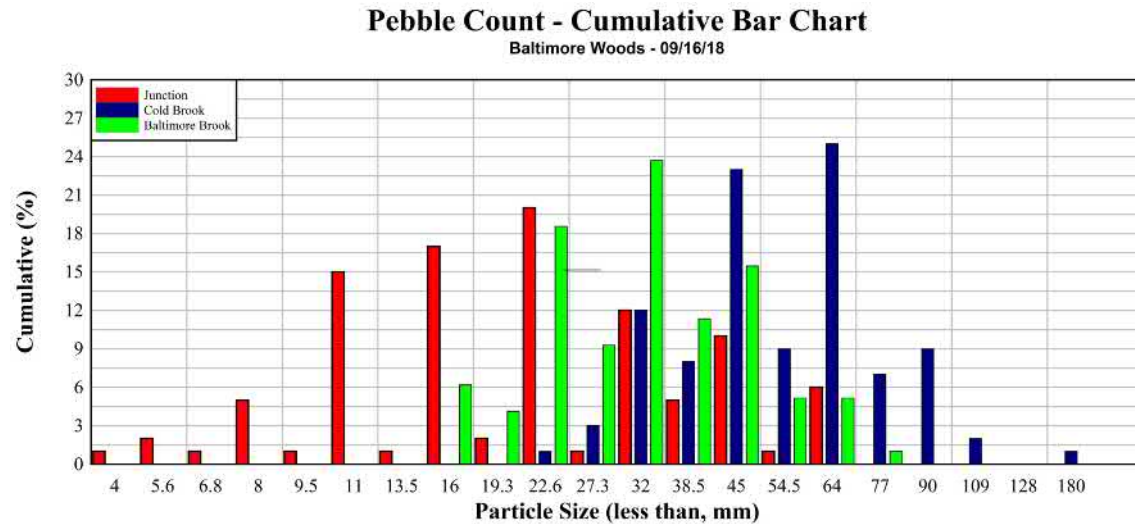


FIGURE 5.5: Results gathered after US SAH-97TM sieves at BWC.

in sand percentage while Cold Brook, the lowest one (gravel distribution on average). Pebble Count analysis, on September 16th 2018, gave an overall background of BWC site and it is in agreement with other confluence morphology (Figure 5.5). As far subsurface sediment collection was concerned, several samples were taken from BWC's tributaries and merging zone in December 2018. Soil laboratory analysis highlighted the presence of fine sand mostly across BWC site. However, collected sediments within the CHZ had more silt-clay fraction, instead.

5.3.2 NMC grain size analysis

Samples were collected where bed material was softer and less resistant to erosive power of the river. NMC is characterized by a steep gradient riverbed at confluence mouths with presence of rocks exposed above the flow surface. The collection area was chosen upstream the CHZ since water depth was shallower and easier to access. Grain size analysis showed a clear and different trend from BWC having coarser river sediment. Most of confluence bed sediment were within 1-2 mm range (Figure 5.7).

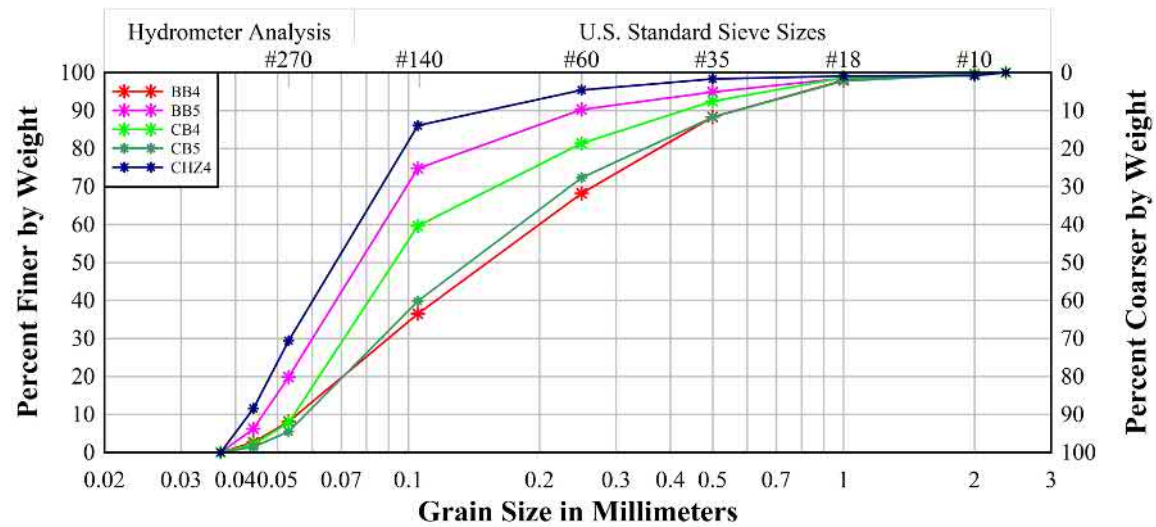


FIGURE 5.6: Soil grain size distribution within BWC, showing a fining of sand from upstream (BB and CB sites) to downstream into the confluence zone (CHZ).

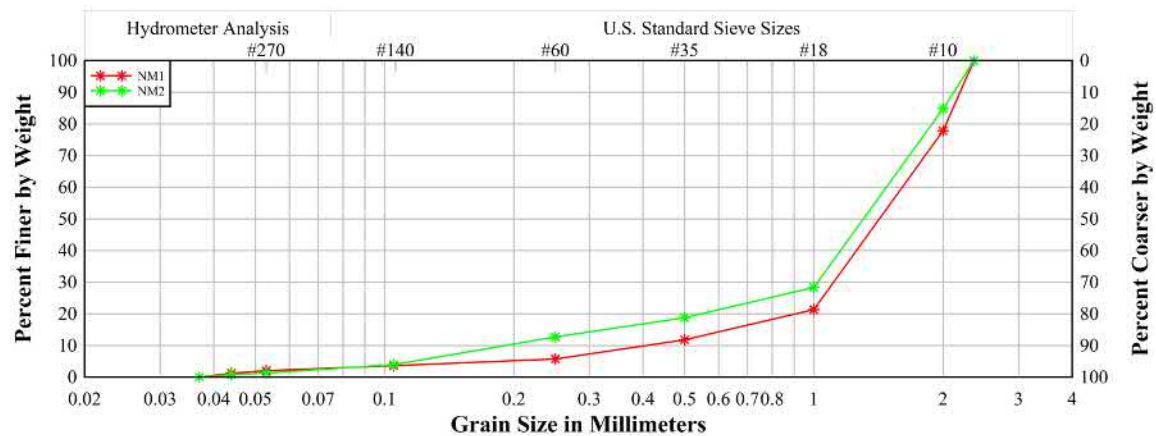


FIGURE 5.7: Soil grain size distribution within NMC, showing medium-fine sand at NM riverbed.

TABLE 5.3: *Sediment size distributions at BWC. Samples are referred to December 2nd 2018 collection. $\sigma_G = (d_{84}/d_{16})^{1/2}$, $S = (d_{90}/d_{10})^{1/2}$, $Gr = 1/2 \cdot (d_{84}/d_{50}) + (d_{50}/d_{16})$.*

Sample	BB4	BB5	CB4	CB5	CHZ4
Cumulative weight (%)					
< 0.053 mm	2.67	6.21	2.13	1.44	11.56
< 2 mm	99.64	99.46	99.57	99.52	99.18
d_{50} (mm)	0.152	0.077	0.092	0.136	0.068
Coefficient of uniformity η (–)					
σ_G	2.607	2.368	2.270	2.530	1.135
S	3.182	4.027	2.815	3.099	3.173
Gr	2.618	2.368	2.432	2.576	1.182
Average Porosity n (–)	0.406	0.404	0.415	0.408	0.439

5.4 Hydraulic conductivity tests

Hydraulic conductivity tests were carried out in spring (05/06/19 at BWC and 05/23/19 at NMC). Areas of interest were the Baltimore Brook, the Cold Brook and the confluence zone bed while the Ninemile Creek within NMC. Methodology is described in Section (4.4.4). In the following subsections, seasonal field campaigns results are reported and statistically analysed.

5.4.1 BWC test results

In this case, three test points each stream were used to conduct falling head method. Baltimore Brook values were the lowest of BWC and constantly on average. CB2 test point had the highest K_v value on the overall mean. CHZ results were slightly higher than tributaries ones.

TABLE 5.4: *Sediment size distributions at NMC. Samples are referred to May 23rd 2019 collection. $\sigma_G = (d_{84}/d_{16})^{1/2}$, $S = (d_{90}/d_{10})^{1/2}$, $Gr = 1/2 \cdot (d_{84}/d_{50}) + (d_{50}/d_{16})$.*

Sample	NM1	NM2
Cumulative weight (%)		
< 0.053 mm	1.25	0.82
< 2 mm	77.85	84.82
d_{50} (mm)	1.29	1.31
Coefficient of uniformity η (–)		
σ_G	1.596	2.295
S	2.088	10.310
Gr	1.618	2.498
Average Porosity n (–)	0.438	0.376

TABLE 5.5: *Statistical analysis of K_v during 05/06/19 field campaign. Values are in m/d.*

	Baltimore Brook			Cold Brook			CHZ		
	BB1	BB2	BB3	CB1	CB2	CB3	CHZ1	CHZ2	CHZ3
Lv	0.15	0.14	0.14	0.08	0.14	0.13	0.10	0.12	0.10
Range	0.011 0.019	0.013 0.016	0.014 0.037	0.002 0.003	0.046 0.766	0.010 0.012	0.030 0.042	0.072 0.088	0.006 0.014
Mean	0.015	0.014	0.027	0.002	0.330	0.011	0.033	0.082	0.008
Median	0.015	0.014	0.028	0.001	0.359	0.011	0.030	0.086	0.006
Dev.St	0.004	0.001	0.007	0.0008	0.278	0.0009	0.005	0.007	0.003

5.4.2 NMC test results

Tests were conducted during FS-NCUC2 two test points at Ninemile Creek riverbed. Ninemile Creek tributary and CHZ was considerably deep to allow field instrumentation to carry out this analysis. Column sediment was mainly composed by coarse and fine sand as illustrated in subsection (5.3.2). Values ranged from 0.305 to 0.587 m/d with a mean K_v of 0.439 and 0.353 m/d for NM3 and NM4, respectively. These results are in agreement with NMC grain size distribution and are a magnitude higher than BWC values.

TABLE 5.6: *Statistical analysis of K_v during 05/23/19 field campaign at NMC. Values are in m/d.*

	NM3	NM4
Lv	0.16	0.16
Range	0.343 0.587	0.305 0.450
Mean	0.439	0.353
Median	0.413	0.329
Dev.St	0.106	0.065

5.5 Piezometers results

Piezometers were used to measure respectively: water depth, VHG and Darcian fluxes. Water levels were recorded on a field book every field campaign and processed into a laptop with MATLAB and Microsoft Office package. Measurements were conducted exclusively in BWC.

5.5.1 BWC Vertical Hydraulic Gradients (VHG)

VHG values from 72 measurements covered a period of three observations (September 16 and 24 2018, November 6 2018) and ranged from downwelling (-0.177) to upwelling (0.303) across the confluence zone. Data were grouped in three groups: CHZ (confluence hydrodynamic zone), BB (Baltimore Brook) and CD (Cold Brook). VHGs were mostly Upwelling in CHZ and BB over field observations while Downwelling in CB, instead. Flow paths may be induced by bed topography (Cardenas et al. 2004; Song et al. 2016) and fine sand infiltration (Song et al. 2016, 2017) resulting in lower VHGs within the CHZ where there is a variation in bed slope as well.

However, VHG spatial distribution was highly variable in BWC and it might be addressed to its small spatial scale (water depth was in BB 30 cm while in CB less than 10 cm). Heterogeneity of fluxes was within acceptable range Song et al. (2016) and all field campaigns were demonstrated to belong to the same population of data by the nonparametric Kruskal-Wallis test ($p = 0.2928$). Piezometers

installed on confluence banks (P2 and P24) served as groundwater table monitors and showed a slight negative hydraulic head difference from water level of P2 to P24.

These observations might explain why CB WHGs were mostly downwelling: this trend was visible in September 24th campaign (5.7) Observations of November 6th, on the other hand, exhibited upwelling fluxes in CD and some downwelling in BB (while CHZ mostly upwelling). This variations might be explained by an increase in water depth (about 6 cm as observed from BWC measurements) with a consequently higher BB flow rate.

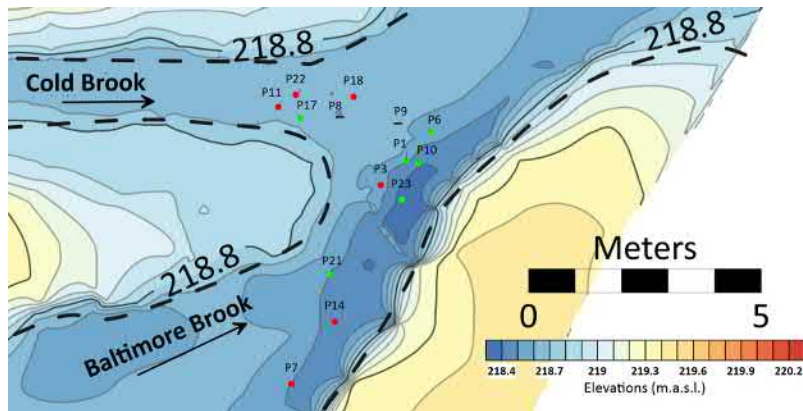
TABLE 5.7: Statistical analysis of VHG. Values are dimensionless. Downwelling and upwelling are negative and positive, respectively.

	Total	09/16/18	09/24/18	11/06/18
Range	-0.527 0.026	-0.177 0.150	-0.083 0.102	-0.136 0.303
Mean	-0.104	-0.005	0.013	0.053
Median	-0.046	-0.005	0.004	0.051
Variance	0.036	0.007	0.003	0.013
Dev.St	0.190	0.082	0.054	0.115

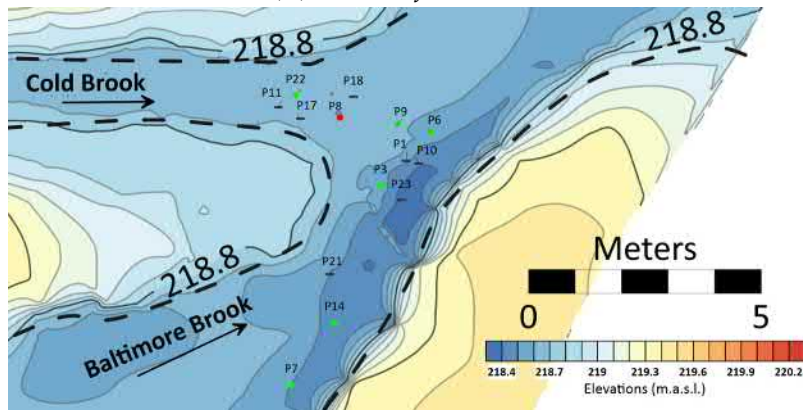
5.5.2 Transversal hydraulic gradients at BWC

Piezometers water levels revealed interesting values across BWC site. Head differences were slight even though evident pressure gradients were visible. In fact, upper piezometers row at confluence bar showed a decrescent trend in which static pressure decreased from CB towards BB. The lower row detected fluctuating values, instead.

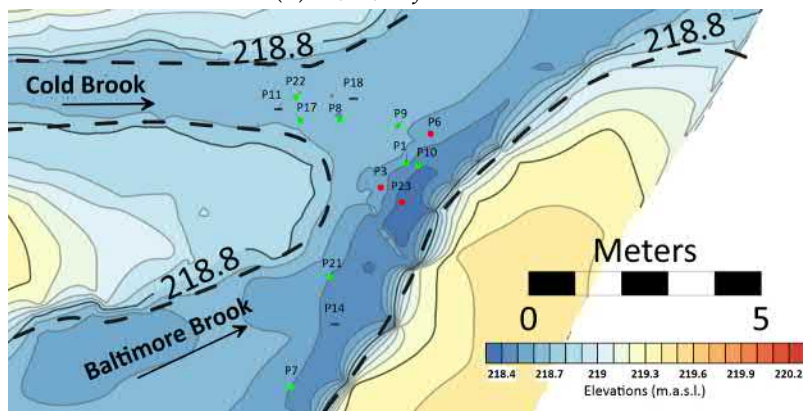
Findings from that area might be explained in the following ways: CB had higher velocity than BB influencing pressure gradients along transversal direction. On the other hand, BWC bed discordance, with CB bottom steeper than BB



(A) 09/16/18 field values.

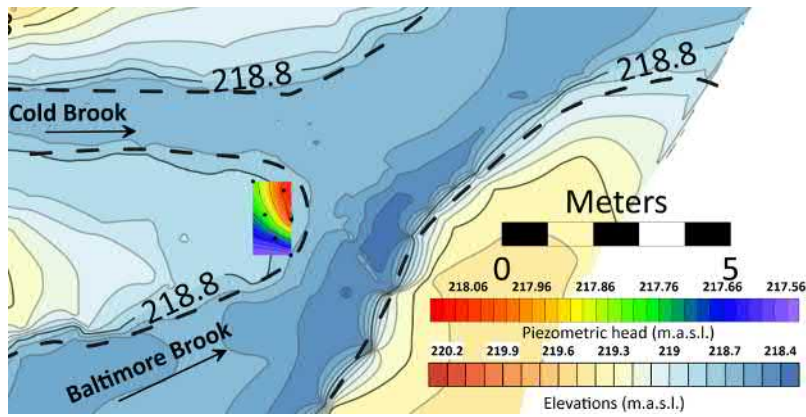


(B) 09/24/18 field values.

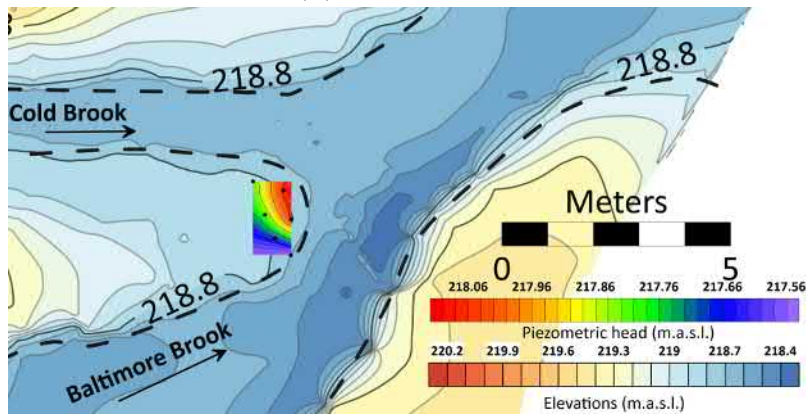


(C) 11/06/18 field values.

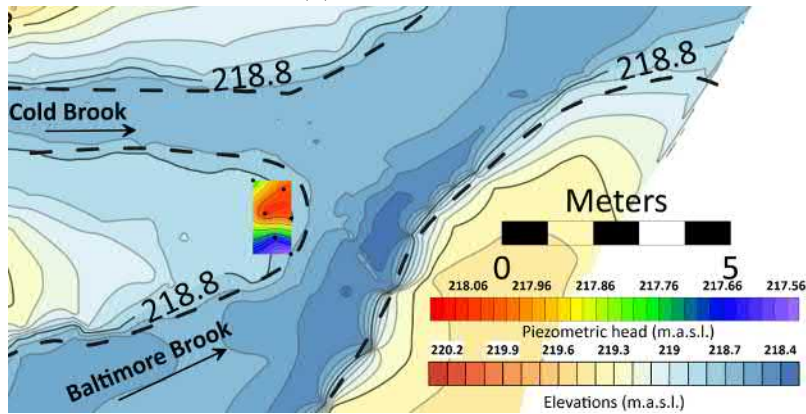
FIGURE 5.8: VHГ patterns at BWC. Green and red dots are downwelling and upwelling fluxes, respectively. Black dash represents no-exchange (pressure head gradient < 1 cm)



(A) 09/16/18 values.



(B) 09/24/18 values.



(C) 11/06/18 values.

FIGURE 5.9: *Pressure heads at BWC. Values are meters above mean sea water level.*

one, caused subsurface water to flow from North to South. In addition to that, confluence banks piezometers (P2 and P24, respectively) clearly evidenced that groundwater followed the same underneath path. Pressure gradient between P2 and P24 was of 0.02, 0.009 and 0.003 in September 16, 24 and November 6, respectively.

5.5.3 BWC darcian fluxes

Fluxes estimation was achieved using (3.4.2) with K_v obtained from hydraulic conductivity tests. Values ranged from -72 mm/d to 43 mm/d . These values reflected high spatial variability due to the complex morphology of BWC. Additionally, fluxes varied over observation period without confirming any significant trend. Darcian flux calculations took into account three different zones: BB, CB and CHZ. In fact, hydraulic conductivity slightly changed across confluence area and mean K_v values were calculated for each zone (Table 5.5). Fluxes within the CHZ (P1, P6, P9 and P10) were larger in magnitude on average while smaller in CB piezometers locations (P3, P7, P14, P21 and P23): it might be explained by the lower amount of silt and clay within the confluence junction.

However, there was no predominant downwelling and upwelling patterns existed as well within the CHZ. On the basis of confluence bar pressure gradient which was constantly directed from CB to BB bank, it would suggest that BB piezometers and some of CHZ should have downwelling patterns (indicating the discharge of groundwater into BB) but evidences were not found of this pattern. Pressure head readings suggested recharging streams but, due to lack of monitoring wells and a streambed stratigraphy, it could not be affirmed that P2 and P24 belong to the same aquifer.

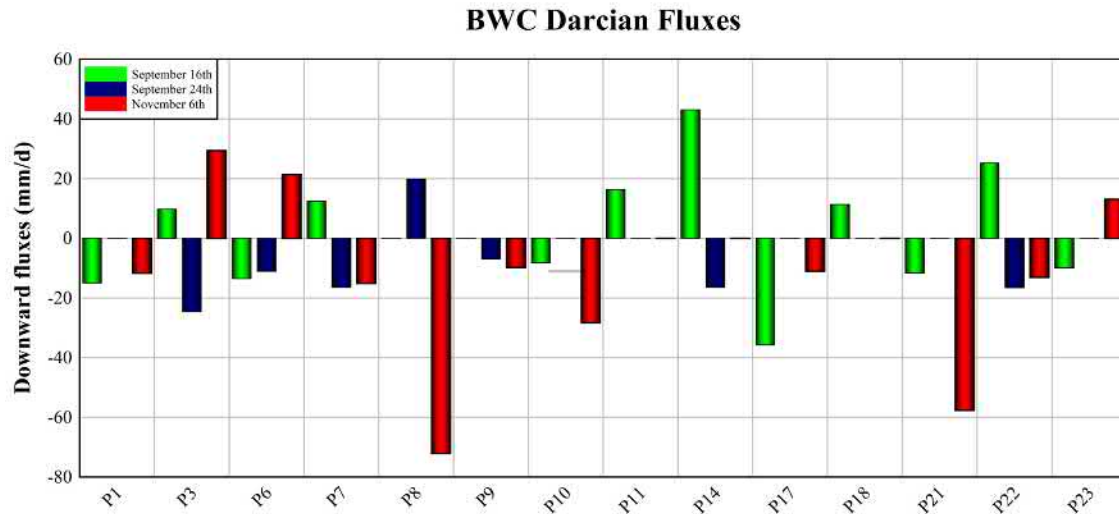


FIGURE 5.10: Darcian fluxes evaluated with hydraulic conductivity test results (Table 5.5).

5.6 Temperature time series

5.6.1 BWC results

Temperature distributions at different sediment layers obtained in BWC were post-processed through the analytical model (Equations 3.6.11 and 3.6.12) to estimate fluxes magnitudes, positive and negative values which indicated downward and upward fluxes, respectively. Results illustrated that vertical hyporheic fluxes had seasonal trends.

Hyporheic flux analysis to shallower sensors within 0-20 *cm* gap mostly over FS-BBCB1. In March 2019, after the snow melt, temperature pipes were replaced within BWC with a different sensors spacing configuration. Ibutton devices were inserted into temperature pipes with a 5 *cm* gap. They were eventually deployed on March 27 and retrieved on April 8 2019. Due to BWC small spatial scale, sensors at subsurface-water interface were not subjected to streambed scouring and did not come out during recording. Samples period varied from a couple of days

TABLE 5.8: *Statistical analysis of Darcian fluxes at BWC. Coefficient of variation (CV) and values are in mm/d*

	CHZ	CB	BB
Range	-72.16 to 19.84	-35.75 to 25.19	-57.68 to 43.06
Mean	-10.044	-4.102	-1.308
Median	-9.986	-3.407	-5.945
Variance	514.073	566.113	249.496
Dev.St	22.673	23.793	15.795
CV	-2.257	-5.801	-12.079

to a couple of weeks. DHR was applied to each temperature time series, to isolate the sinusoidal components with periods of 24h.

5.6.1.1 September 2018 BWC time series

During the fall season, temperatures ranged from 18.98 °C to 12.64 °C with notable temperature gradients among interface and subsurface sensors. In fact, on September 19, all the time series show a plunge in temperatures (especially in 0918B, Bw0918C and 0918E). On the other hand, sensors at 40 cm depth were barely affected by these temperature fluctuations: they recorded a 1 °C oscillation at most (0918B). However, variations in flux direction within the confluence were observed within the top 20 cm of the riverbed by temperature profile analysis. The probes at greater depths did not register sufficient temperature variation to register as vertical hyporheic fluxes. From September 16 to 23, fluxes ranged from 112 mm/d to -260 mm/d, with four of these upwelling fluxes in the upstream section of the confluence (0918A, 0918B, 0918C and 0918E, see 5.11). The single downwelling flux (0918D) was observed at the downstream section of the confluence. September results, thus, appear to indicate a gaining confluence with dominating downward fluxes (from September 16 to 24).

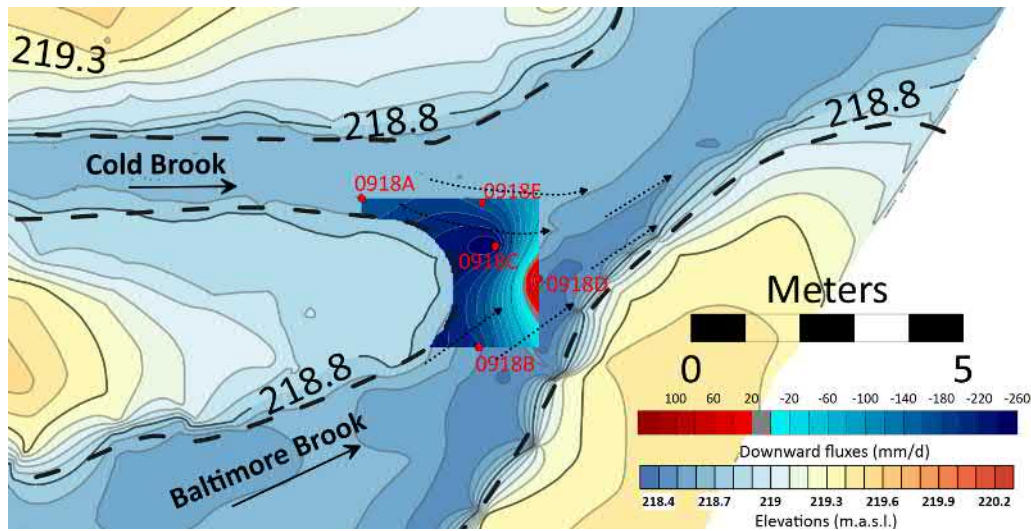


FIGURE 5.11: VHF map at BWC in September 2018 (FS-BBCB1). Downwelling and upwelling fluxes are illustrated by red and blue contours, respectively.

5.6.1.2 October-November 2018 BWC time series

In the mid-fall period, from October 23 to November 6 (1018), temperature was within the range of 10.35 °C and 6.55 °C. In Figure 5.12 it may be noticed three distinct patterns of vertical hyporheic exchange, during which time the site received 55 mm of precipitation and river stage increased 6 cm or 30%. During the beginning of this wet period, from October 23rd to October 25th, the first pattern involved maximum downwelling fluxes of 405 mm/d around rods 1018A, 1018B, 1018C and 1018F in the upstream section, and upwelling in the downstream section. In this period, the maximum daily upwelling fluxes gradually transitioned from -400 to -145 mm/d at rod 1018E, while upwelling remained steady at 1018D. The second pattern emerged on October 26th, when rod 1018E flux direction changed to moderately downwelling from a strong upwelling, and the upwelling at 1018D in the BB section of the confluence increased to a maximum of -140 mm/d (Figure 5.12). The third pattern emerged from November

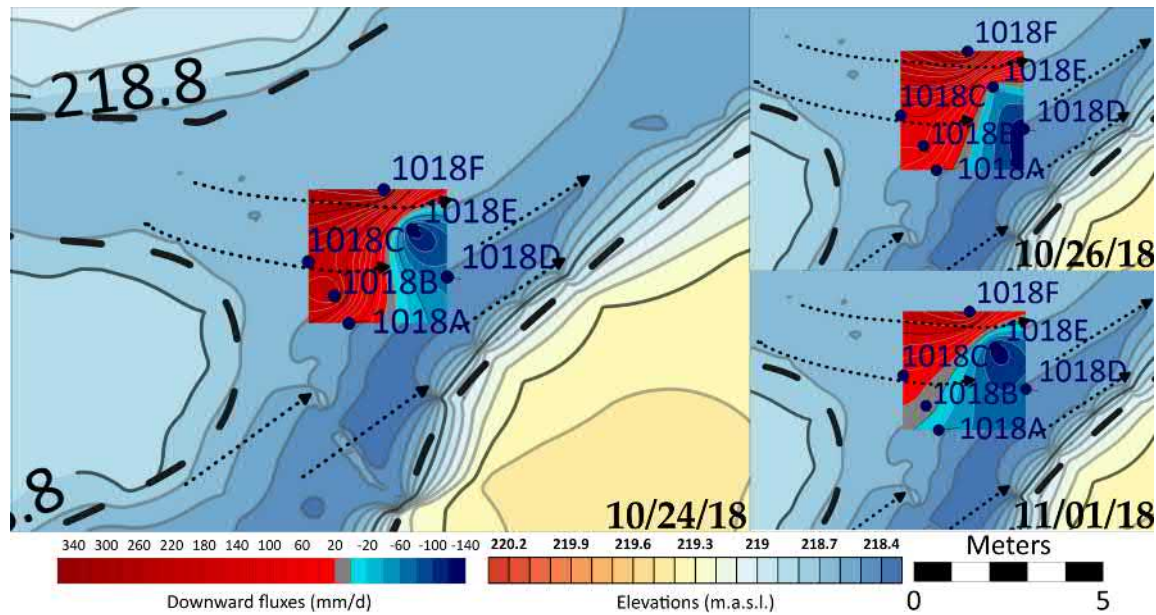


FIGURE 5.12: Vertical hyporheic fluxes (mm / d) for October 23 to November 6 2018, derived from temperature profiles. Light blue contour represents an interpolated transitional zone.

1st to November 6th when the upwelling hyporheic flux shifted further upstream along the BB side of the confluence to rods 1018A and the downwelling at rod 1018B ceased and became neutral. These changes in flux pattern suggest that BB transitioned to greater upwelling during the wet period, while downwelling flux in the CB section of the confluence was relatively steady.

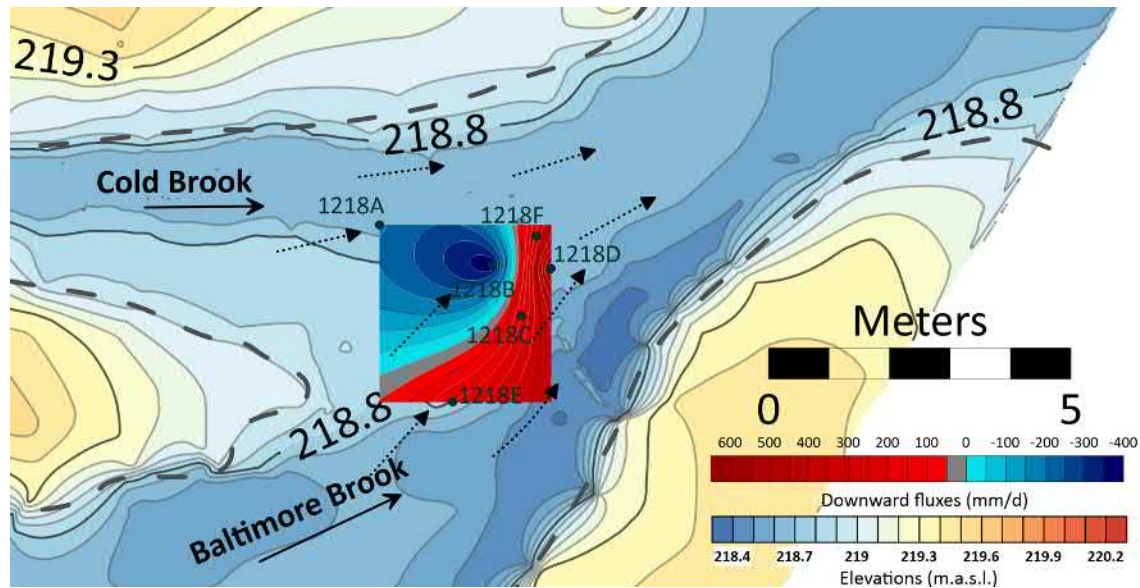


FIGURE 5.13: VHF map at BWC in December 2018 (FS-BBCB1). Downwelling and upwelling fluxes are illustrated by red and blue contours, respectively.

5.6.1.3 December 2018 BWC time series

Temperature values were taken every minute ranging from 5.72°C to -0.39°C and implemented fluxes ranged between 600 mm/d to -398 mm/d . As winter approached BWC, this third field campaign was aimed to understand fluxes pattern with cold, almost freezing, weather and water conditions: in late fall during December 2nd to 4th, after a month of little rainfall, the hyporheic fluxes reversed from the mid-fall pattern. The upwelling fluxes were organized along the CB upstream section of the, while downwelling fluxes were organized along the downstream confluence section and into the upper BB section. In this period, the CB temperature rods (1218A and 1218B) registered upwelling fluxes, while rods 1218D and 1218E had strong downwelling fluxes (Figure 5.13). As with the late summer period, but unlike the mid-fall with the rains, the December fluxes were steady values over the sampling period even though there was a steady decline in

river stage.

5.6.1.4 March-April 2019 BWC time series

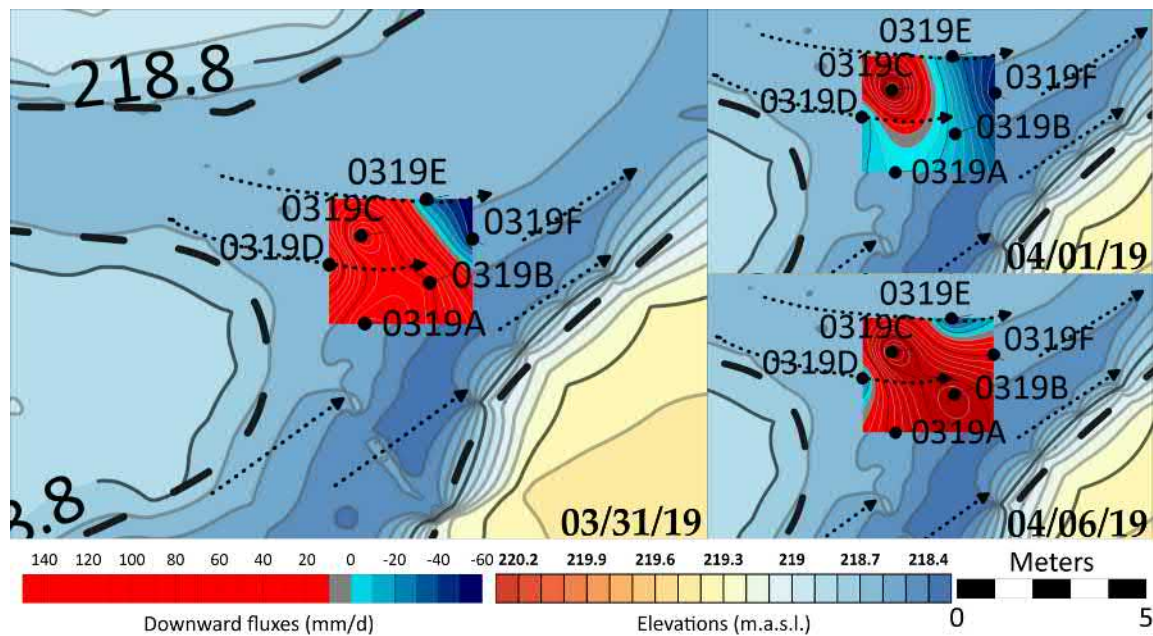


FIGURE 5.14: VHF map at BWC in March-April 2019 (FS-BBCB2). Downwelling and upwelling fluxes are illustrated by red and blue contours, respectively.

Temperature ranged between 10.36°C and 1.67°C while fluxes from 262.42 mm/d to -136.63 mm/d . The spring season brought changes in river flow, and this was used to organize three periods of distinct patterns in hyporheic flux. The changes in flow were attributed to a rainfall event between March 29th and 31st and another period of rainfall between April 3rd and 7th. At the end of the March rains, the downwelling fluxes were across most of the confluence, extending from the upper confluence to the lower section in the BB region, with an isolated corner of upwelling at rods 0319E and 0319F (Figure 5.14).

During the period between the rains, on April 1, the hyporheic flux pattern shifted and upwelling existed across most of the confluence, at all rods except for the rod 0319C in the upper confluence where CB entered. The continuation of rains from April 3rd to 7th resulted in a general return to the late March pattern of flux, with downwelling extending across most of the confluence, and upwelling at rod 0319E in the downstream section along the CB region, as well as at rod 0319D near the confluence vertex (Figure 5.14).

5.6.2 NMC results

The second confluence was investigated for a month during FS-NCUC2. Temperature rods were installed across Ninemile Creek and its unnamed tributary. Since NMC's CHZ was characterized by deep water depth, iButtons location was then constricted to a small region. Nevertheless, they were installed close to a topographic bed variation along Ninemile Creek mouth (Figure 4.15). Sensors recorded from mid-April to end of May 2019 sediment water time series: iButtons gap was set to 5 *cm* between a pair of sensors.

5.6.2.1 April-May 2019 NMC time series

The spring season at NMC was characterized by a distinct pattern in hyporheic fluxes. The sampling rate was of 15 *min* and the observation period lasted from April 17 to May 23, 2019. Water pore sediment had a temperature range of 6.5°C to 25.68°C and computed fluxes ranged between -300 *mm/d* to 800 *mm/d*. 0419A, 0419B and 0419C exhibited consistent patterns at NMC over the spring season. This row of temperature rods was located at a riffle tail, individuated at the rivers junction, where it is common to find upwelling zones Gariglio et al. (2013), a steady downwelling pattern was found. From a USGS gage located approximately 20 *km* downstream of NMC, changes in flow were attributed to several rainfall event between April and May 2019 (Figure 5.15) with a peak on May 15. Downwelling fluxes were across most of the observation period, extending from April 19 to the end of May, with an isolated corner of upwelling at rods 0419C on April 17 and 18 (5.16a).

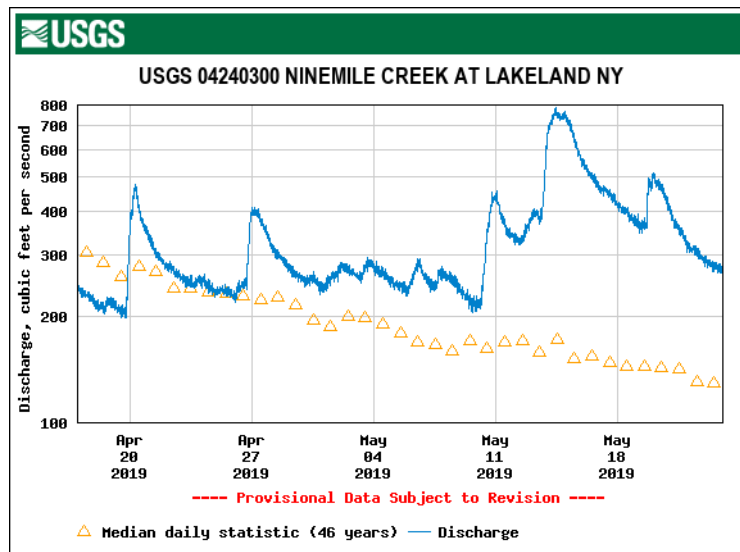
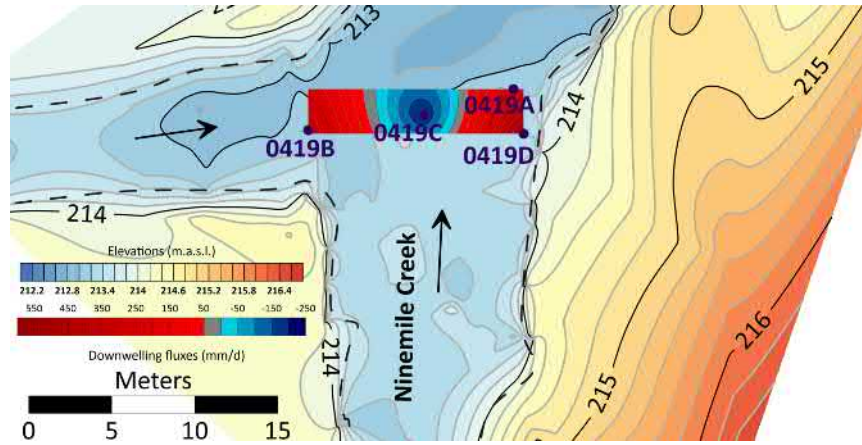
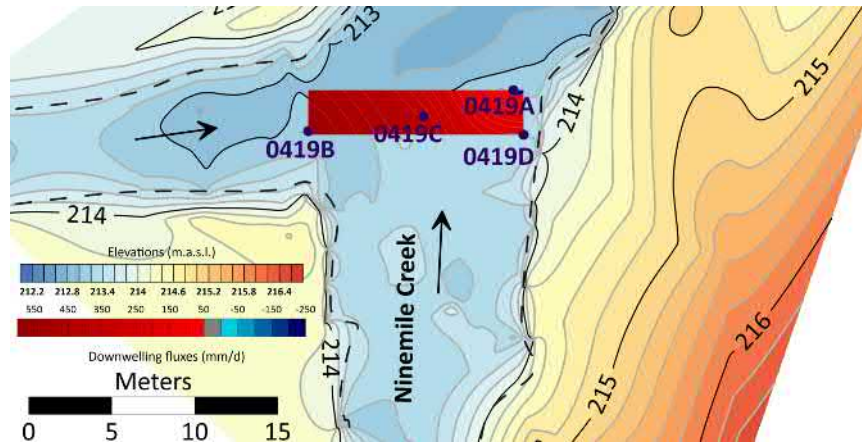


FIGURE 5.15: *Ninemile Creek runoff at gage 04240300 from April 17 to May 23, 2019 (Lakeland, NY).*

0419D rod detected variable flux directions before failed to record any data beyond May 7, 2019. In fact, during the period between April 21 to 24, the hyporheic flux pattern shifted to upwelling before recording downwelling again, and between May 2 to 7. This temperature rod was located within a flux acceleration zone close to the riverbank. The continuation of rains yielded stream water infiltrating into the ground recharging the local groundwater even though temperature records were taken during spring season.



(A) VHF on 04/18/19



(B) VHF on 05/01/19

FIGURE 5.16: VHF map of NMC. Downwelling and upwelling fluxes are illustrated by red and blue contours, respectively.

References

- Cardenas, B. M., J. L. Wilson, and V. A. Zlotnik
2004. Impact of heterogeneity, bed forms, and stream curvature on subchannel hyporheic exchange. *Water Resources Research*, 40(8).
- Chen, X.
2000. Measurement of streambed hydraulic conductivity and its anisotropy. *Environmental Geology*, 39(12).
- Gariglio, F. P., D. Tonina, and C. H. Luce
2013. Spatiotemporal variability of hyporheic exchange through a pool-riffle-pool sequence. *Water Resources Research*, 49(11):7185–7204.
- Gordon, R. P., L. K. Lautz, M. A. Briggs, and J. M. McKenzie
2011. Automated calculation of vertical pore-water flux from field temperature time series using the vflux method and computer program. *Journal of Hydrology*, 141-142:142–158.
- Rhoads, B. L. and S. T. Kenworthy
1995. Flow structure at an asymmetrical stream confluence. *Geomorphology*, 11(4):273 – 293.
- Rhoads, B. L. and A. N. Sukhodolov
2001. Field investigation of three-dimensional flow structure at stream confluences: 1. thermal mixing and time-averaged velocities. *Water Resources Research*, 37(9):2393–2410.

- Song, J., W. Jiang, S. Xu, G. Zhang, L. Wang, M. Wen, B. Zhang, Y. Wang, and Y. Long
2016. Heterogeneity of hydraulic conductivity and darcian flux in the submerged streambed and adjacent exposed stream bank of the beiluo river, north-west china. *Hydrogeology Journal*, 24(8):2049–2062.
- Song, J., G. Zhang, W. Wang, Q. Liu, W. Jiang, W. Guo, B. Tang, H. Bai, and X. Dou
2017. Variability in the vertical hyporheic water exchange affected by hydraulic conductivity and river morphology at a natural confluent meander bend. *Hydrological Processes*, 31(19):3407–3420. HYP-16-0947.R2.

Chapter 6

Relations between river confluence and hyporheic exchange

This field study found distinct upwelling or downwelling patterns of hyporheic exchange flux and observed its variation across eight months from late summer to spring seasons. During this period, these patterns exhibited variability while hydrodynamic and hydrological condition were changing. The result of this study must be examined within the context of field campaign budget, which led to some limitations. Firstly, BB, CB and NC (at study site) were ungauged streams and daily observations of discharge and water stage were not accomplished. It is acknowledged that the main drivers of hyporheic patterns are the relative levels of river stage and groundwater at regional scale Song et al. (2017). However, topographic irregularities and soil heterogeneity, in which temperature rods were deployed, generate nested flow paths at meter scale Tonina and Buffington (2007) which complicated the understanding of flux mechanism, since real vertical flux is unknown in field observations. Secondly, we chose distinctive confluence locations Best (1987) to carry our seasonal analysis at BWC and NMC to optimize our research within the hydraulic aspect of this subject.

6.1 Effect on variations in confluence geometry on the hyporheic fluxes

Regional and local drivers of hyporheic exchange influence the CHZ in different ways. In fact, at a regional scale, the dominant drivers of hyporheic exchange flux patterns are the relative levels of river stage and groundwater (Cardenas et al. 2004; Tonina 2008; Boano et al. 2014; Song et al. 2017; Cheng et al. 2019, while at local scale bed morphology, soil heterogeneity, and channel velocity influence hyporheic exchange Tonina (2008). In pool-riffle channels with moderate slope, such as BB and CB, hyporheic exchange is usually driven by the variability of the spatial distribution of channel velocity and resulting pressure head Buffington and Tonina (2009).

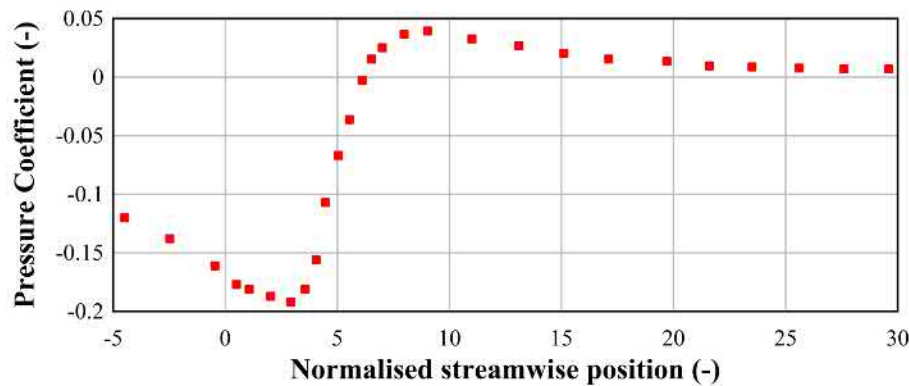


FIGURE 6.1: *Longitudinal distribution of pressure coefficient in a backward facing step Driver and Seegmiller (1985).*

In September 2018, at the confluence entrance the flow from CB tended toward the BB bank (Figure 5.3 left). At that time the area of measurement was located just downstream the junction corner, where the flow from BB is featuring an abrupt step at the entrance of the scour hole (Figures 5.11, 6.2, 6.3 and 6.4 a). The flow over a step is a classic type of separation flow, termed backward facing step flow (BFSF), which has been extensively investigated using both experimental Driver and Seegmiller (1985) and numerical methods.

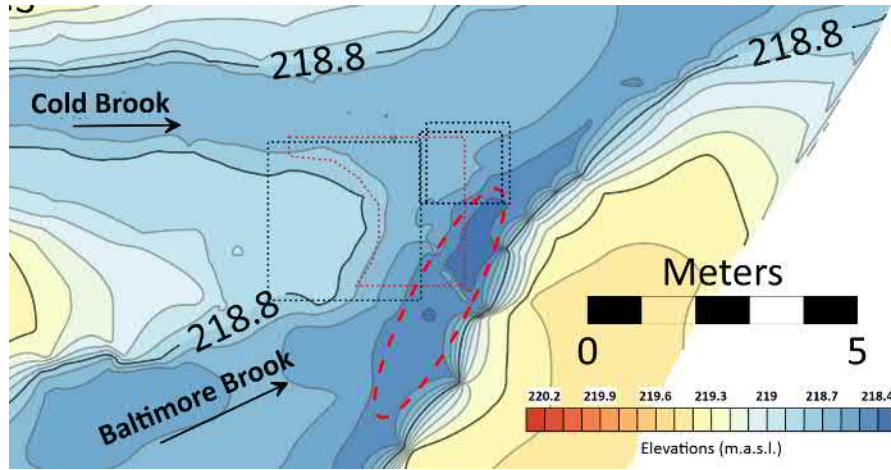


FIGURE 6.2: VHF map extents from FS-BBCB1 and FS-BBCB2. Red polygon refers to September 2018 map dark green, dark blue and black recall December 2018, October 2018 and March 2019 maps, respectively. The scour hole is individuated by the red ellipse.

It is well-known that in BFSF downstream the step bottom pressure is going down to a minimum at $x/H_{step} = 3.0$, which is followed by a rapid increase to get a maximum close to the reattachment point, located at $x/H_{step} = 9$ (Figure 6.5) Driver and Seegmiller (1985). In our case, as the step height is approximately 0.15 m , the maximum pressure should be located about 0918D point (Figure 6.4 a). This is consistent with the observed hyporheic fluxes, which were directed upward (upwellings) upstream and immediately downstream of the step bordering the scour hole and downward (downwellings) around 0918D point, where flow reattachment and maximum pressure should be located. On the other hand, in the area of measurement, the flow from CB is moving over a plane bed, where flow was accelerating, and upwelling was observed.

December 2018 pattern was affected due to a snowmelt event (Figure 5.14) causing an evident increase in discharge and river stage. Therefore, the junction angle changed accordingly with flow directions (Figure 5.1) delineating a

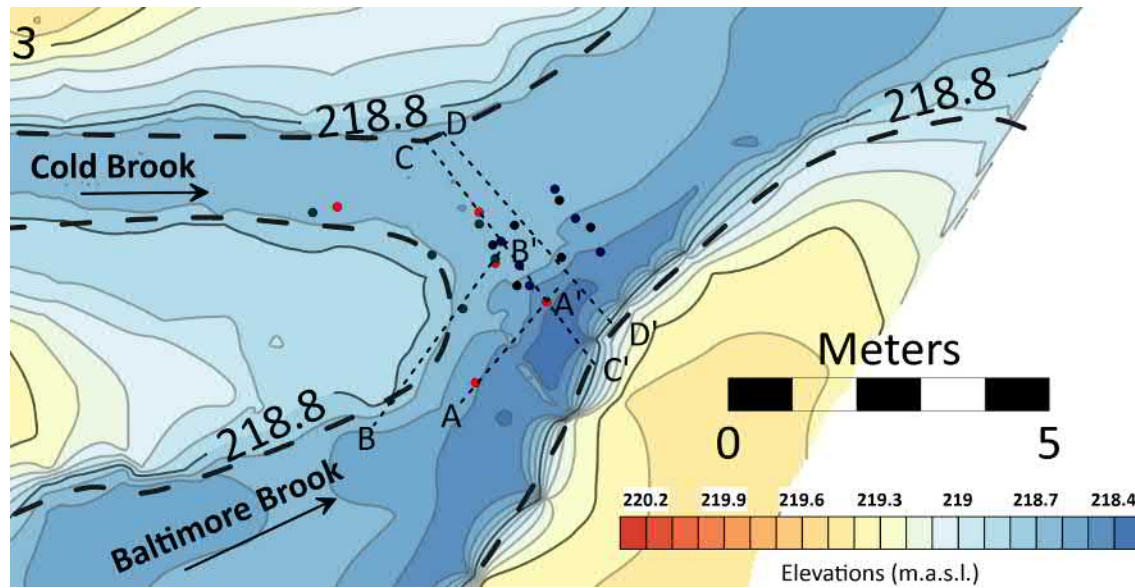


FIGURE 6.3: Test points and cross-section locations from FS-BBCB1 and FS-BBCB2. Red points refer to September 2018, light blue, dark blue and black recall to December 2018, October 2018 and March 2019, respectively. The red ellipse represents the scour hole.

new stagnation zone and shear layer, water circulation, velocity ratio and erosional/depositional patterns with evident results in hyporheic flux distribution and rate. The hyporheic fluxes organization observed in December 2018 suggests a pressure-head variation due to the new junction angle Buffington and Tonina (2009) that caused an extended and enlarged downwelling zone toward the middle of BWC, compared to September 2018 pattern. In fact, as flow increases and submerges bed topography, the bedforms exert less influence on the water-surface profile which becomes more uniform. However, this effect is not widely studied yet and this recent investigation highlights its potential importance of exchange dynamic.

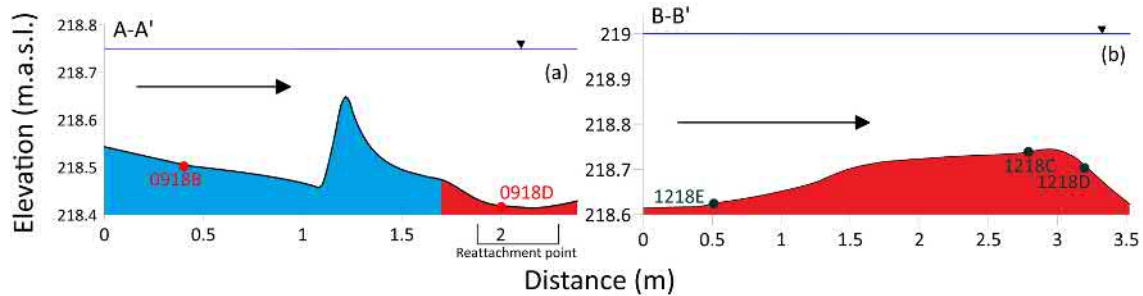


FIGURE 6.4: Longitudinal sections at BWC (AA' and BB'). Red and blue light fill depict downwelling and upwelling zones, respectively.

October 2018 vertical fluxes and March 2019 contour maps demonstrated variable patterns (Figure 5.12 and 5.14) since these observations were done downstream of confluence junction where water flow was subjected to more complex three-dimensional structures. Figure 6.5 shows the irregularity of the confluence bed in which 1018 and 0319 field campaigns were done. We may expect that that area was strongly related to lateral hyporheic exchange due to CB bend-like flow path.

6.2 Effect of secondary flows on the hyporheic fluxes

In October/November 2018 and March/April 2019 the area of measurement was located downstream of that in September and December 2018, in the shear layer region (Figure 6.2), where hydrodynamics is generally characterized by complex 3D patterns and helical flow cells are also often observed Rhoads and Kenworthy (1995), although their presence, characteristics and origin need further investigations Gualtieri et al. (2019). Following the back-to-back bend or meander analogy, these cells are expected to converge at the surface in the centre of the channel and to diverge near the bed (Mosley 1976; Rhoads and Kenworthy 1995; Rhoads and Sukhodolov 2001).

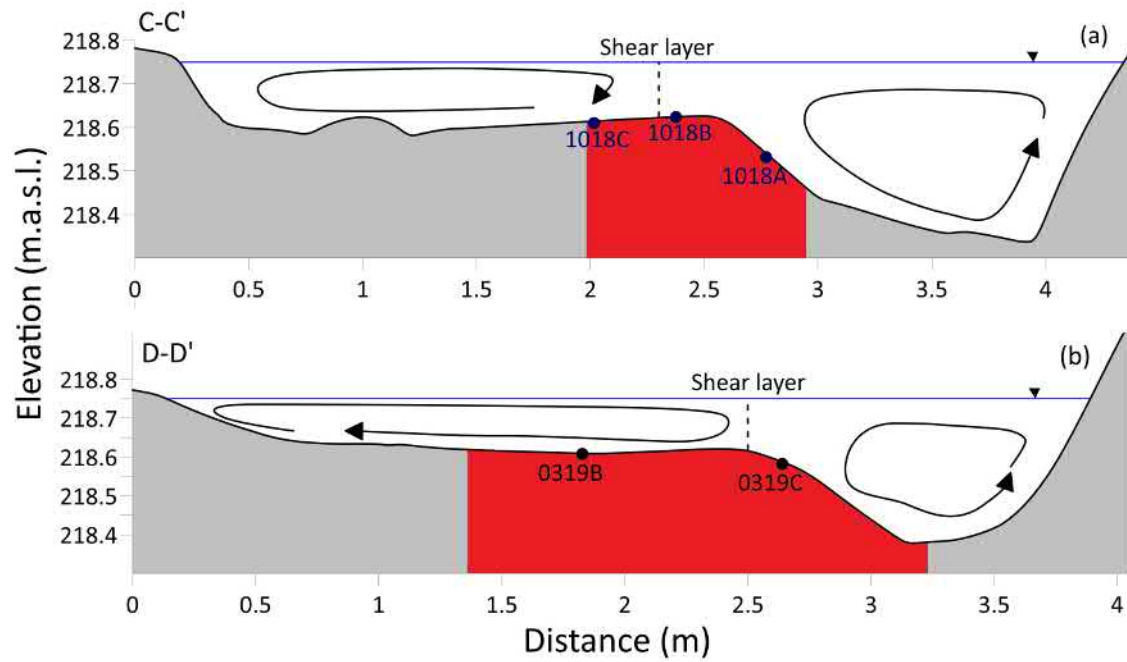


FIGURE 6.5: Cross sections at BWC (CC' and DD'). Dotted line shows shear layer position and helicoidal rotating cells represent ideal water circulation. Red and blue light fill depict downwelling and upwelling zones, respectively.

Furthermore, these helical cells are associated with downward and upward flow patterns in the water column which could have an impact even on the hyporheic exchange. Cheng et al. (2019) observed at the confluence between Juehe River and Haohe River (junction angle, 110°) downwelling patterns in the area across the shear layer where helicoidal flow cells were located. They argued that the encounter and impact of the two tributaries created in that area a downward flow causing a downwelling hyporheic exchange.

In the present study, it was not possible to confirm or not the presence of helical cells at the BWC confluence. However, confluence planform (Figure 5.1) and the related bend-like flow patterns of the tributaries might suggest the presence of the above secondary circulation. In October/November 2018, downwelling/upwelling was observed on the CB/BB side of the area of measurement, respectively, but some variations were noted from October to November (Figure 5.12).

In March/April, the distribution of the hyporheic fluxes was different, as almost only downwelling was measured on March 31 and April 6, while on April, 1 upwelling was predominant (Figure 5.14). Trying to explain this strong variability, two cross-sections located in the measurement area October/November 2018 and March/April 2019 were considered (Figure 6.3) and the distribution of the hyporheic fluxes was plotted (Figure 6.5 a/b). In October/November 2018 and March/April 2019 a downwelling region was observed across the shear layer about the scour hole (Figure 6.5 a/b). This could be related to the bed pressure distribution across the back-to-back bend at the confluence. At the end, the observed patterns in the distribution of hyporheic fluxes seem to be related to the hydrodynamics and morphodynamics characteristics about the confluence and their changes during the hydrological cycle.

Given the role of confluence junction angle in influencing hyporheic exchange flux, patterns of hyporheic fluxes are expected to fluctuate with changes in flow depth if the junction angle changes with channel depth of water. Further, given the role of momentum flux ratio influencing hyporheic flux, differences in water characteristics that lead to changes in density, temperature, conductivity and suspended sediment concentration, would likely trigger changes in hyporheic exchange patterns Gualtieri et al. (2019).

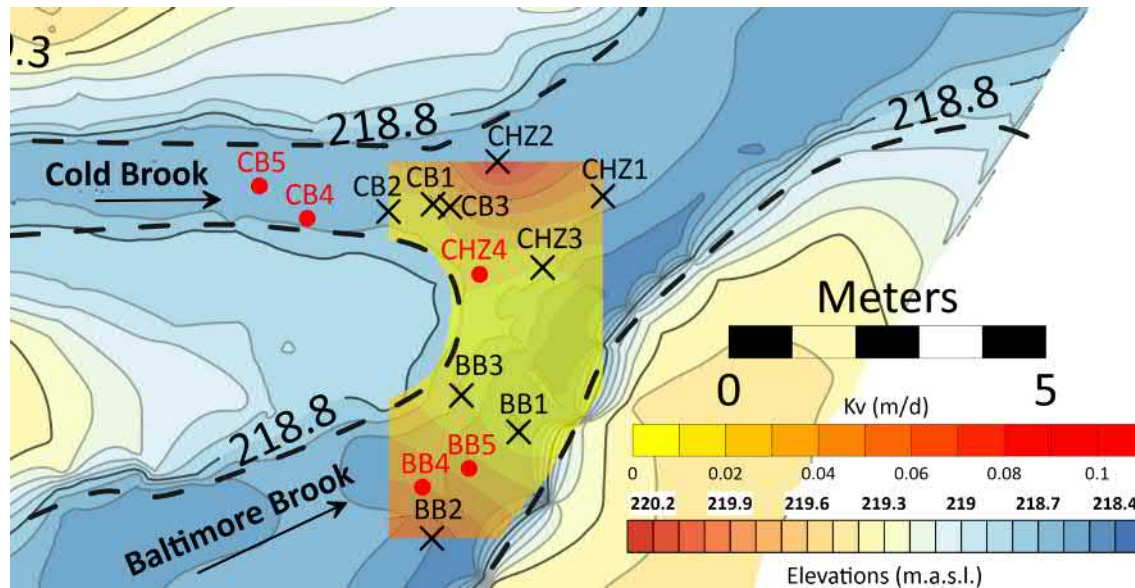


FIGURE 6.6: K_v map at BWC. Values range from higher (Red contour) to lower (Yellow contour) conductivity

6.3 Effect on variations in soil grain size and hydraulic conductivity

This field study found homogeneous fine sand at BWC and medium sand at NMC (Table 5.3 and 5.4). However, bed sediment particle distribution caused by erosional and depositional processes controlled by river confluence morphology had a notable effect on the hydraulic conductivity values. Elements such as junction angle and momentum flux ratio determine bed sediment allocation Song et al. (2017) causing heterogeneity in K_v . At BWC test site, low-flow condition were observed mostly over the field campaign determining K_v value distribution at BWC (Figure 6.6): the erosional bank (where BB1, BB2 and BB3 were located) yielded lower values in the BB segment due to layering of streambed sediments Jiang et al. (2015) caused by higher momentum flux Jiang et al. (2015); Song et al. (2016).

In fact, upwelling flux was individuated in September 2018 in BB. On the other

hand, the meandering path of CB might have increased K_v values, instead. In fact, laboratory analysis of substrate samples showed that grain size was mostly composed of coarser sand ($0.063 \text{ mm} < PZ < 0.2 \text{ mm}$) while the silt-clay fraction, on the other hand, was larger in CHZ sediments (Figure 5.6). NMC test site analysis was confined by the upstream section on the main channel: K_v and grain size distribution of UC were not achieved but relationship between NM1-NM2 and NM4-NM5 confirmed that K_v was small due to its position (pool) just before of a riffle, where stream velocity usually decreases Käser et al. (2009).

Fundamental role is also played by hydrological settings which may deposit fine sand, silt and clay during a flood event as observed at BWC in December 2018. A high-flow event affected flow circulation and deposited outwash material on the confluence bed which facilitates K_v heterogeneity across the channel: values were usually smallest in the middle of the stream and greater near the banks. In addition to that, past studies have also showed that K_v is related to water depth and sediment transport process Genereux et al. (2008). The study shows that distinctive stream morphologies have resulted in bedforms that correspond to erosion and deposition of the channel at each test site. Those contrasting erosion and deposition patterns led to different sediment distributions and spatial variability for K_v values at each test site. In fact, field campaigns showed very low K_v values throughout the confluences and spatial variability of K_v , across the channel along the lateral direction, generally occurred from bank to bank under different conditions of river morphologies. The values ranged from 0.002 to 0.082 m/d at BWC and from 0.353 to 0.439 m/d at NMC.

6.4 VHF estimating methods comparison

6.4.1 Temperature time series versus piezometers readings at BWC

During September 2018 (FS-BBCB1) temperature rods were installed nearby some PVC piezometers. Therefore, VHG results and analytic solutions from iButton sensors were compared in the post-processing stage. In Figure 6.7, the instruments configuration is showed from September 16 to 24. A couple of temperature pipes were inserted into BB and CB streambed, to monitor mouth streams vertical

exchange, and 3 other pipes were, instead, located at the junction. Their position was nearby some piezometers previously driven into BWC soil. 0918D and 0918E were close by P3, P23 and P8, P18 respectively. 0918A and 0918B were placed a bit dislocated from piezometers P11 and P21, respectively. This comparison takes into account 0918 iButtons time series and, as far VHG are concerned, daily observations of water levels of the same period.

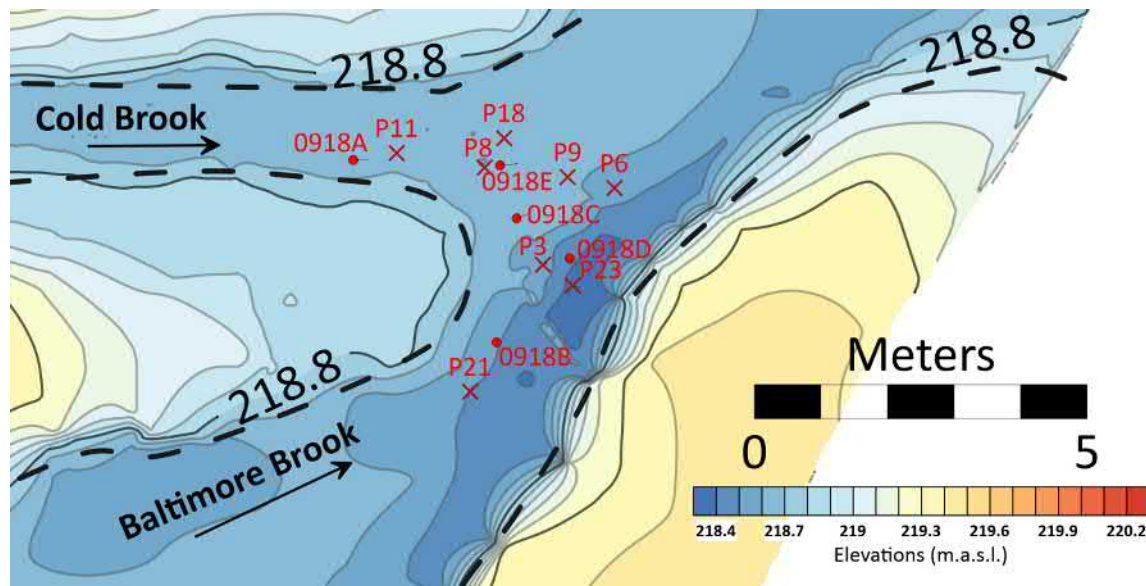


FIGURE 6.7: *iButtons rods and piezometers point locations during September 2018 (FS-BBCB1).*

Darcian flux magnitudes and directions were variable over the observing period considered. In fact, BB and CB fluxes (0918A and 0918B) estimated by VFLUX2 were oriented upward. P11 VHGs, by using an average of K_v methods results, yielded downward values over the observation period. P21 flux value (BB side) was in agreement with 0918B values, in particular magnitudes were close with September 24 observation.

The CHZ values were more uncertain: 0918D fluxes showed a downward direction while P3 and P23 were highly variable over the overall considered period.

P8 and P18 fluxes were mostly downward (except for September 24 in P18). However, VFLUX2 estimation, instead, showed upward fluxes. Therefore, a slight correlation was found between 0918B and P21 fluxes which had a the shortest gap. Darcian fluxes obtained by piezometers had an average sediment column of 30 *cm* and K_v tests were carried out at an average depth of 18 *cm*. VFLUX2 results had a different approach that uses thermal conductivity coefficient to estimate the vertical flux. These differences could explain the accuracy of this comparison.

TABLE 6.1: *Vertical fluxes calculation comparison. Values are in mm/d and positive downward.*

Instrument	Sep 16	Sep 24
P11	16.37	8.38
0918A	-202	-218
P21	-11.64	-3.41
0918B	-281	-249
P3	9.76	-24.69
P23	-9.92	5.76
0918D	150	150
P8	1.37	19.84
P18	11.31	-5.95
0918E	-221	-226

References

Best, J. L.

1987. *Recent Developments in Fluvial Sedimentology*, chapter Flow dynamics at river channel confluences: Implications for sediment transport and bed morphology. Society of Economic Palaeontologists and Mineralogists Special Publication 39.

Boano, F., J. W. Harvey, A. Marion, A. I. Packman, R. Revelli, L. Ridolfi, and A. Wrman

2014. Hyporheic flow and transport processes: Mechanisms, models, and biogeochemical implications. *Reviews of Geophysics*, 52(4):603–679.

Buffington, J. M. and D. Tonina

2009. Hyporheic exchange in mountain rivers ii: Effects of channel morphology on mechanics, scales, and rates of exchange. *Geography Compass*, 3(3):1038–1062.

Cardenas, B. M., J. L. Wilson, and V. A. Zlotnik

2004. Impact of heterogeneity, bed forms, and stream curvature on subchannel hyporheic exchange. *Water Resources Research*, 40(8).

Cheng, D., J. Song, W. Wang, and G. Zhang

2019. Influences of riverbed morphology on patterns and magnitudes of hyporheic water exchange within a natural river confluence. *Journal of Hydrology*, 574:75 – 84.

Driver, D. M. and H. L. Seegmiller

1985. Features of a reattaching turbulent shear layer in divergent channel flow. *AIAA Journal*, 23(2):163–171.

- Genereux, D. P., S. Leahy, H. Mitasova, C. D. Kennedy, and D. R. Corbett
2008. Spatial and temporal variability of streambed hydraulic conductivity in west bear creek, north carolina, usa. *Journal of Hydrology*, 358(3):332–353.
- Gualtieri, C., M. Ianniruberto, and N. Filizola
2019. On the mixing of rivers with a difference in density: The case of the negro/solimes confluence, brazil. *Journal of Hydrology*, 578:124029.
- Jiang, W., J. Song, J. Zhang, Y. Wang, N. Zhang, X. Zhang, Y. Long, J. Li, and X. Yang
2015. Spatial variability of streambed vertical hydraulic conductivity and its relation to distinctive stream morphologies in the beiluo river, shaanxi province, china. *Hydrogeology Journal*, 23(7):1617–1626.
- Käser, D. H., A. Binley, A. L. Heathwaite, and S. Krause
2009. Spatio-temporal variations of hyporheic flow in a riffle-step-pool sequence. *Hydrological Processes*, 23(15):2138–2149.
- Mosley, M. P.
1976. An experimental study of channel confluences. *Journal of Geology*, 84:535–562.
- Rhoads, B. L. and S. T. Kenworthy
1995. Flow structure at an asymmetrical stream confluence. *Geomorphology*, 11(4):273 – 293.
- Rhoads, B. L. and A. N. Sukhodolov
2001. Field investigation of three-dimensional flow structure at stream confluences: 1. thermal mixing and time-averaged velocities. *Water Resources Research*, 37(9):2393–2410.
- Song, J., W. Jiang, S. Xu, G. Zhang, L. Wang, M. Wen, B. Zhang, Y. Wang, and Y. Long
2016. Heterogeneity of hydraulic conductivity and darcian flux in the submerged streambed and adjacent exposed stream bank of the beiluo river, north-west china. *Hydrogeology Journal*, 24(8):2049–2062.

- Song, J., G. Zhang, W. Wang, Q. Liu, W. Jiang, W. Guo, B. Tang, H. Bai, and X. Dou
2017. Variability in the vertical hyporheic water exchange affected by hydraulic conductivity and river morphology at a natural confluent meander bend. *Hydrological Processes*, 31(19):3407–3420. HYP-16-0947.R2.
- Tonina, D.
2008. *Fluid Mechanics of the Environmental Interfaces*, chapter Surface water and streambed sediment interaction: the hyporheic exchange, Pp. 1–44. Taylor & Francis.
- Tonina, D. and J. M. Buffington
2007. Hyporheic exchange in gravel bed rivers with pool-riffle morphology: Laboratory experiments and three-dimensional modeling. *Water Resources Research*, 43(1).

Part III

Chapter 7

Conclusions

The current study focuses on hydrodynamic and morphological drivers of spatial and temporal patterns of hyporheic exchange at river confluences, based on the Song et al. (2017); Cheng et al. (2019) field work between the Juehe River and the Haohe River in the southern region of Xi'an City, Shaanxi Province, China. The aim is to fill the existing gap on the hydrodynamic, morphological processes and seasonal variations associated with hyporheic exchange at river confluences. The initial results commit to provide additional understanding to these processes. In this Chapter a concise summary of thesis structure is given.

The field study aimed the attention to three distinct aspects related to hyporheic flux mechanism:

- Confluence morphology
- Porous media characteristics
- Hydrodynamic structure of the flow

Two river confluences were chosen to carry out a field study on hyporheic fluxes: first site was found in the "Baltimore Woods Nature Center" natural park at Marcellus (NY, USA). The granulometric analyzes of the river bed material showed a composition of fine sand - coarse in majority.

Both confluences were surveyed with a total station (TopCon GTS 250) to obtain bathymetrys and profiles. The piezometric measurements, on the other hand, were carried out using mini-wells inserted in characteristic points of the study areas: through the measurements of the vertical hydraulic gradients, it was possible

to obtain the VHG, the hyporic flows (using the Darcy formula) and the piezometric dimensions. In the BBCB confluence, considering the reduced spatial scale of the phenomenon and the confluence, it was easier to obtain water level measurements than in the case of NM, where greater depth worsened the working conditions.

The piezometric measurements were collected from September until November 2018: it is clear from the initial processing of the collected data that the measurements are mainly influenced by the change in the water level and the flow rate, rather than by the hydrodynamic regime of the confluence: vi is the presence of a negative pressure gradient from the tributary with greater momentum towards that with less quantity.

As for temperature measurements and the use of the heat exchange equation to derive hyporic flows, temperature sensors called "Ibuttons" have been used which allow you to record temperature changes at regular time intervals. They were used exclusively on the BBCB confluence, being easily accessible and shallower for making measurements.

As they were not water resistant, it was necessary to install the sensors inside special PVC pipes with the application of waterproof silicone. The tubes were equipped with three sensors each positioned respectively at 0, 20 and 40 cm from the river bed. The measures have been carried out in different periods of the year (September-October, November and December) to observe seasonal and spatial variations of hyporic flows. To derive the direction and magnitude of the exchanges between surface and underground water, the method widely known as Hatch was used: it uses the amplitude or phase variations of the time series of temperature. The data showed a constant behavior of the flows generated in the hyporic zone. It should be noted, however, a greater variability in case of external temperature change which has led, in some cases, to significant changes in the direction of the exchanges: in any case, it is still being analyzed to establish its effective cause.

Land survey yielded the bed morphology of two river confluences in Marcellus, USA. Low channel slopes and sinuosity were distinctive of pool-riffle channels. They commonly have pools composed of fine material (fine sand, gravel)

and variable straight to meandering paths. Hyporheic exchange is driven by spatial pressure head variations as it was appreciated in BWC and NMC field campaigns. In fact, bedform influence was found in September 2018 and April 2019 where temperature rods were placed in peculiar points. Downwelling/upwelling patterns were strictly related to confluence morphology. The presence of a scour hole, typical feature of a nodal fluvial system, determined low pressure (downwelling) and high pressure (upwelling) on toe and the crest of cavity, respectively. Confluence junction angle governed flow circulation and hydrodynamic zones shifting back stagnation zone and relocating the shear layer during a high-flow event. The variation of the dynamic pressure affected vertical flow pattern compared to low-flow condition patterns. However, we expect that velocity gradients were highly variable over seasons; Gradation of the bed sediment showed that BWC and NMC site were mostly sandy-gravel and hydraulic conductivity tests reported very low values, suggesting that fine sediments were transported into pores reducing soil permeability. However, dependence was as well under investigation in this study. Seasonal hydrological condition needed to be taken into account. There was a visible pattern among October 2018 and March 2019 temperature rods: in these two cases fluxes were not driven by morphological or hydrodynamic conditions. VFLUX2 estimated fluxes had a constant rate and were less spatially variable than Darcian fluxes obtained from piezometers readings. In addition to this, seepage directions obtained through these two methods were barely in agreement. VHG values may have deceived vertical patterns due to soil heterogeneity in which piezometers were deployed.

Main findings may be summed up as it follows:

- Soil samples showed that BWC and NMC sites were mostly sandy-gravel and hydraulic conductivity tests reported very low values, suggesting that local sediment transport processes allocated fine sediments into pores reducing soil permeability.
- Confluence geometry, hydrodynamics and morphodynamics were found to significantly affect hyporheic exchange rate and patterns. In September and December 2018, local scale bed morphology, such as the confluence scour

hole and minor topographic irregularities, influenced the distribution of bed pressure head and the related patterns of downwelling/upwelling at BWC.

- Variation in hydrological conditions during a high flow event at BWC in December 2018 survey were seen to modify confluence geometry, such as junction angle and position, and, in turn, flow circulation patterns, shifting back the stagnation zone and relocating the shear layer. The hyporheic flux pattern in low flow conditions was modified where upwelling was mostly observed, and partially over a stepped bed, downwelling was measured.
- In October/November 2018 and March/April 2019, classical back-to-back bend planform and the related secondary circulation probably affected hyporheic exchange patterns around the confluence shear layer at BWC.
- Seasonal hydrological condition should be taken into account. There was a visible pattern among October 2018 and March 2019 temperature rods at BWC: in these two cases fluxes were not only driven by morphological or hydrodynamic conditions. In fact, downwelling patterns were consistent and found at NMC over April/May 2019 suggesting that vertical hyporheic fluxes were obtained due to a losing stream condition at NM.

Follow-up work must focus the relationship among soil permeability, flow momentum changes and groundwater which are still under investigation for this complex study. Monitoring streams discharge and vertical fluxes become crucial for a first insight to hyporheic dynamics within a complex riverine system such a confluence in order to highlight main factors such as seasonal and regional changes and drivers of surface-subsurface water interaction.

Further developments

The present investigation is limited to a relatively small number of observed points that partially covers a broad range of influent factors on the dynamics of hyporheic fluxes at river confluences. The experiments presented herein were conducted on field and the results only refer to hypothetical flow condition. Nevertheless, this research study contributes to widen the current knowledge on the hydraulic and morphological processes of hyporheic fluxes at river confluences. The following topics are proposed for future investigations which must focus on:

- Relationship among soil permeability, flow momentum changes and ground-water which are still under investigation for this complex study
- Monitoring streams discharge and vertical fluxes become crucial
- Factors such as seasonal and regional changes as drivers of surface-subsurface water interaction

References

Cheng, D., J. Song, W. Wang, and G. Zhang

2019. Influences of riverbed morphology on patterns and magnitudes of hyporheic water exchange within a natural river confluence. *Journal of Hydrology*, 574:75 – 84.

Song, J., G. Zhang, W. Wang, Q. Liu, W. Jiang, W. Guo, B. Tang, H. Bai, and X. Dou

2017. Variability in the vertical hyporheic water exchange affected by hydraulic conductivity and river morphology at a natural confluent meander bend. *Hydrological Processes*, 31(19):3407–3420. HYP-16-0947.R2.

Appendix

Appendix A

Temperature time series charts

In this appendix, temperature time series of the measurements performed in the field surveys in Marcellus are illustrated for every rod. The following information is shown for each experiment:

- Temperature profile of each field survey where iButtons sensors were deployed: FS-BBCB1, FS-BBCB2 and FS-NCUC2.
- 1, 2 and 3, at the end of each curve, indicate relative position from surface-subsurface interface. 3 is for an iButton sensor at $x = 0$, 2 is the middle sensor and 1 represents the deepest one.

0918, 1018 and 1218 BWC time series had an iButton spacing of 20 *cm* (3 is at $x = 0$, 2 is at $x = 20$ and 1 at $x = 40$) while 0319 had a spacing of 5 *cm* (3 is at $x = 0$, 2 is at $x = 5$ and 1 at $x = 10$). Uncompleted temperature profiles are due to fail in recording from iButton sensor.

At NMC, 0419 had a spacing of 5 *cm* (3 is at $x = 0$, 2 is at $x = 5$ and 1 at $x = 10$). Uncompleted temperature profiles are due to fail in recording from iButton sensor.

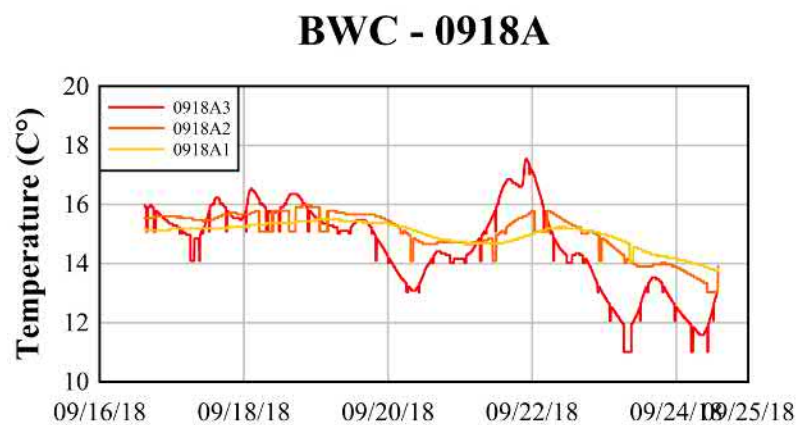


FIGURE A.1: Temperature time series at BWC during 0918 (FS-BBCB1).
Temperature probe A.

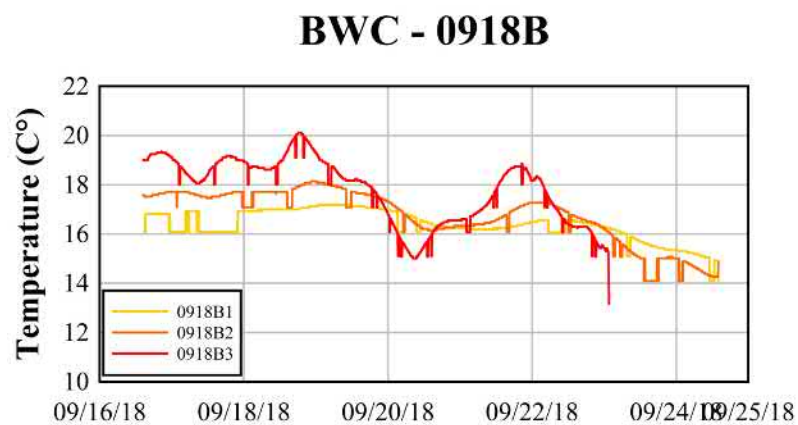


FIGURE A.2: Temperature time series at BWC during 0918 (FS-BBCB1).
Temperature probe B.

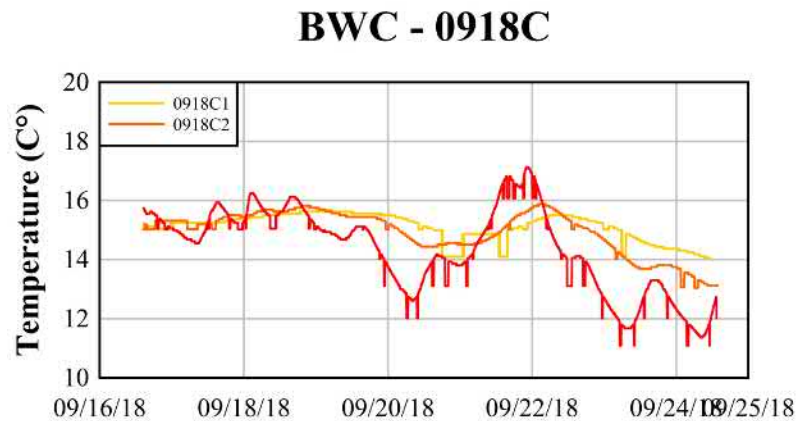


FIGURE A.3: Temperature time series at BWC during 0918 (FS-BBCB1).
Temperature probe C.

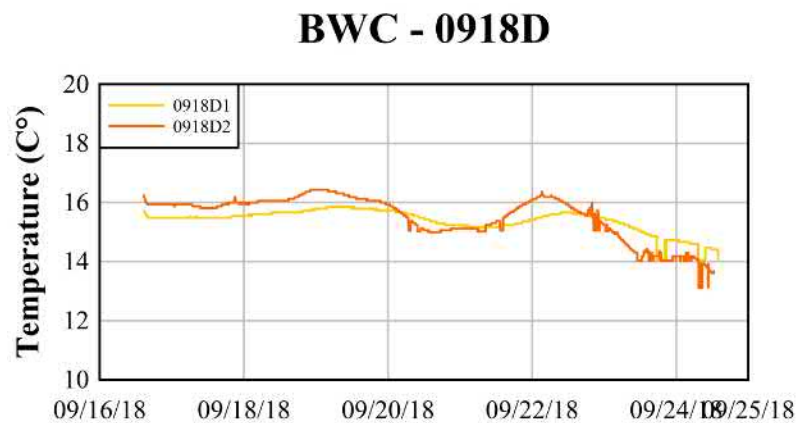


FIGURE A.4: Temperature time series at BWC during 0918 (FS-BBCB1).
Temperature probe D.



FIGURE A.5: Temperature time series at BWC during 0918 (FS-BBCB1).
Temperature probe E.

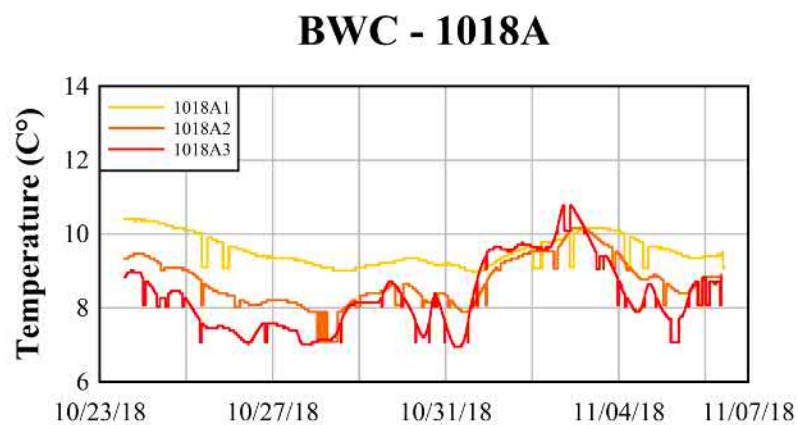


FIGURE A.6: Temperature time series at BWC during 1018 (FS-BBCB1).
Temperature probe A.

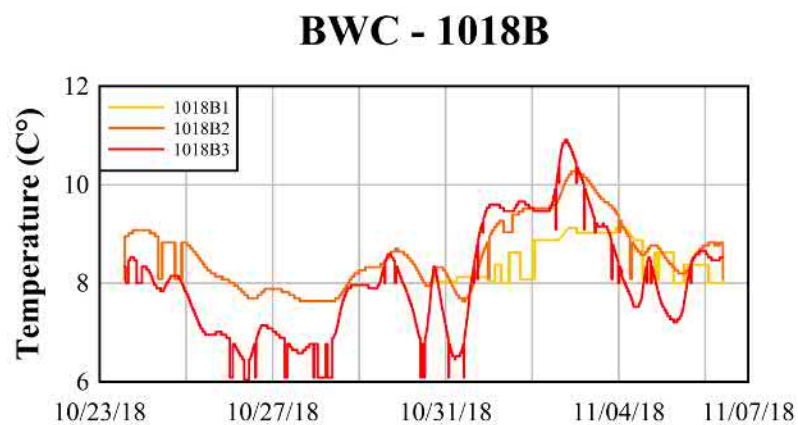


FIGURE A.7: Temperature time series at BWC during 1018 (FS-BBCB1).
Temperature probe B.

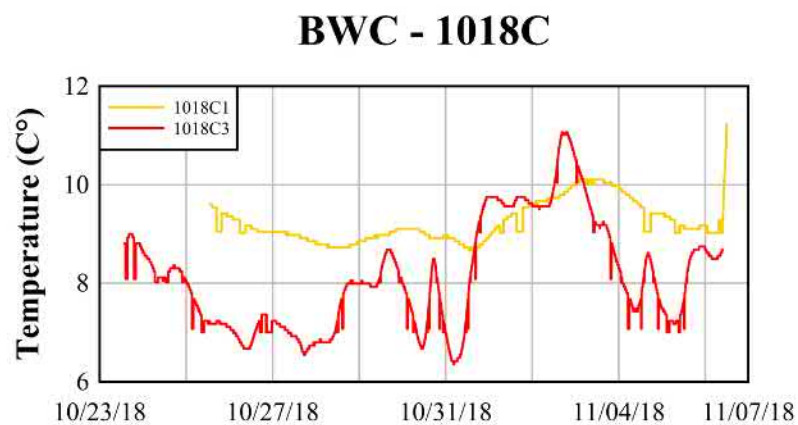


FIGURE A.8: Temperature time series at BWC during 1018 (FS-BBCB1).
Temperature probe C.

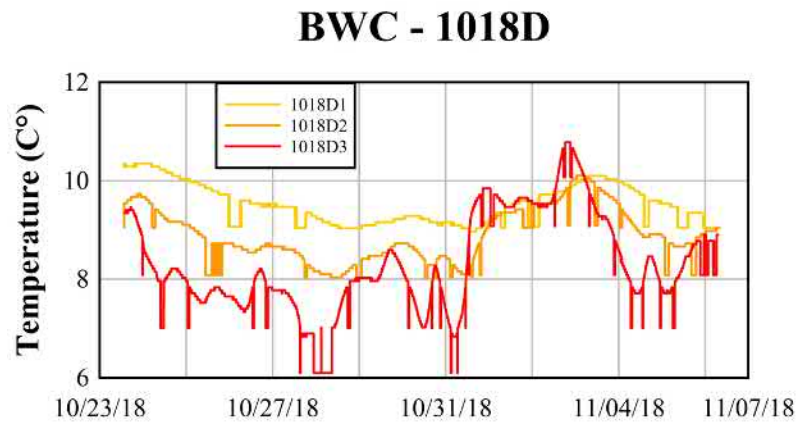


FIGURE A.9: Temperature time series at BWC during 1018 (FS-BBCB1).
Temperature probe D.

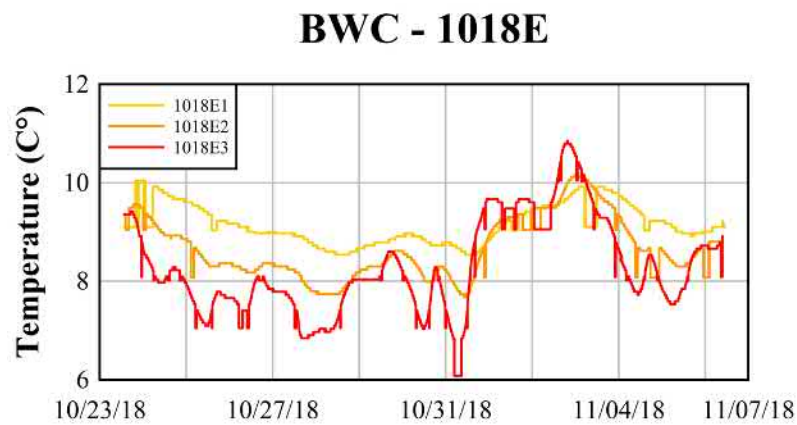


FIGURE A.10: Temperature time series at BWC during 1018 (FS-BBCB1).
Temperature probe E.

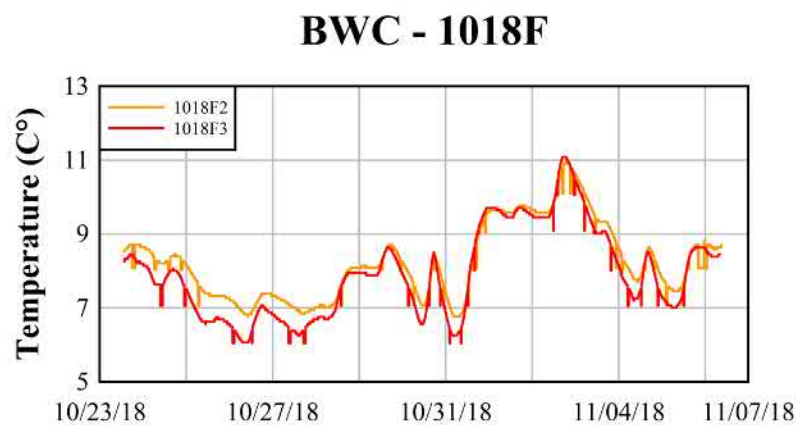


FIGURE A.11: Temperature time series at BWC during 1018 (FS-BBCB1).
Temperature probe F.

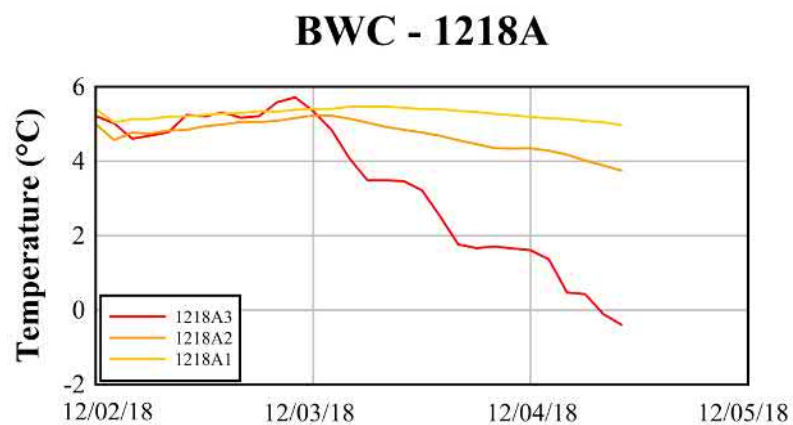


FIGURE A.12: Temperature time series at BWC during 1218 (FS-BBCB1).
Temperature probe A.

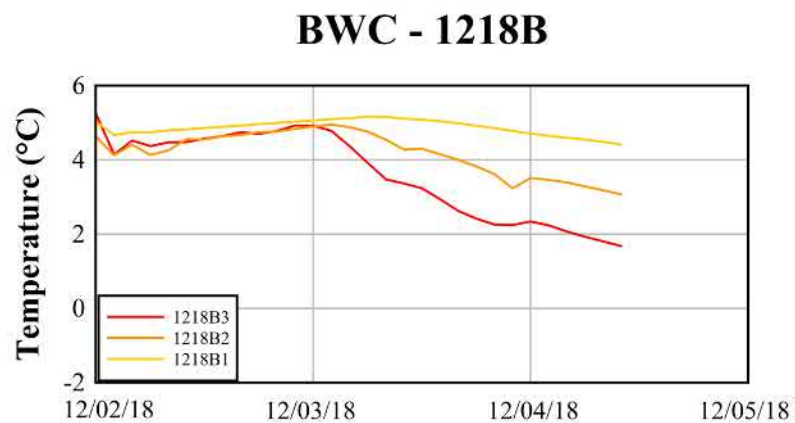


FIGURE A.13: *Temperature time series at BWC during 1218 (FS-BBCB1).
Temperature probe B.*

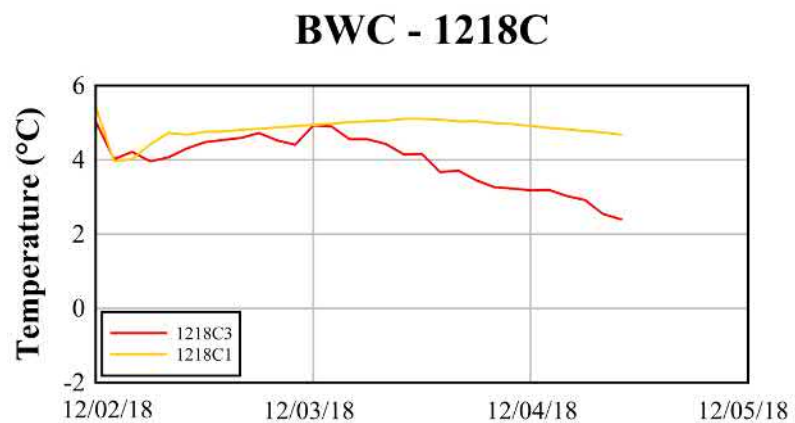


FIGURE A.14: *Temperature time series at BWC during 1218 (FS-BBCB1).
Temperature probe C.*

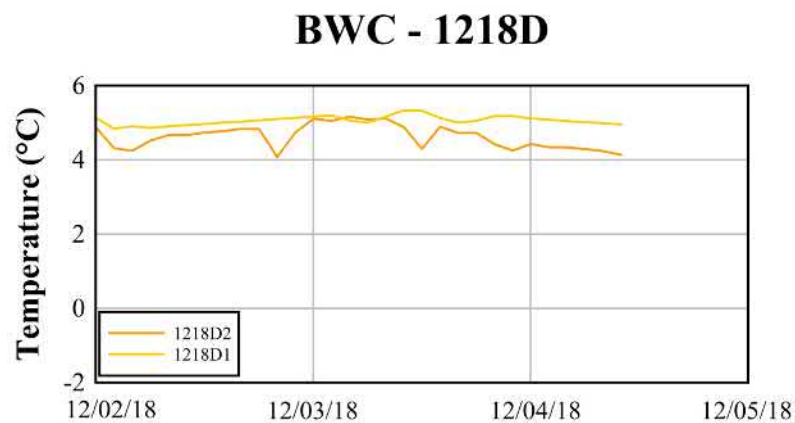


FIGURE A.15: *Temperature time series at BWC during 1218 (FS-BBCB1).
Temperature probe D.*

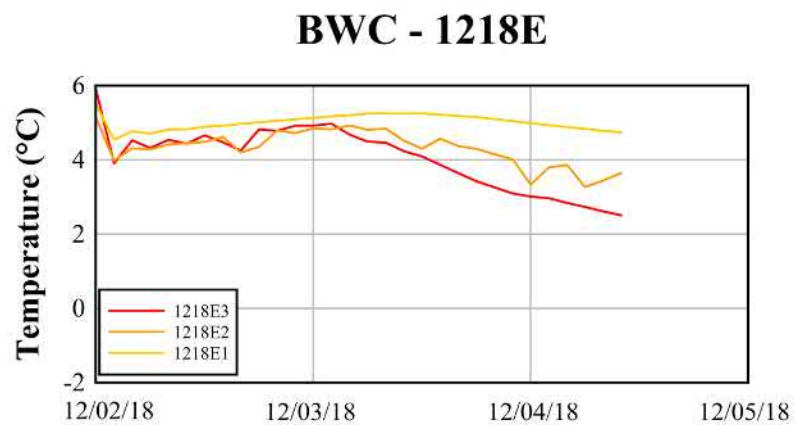


FIGURE A.16: *Temperature time series at BWC during 1218 (FS-BBCB1).
Temperature probe E.*

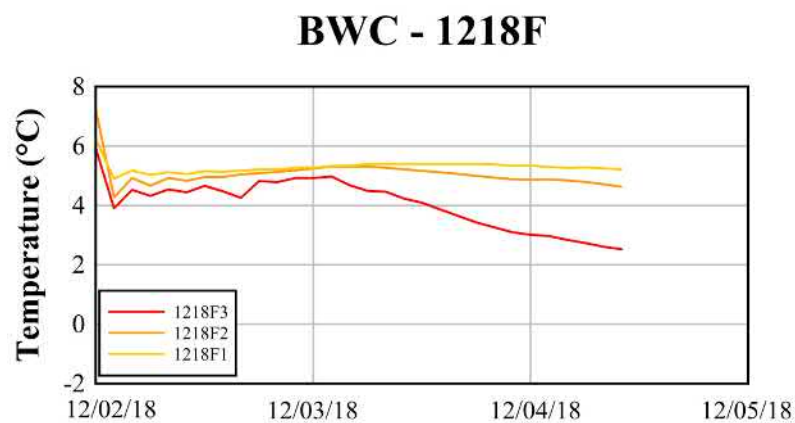


FIGURE A.17: Temperature time series at BWC during 1218 (FS-BBCB1).
Temperature probe F.

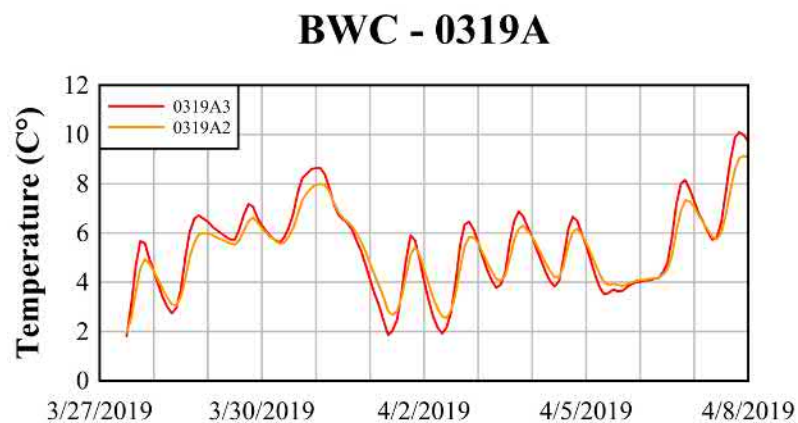


FIGURE A.18: Temperature time series at BWC during 0319 (FS-BBCB2).
Temperature probe A.

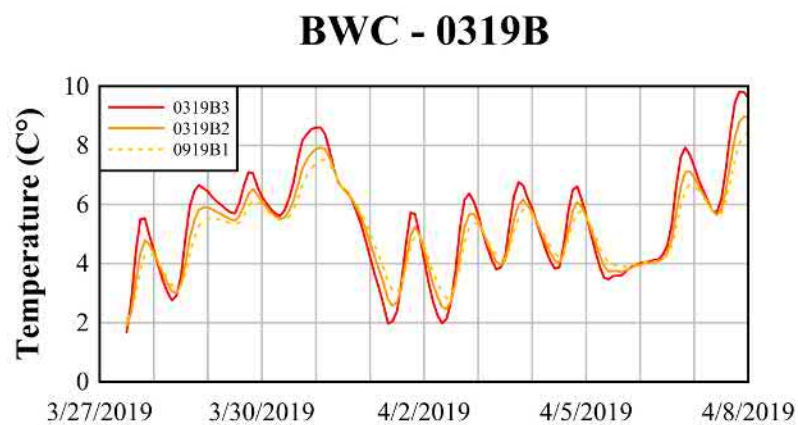


FIGURE A.19: Temperature time series at BWC during 0319 (FS-BBCB2).
Temperature probe B.

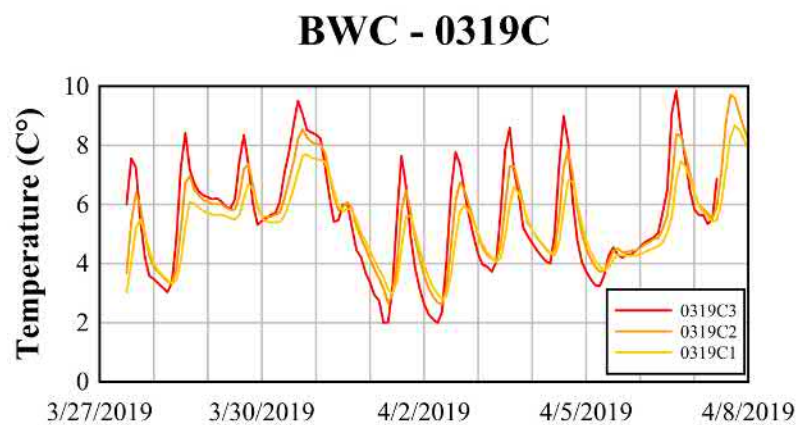


FIGURE A.20: Temperature time series at BWC during 0319 (FS-BBCB2).
Temperature probe C.

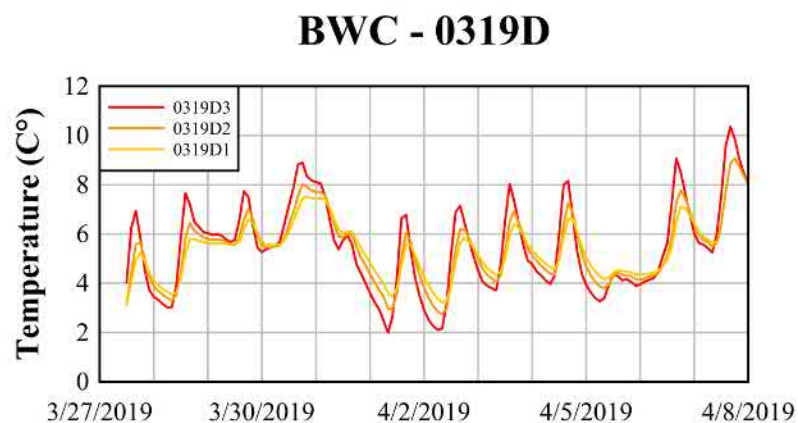


FIGURE A.21: Temperature time series at BWC during 0319 (FS-BBCB2).
Temperature probe D.

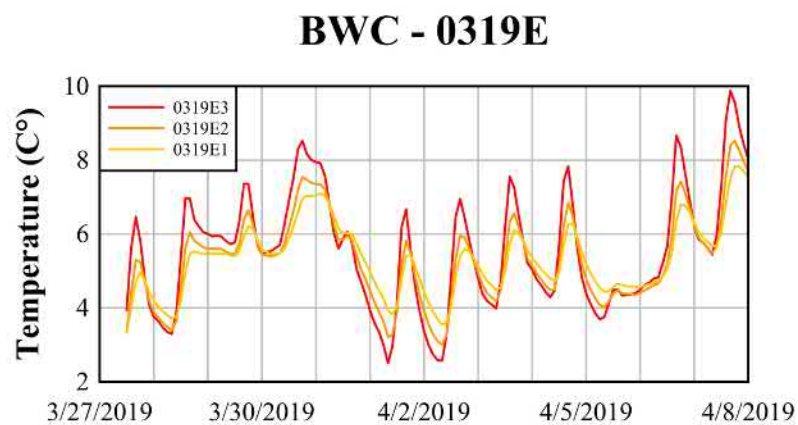


FIGURE A.22: Temperature time series at BWC during 0319 (FS-BBCB2).
Temperature probe E.

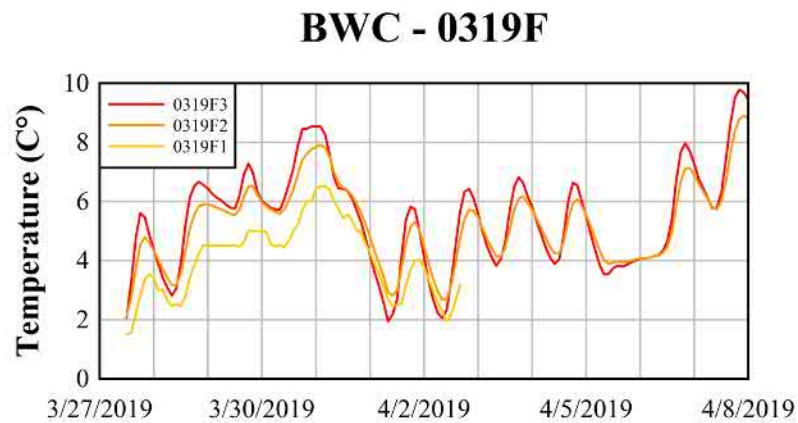


FIGURE A.23: Temperature time series at BWC during 0319 (FS-BBCB2).
Temperature probe F.

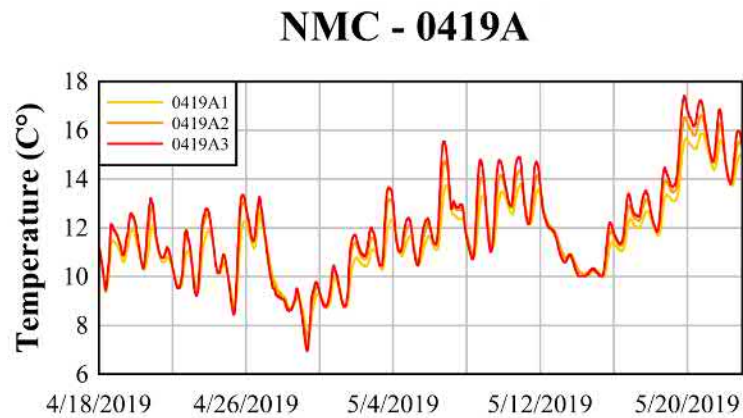


FIGURE A.24: Temperature time series at NMC during 0419 (FS-NMUC2). Temperature probe A.

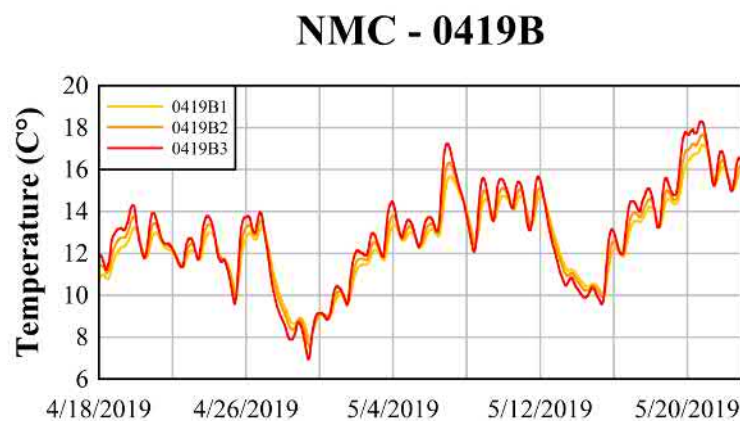


FIGURE A.25: Temperature time series at NMC during 0419 (FS-NMUC2). Temperature probe B.

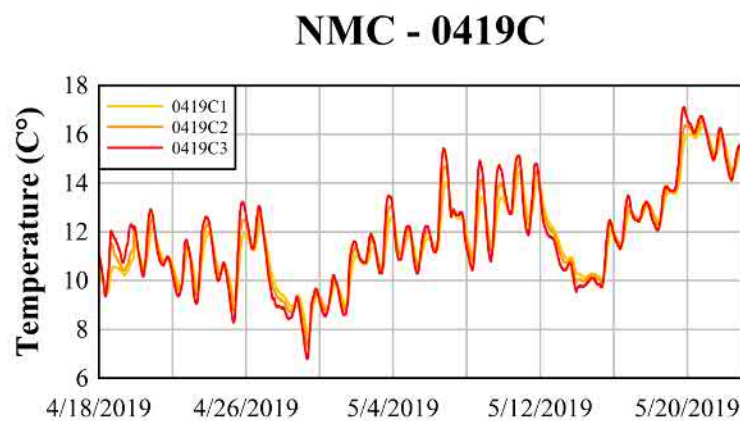


FIGURE A.26: Temperature time series at NMC during 0419 (FS-NMUC2). Temperature probe C.

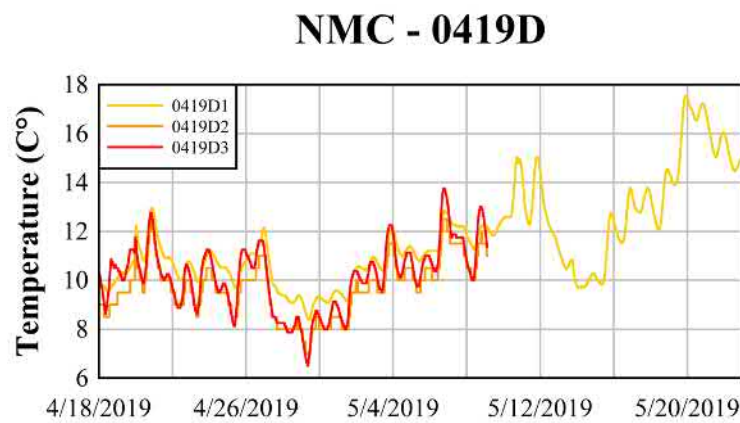


FIGURE A.27: Temperature time series at NMC during 0419 (FS-NMUC2). Temperature probe D.

Appendix B

Downward fluxes charts

In this appendix, downward flux time series of the measurements performed in the field surveys in Marcellus are illustrated for every rod. The following information is shown for each experiment:

- Downward fluxes profile of each field survey where iButtons sensors were deployed: FS-BBCB1, FS-BBCB2 and FS-NCUC2.
- Results are estimated at a mean depth of 10 *cm* from the surface-subsurface interface.

At NMC, Fluxes are estimated from a mean depth of 5 *cm* from the surface-subsurface interface. Uncompleted temperature profiles are due to fail in recording from iButton sensor.

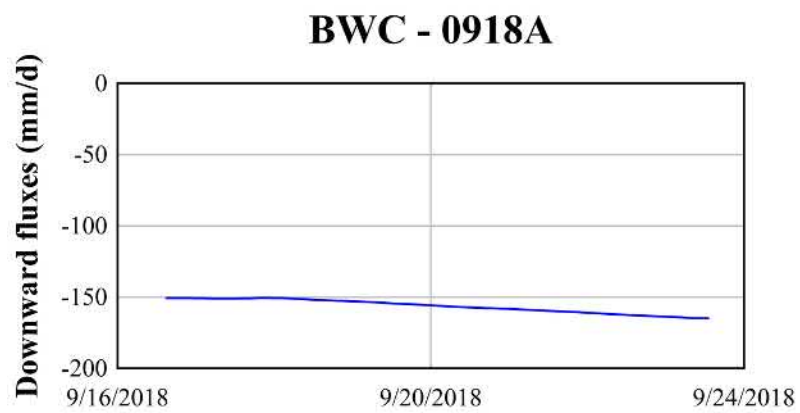


FIGURE B.1: *Downward fluxes at BWC during 0918 (FS-BBCB1). Temperature probe A.*

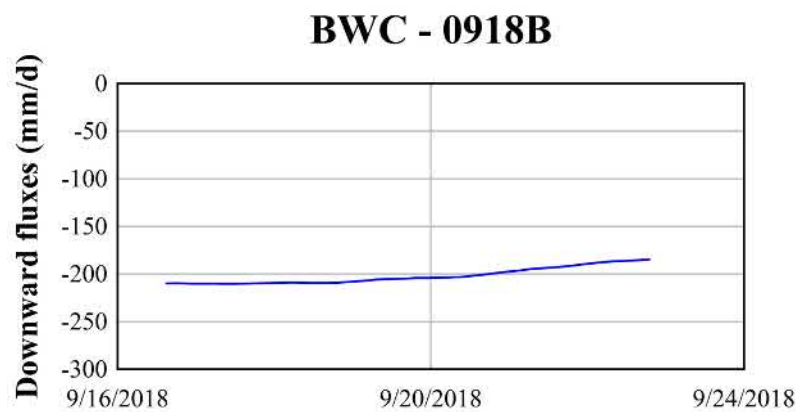


FIGURE B.2: *Downward fluxes at BWC during 0918 (FS-BBCB1). Temperature probe B.*

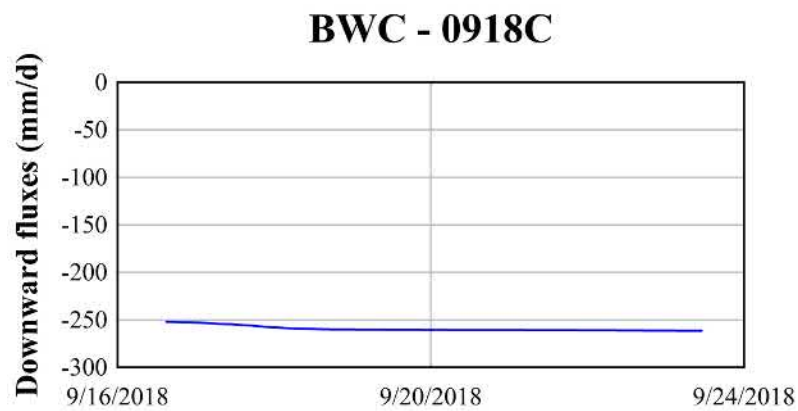


FIGURE B.3: *Downward fluxes at BWC during 0918 (FS-BBCB1). Temperature probe C.*

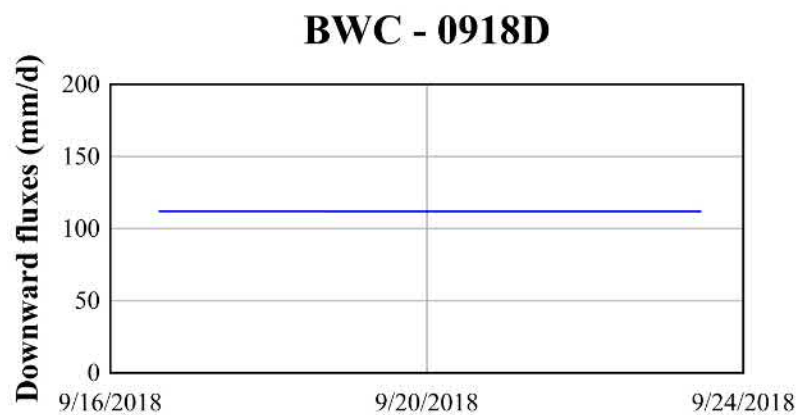


FIGURE B.4: *Downward fluxes at BWC during 0918 (FS-BBCB1). Temperature probe D.*

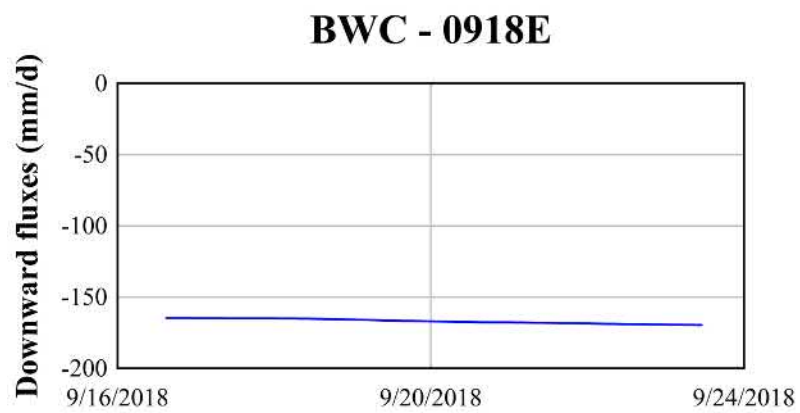


FIGURE B.5: *Downward fluxes at BWC during 0918 (FS-BBCB1). Temperature probe E.*

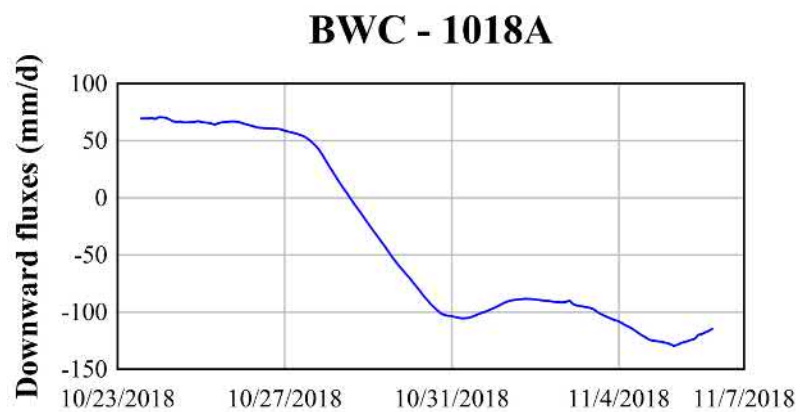


FIGURE B.6: *Downward fluxes at BWC during 1018 (FS-BBCB1). Temperature probe A.*

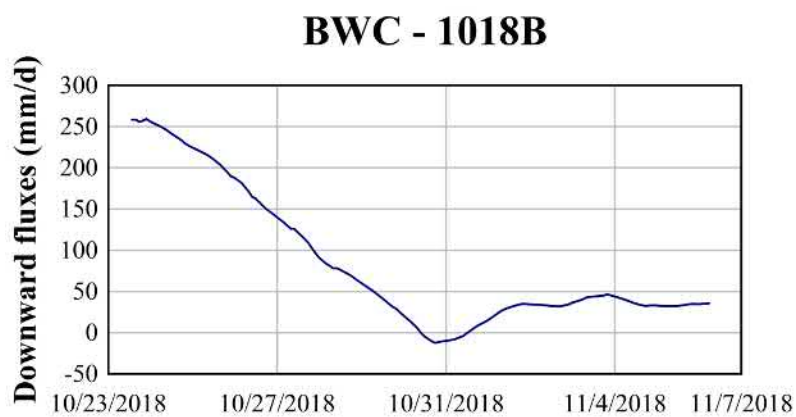


FIGURE B.7: *Downward fluxes at BWC during 1018 (FS-BBCB1). Temperature probe B.*

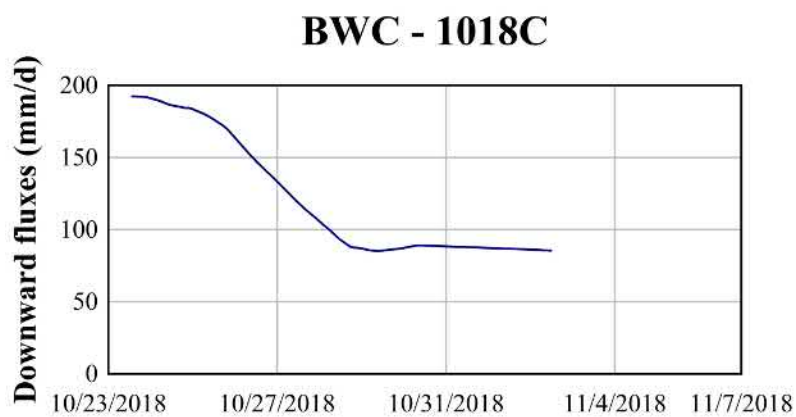


FIGURE B.8: *Downward fluxes at BWC during 1018 (FS-BBCB1). Temperature probe C.*

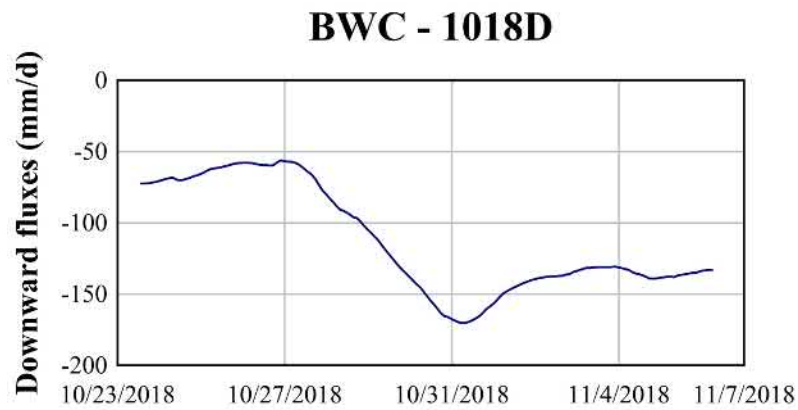


FIGURE B.9: Downward fluxes at BWC during 1018 (FS-BBCB1). Temperature probe D.

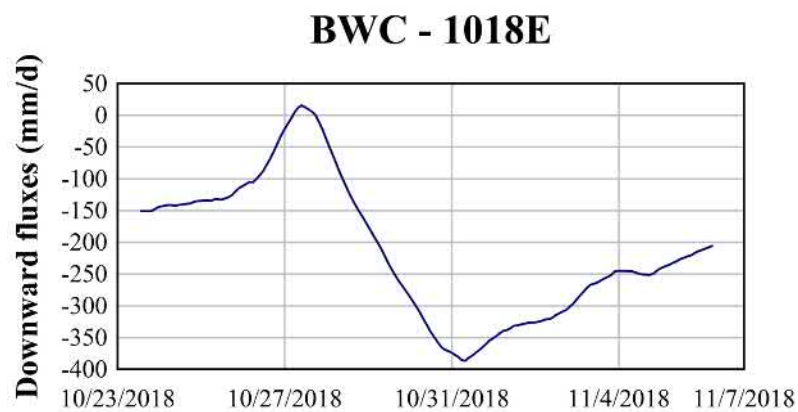


FIGURE B.10: Downward fluxes at BWC during 1018 (FS-BBCB1). Temperature probe E.

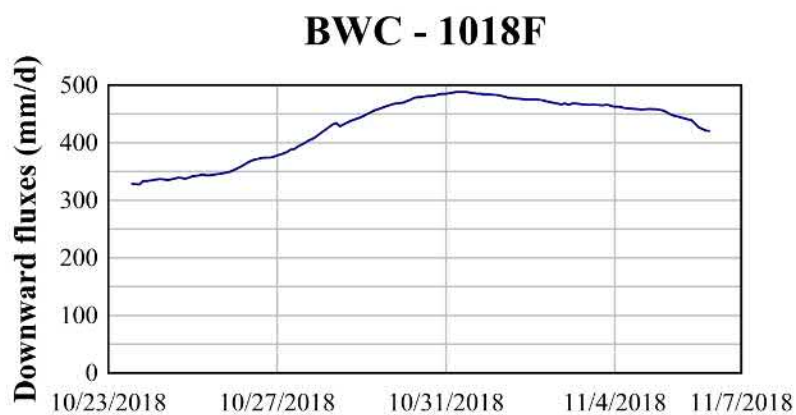


FIGURE B.11: Downward fluxes at BWC during 1018 (FS-BBCB1). Temperature probe F.

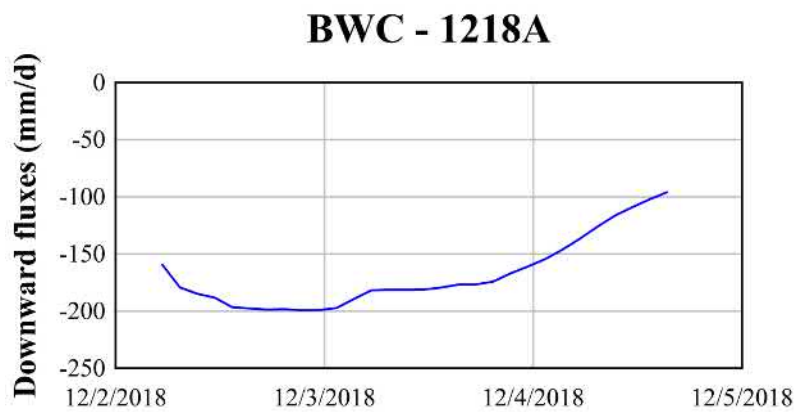


FIGURE B.12: Downward fluxes at BWC during 1218 (FS-BBCB1). Temperature probe A.



FIGURE B.13: *Downward fluxes at BWC during 1218 (FS-BBCB1). Temperature probe B.*

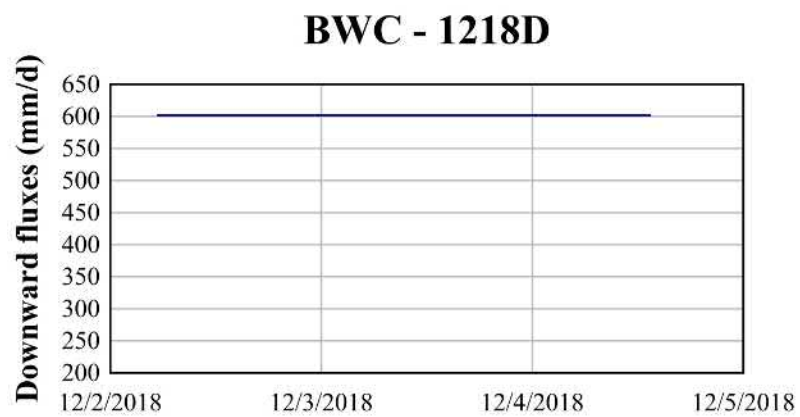


FIGURE B.14: *Downward fluxes at BWC during 1218 (FS-BBCB1). Temperature probe D.*

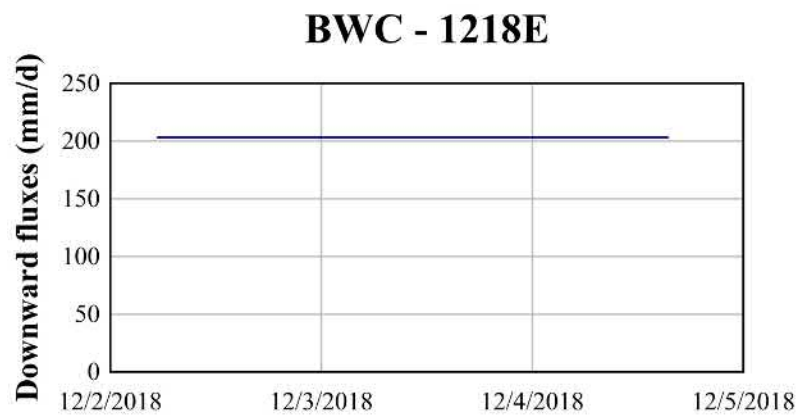


FIGURE B.15: Downward fluxes at BWC during 1218 (FS-BBCB1). Temperature probe E.

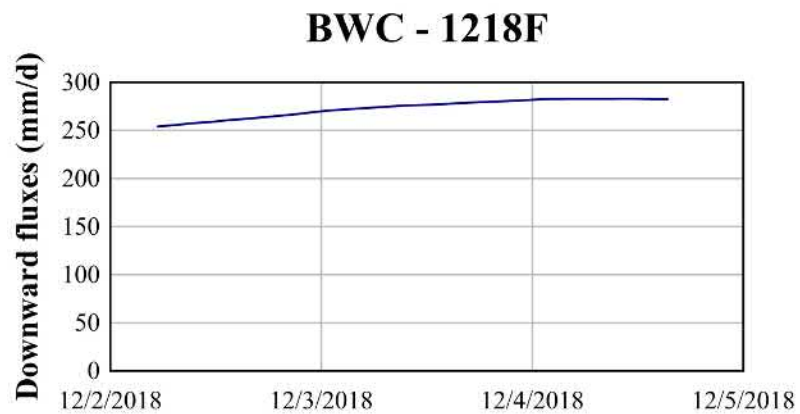


FIGURE B.16: Downward fluxes at BWC during 1218 (FS-BBCB1). Temperature probe F.

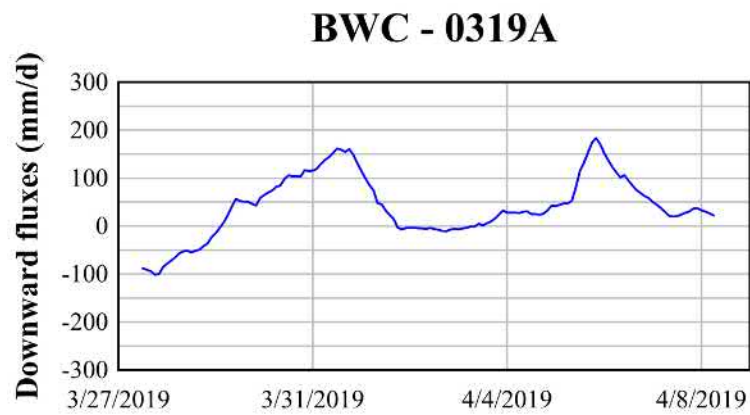


FIGURE B.17: Downward fluxes at BWC during 0319 (FS-BBCB2). Temperature probe A.

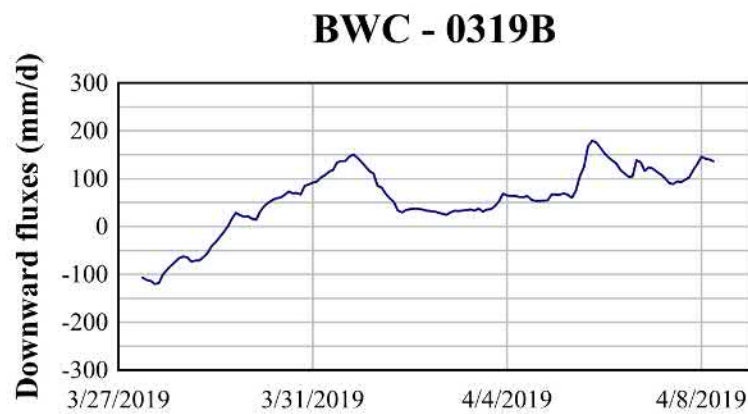


FIGURE B.18: Downward fluxes at BWC during 0319 (FS-BBCB2). Temperature probe B.

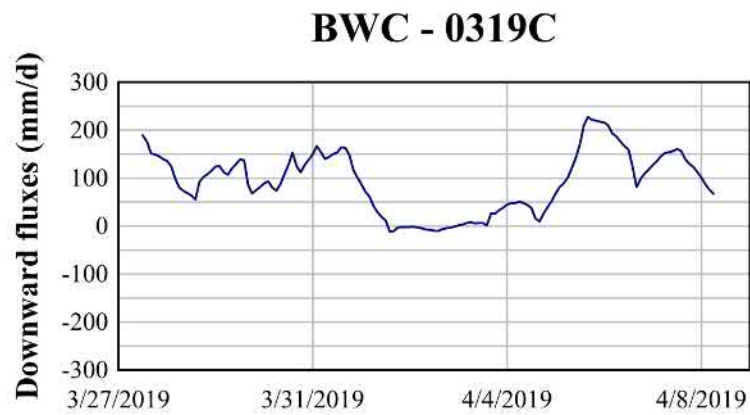


FIGURE B.19: Downward fluxes at BWC during 0319 (FS-BBCB2). Temperature probe C.

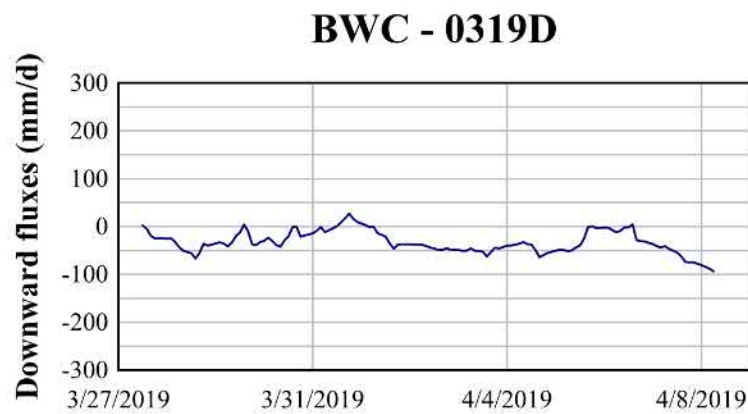


FIGURE B.20: Downward fluxes at BWC during 0319 (FS-BBCB2). Temperature probe D.

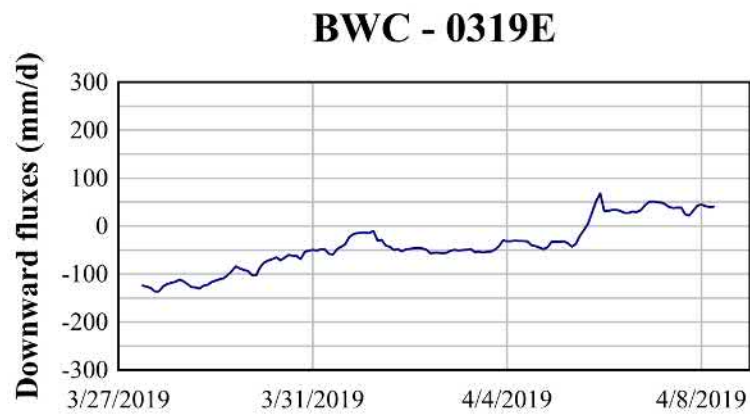


FIGURE B.21: Downward fluxes at BWC during 0319 (FS-BBCB2). Temperature probe E.

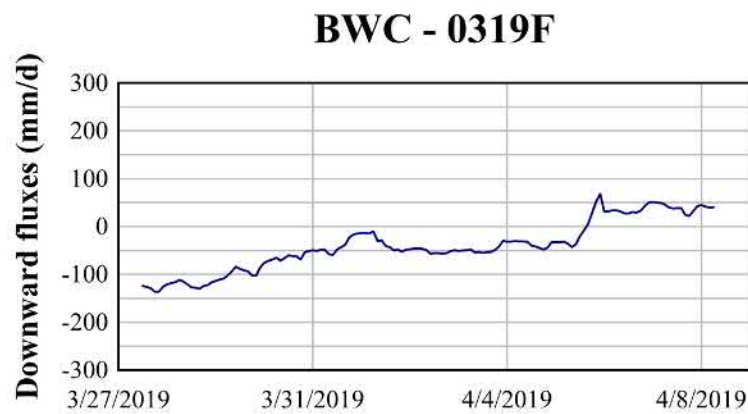


FIGURE B.22: Downward fluxes at BWC during 0319 (FS-BBCB2). Temperature probe F.

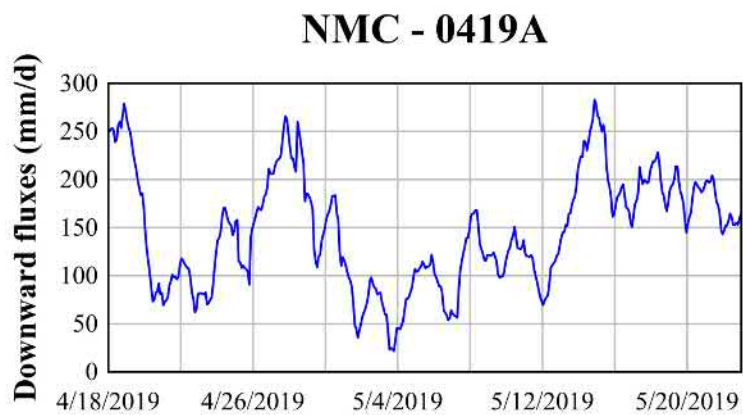


FIGURE B.23: *Downward fluxes at NMC during 0419 (FS-NMUC2).
Temperature probe A.*

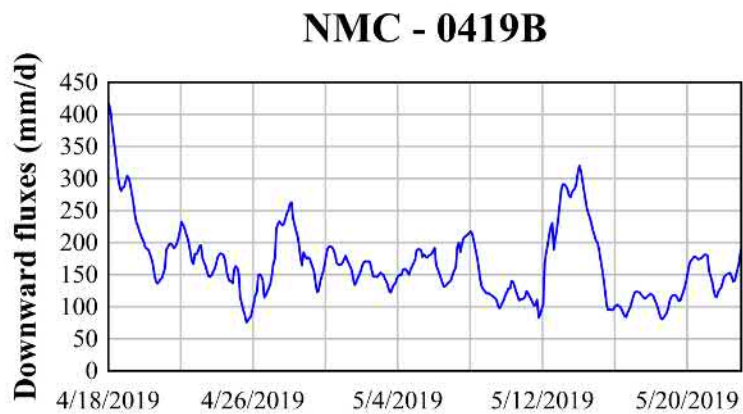


FIGURE B.24: *Downward fluxes at NMC during 0419 (FS-NMUC2).
Temperature probe B.*

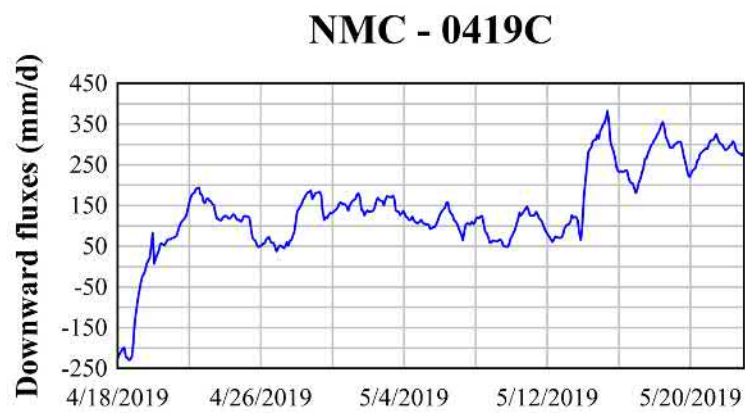


FIGURE B.25: Downward fluxes at NMC during 0419 (FS-NMUC2).
Temperature probe C.

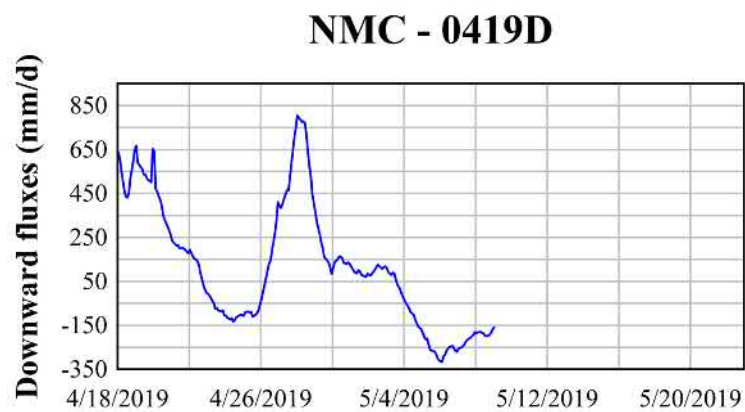


FIGURE B.26: Downward fluxes at NMC during 0419 (FS-NMUC2).
Temperature probe D.

Abbreviations and List of symbols

- A Cross-sectional area of the alluvium. 31, 32
- C_d Loss coefficient representing changes in momentum. 33
- C_{fm} Number of revolutions per minute. 71
- C_s Volumetric heat capacity of the saturated sediment grains. 36
- C_w Volumetric heat capacity of the saturated streambed. 36, 37
- C Volumetric heat capacity of the saturated sediment calculated as the mean of C_w and C_s . 36, 37
- Gr Coefficient of uniformity defined as $Gr = 1/2 \cdot (d_{84}/d_{50}) + (d_{50}/d_{16})$. xviii, xix, 89, 91
- H Total head. 33
- K_v Hydraulic conductivity. xi, xiii, xviii, xix, 60, 63, 64, 80, 84, 89, 91, 92, 94, 114–117
- M_r Momentum flux ratio. 9
- S Coefficient of uniformity defined as $S = (d_{90}/d_{10})^{1/2}$. xviii, xix, 89, 91
- T_L Temperature value at the lowest record sensor. 37, 38
- T_S Temperature value at the shallowest record sensor. 37, 38
- T Temperature. 36–38

- U_m Mean downstream velocity. 9
- V_c The depth-averaged velocity in the center of the mixing layer. 16
- V_w Volume of water. 30, 31
- V Mean velocity or velocity vector. 16, 33, 41, 71
- W Channel width. 15
- Z_L Vertical coordinate at the shallowest sensor. 37
- Z_S Vertical coordinate at the shallowest sensor. 37
- ΔL Distance between the two sensors. 37, 38
- Δh Difference in water elevation between the piezometer and the stream level. 35
- β Thermal dispersivity. xviii, 36, 37, 74
- δ Mixing layer width. 16
- κ_e Effective thermal diffusivity. 36, 37
- λ_0 Baseline thermal conductivity (in the absence of fluid flow). 36
- μ Dynamic viscosity. 38, 39
- ω_1 The fundamental signal. 74
- ω_2 The first armonic. 74
- ω_3 The second armonic. 74
- ϕ_L Phase of the surface temperature signal at the lowest sensor. 37
- ϕ_S Phase of the surface temperature signal at the shallowest sensor. 37
- ρ Water density. 9, 36, 38, 39

- σ_G Coefficient of uniformity defined as $\sigma_G = (d_{84}/d_{16})^{1/2}$. xviii, xix, 89, 91
- d_{10} The diameter where 10 percent of the distribution has a smaller particle size. xviii, xix, 89, 91
- d_{16} The diameter where 16 percent of the distribution has a smaller particle size. xviii, xix, 89, 91
- d_{50} The diameter where 50 percent of the distribution has a smaller particle size. xviii, xix, 89, 91
- d_{84} The diameter where 84 percent of the distribution has a smaller particle size. xviii, xix, 89, 91
- d_{90} The diameter where 90 percent of the distribution has a smaller particle size. xviii, xix, 89, 91
- e Hyporheic exchange per unit length. x, 31
- g The gravitational acceleration. 33
- h_1 Hydraulic head in the pipe measured at time t_1 . 64
- h_2 Hydraulic head in the pipe measured at time t_2 . 64
- h Flow depth. 15, 33
- l Characteristic length. x, 31
- t Time. 64
- v_f Linear particle velocity. 36
- z Vertical coordinate. 33, 35, 38
- AR** Auto-regressive frequency. 37

- BB** The Baltimore Brook. xii, xiii, xviii, 50, 80, 81, 84–92, 94, 97–101, 107, 108, 111, 113, 114, 116, 123
- BWC** Baltimore Brook and Cold Brook river confluence. viii, ix, xi–xiii, xviii, xix, 59, 60, 67, 73, 80–82, 84, 86–101, 107, 110–116, 124, 125
- CB** The Cold Brook. xii, xviii, 50, 80, 81, 84–91, 94, 97, 99–101, 107–109, 111, 113, 115, 116, 123
- CHZ** The Confluence Hydrodynamic Zone. xii, xviii, 1, 2, 7, 9–11, 14, 17, 44, 84–92, 94, 97, 102, 108, 115, 117
- DHR** Dynamic Armonic Regression. 73, 74, 97
- FS-BBCB1** Field study at Baltimore Brook-Cold Brook Confluence from September to December 2018. xii, xiii, 50, 59, 60, 81, 96, 98, 100, 109, 110, 115, 116
- FS-BBCB2** Field study at Baltimore Brook-Cold Brook Confluence from March to May 2019. xii, xiii, 50, 59, 60, 81, 101, 109, 110
- FS-NCUC1** Field study at Ninemile Creek-Unnamed Creek Confluence from September to December 2018. 50, 59, 60
- FS-NCUC2** Field study at Ninemile Creek-Unnamed Creek Confluence from March to May 2019. 50, 59, 60, 89, 102
- GSA** Grain size analysis. xviii, 60
- LS** Land survey. xviii, 60
- NC** The Ninemile Creek. xviii, 50, 88, 107
- NMC** Ninemile Creek and its unnamed tributary river confluence. viii, ix, xi–xiii, xviii, xix, 59, 60, 65, 67, 73, 81, 83, 85, 86, 88–92, 102–104, 107, 114, 115, 124, 125

Q Discharge. 9, 30, 31, 85, 88

TTS Temperature time series. xviii, 60

UC The Ninemile Creek's unnamed tributary. xviii, 50, 88, 115

VHF Vertical hydraulic fluxes. ix, xii, xiii, 42, 44, 98, 100, 101, 104, 109, 115–117

VHG Vertical hydraulic gradient. ix, xii, xviii, xix, 3, 35, 59, 60, 65, 66, 80, 90–93, 115, 116, 123, 124